Investigation into Maximizing Component Availability for Superconducting Cables in Turbo-electric Distributed Propulsion Aircraft

PhD Thesis

Steven Brian Nolan

Department of Electronic and Electrical Engineering
University of Strathclyde, Glasgow

October 2, 2023

Abstract

The commercial aviation industry is growing at a substantial rate, with demand doubling every 15 years and this trend is set to continue well into the 21st Century. At the same time regulatory pressures are being exerted on the industry as governments around the world seek to reduce their greenhouse gas emissions in an effort to contain global temperature rise to $2^{\circ}C$. Combined with existing infrastructure challenges, these issues are forcing air-framers to develop new, novel designs that support sustainable approaches to future aviation to meet environmental, social and economic demands. The pathway to decarbonisation of aviation will involve a combination of fuel, technology and operational measures. Many of the proposed technologies, such as electrical propulsion, are inherently disruptive and require changes to supply-chains, ground operations, maintenance standards and procedures, and pilot training. Such disruption is unavoidable given the scale of the challenge of electrical propulsion: a typical widebody jet engine for passenger aircraft can output over 22 MW fully loaded; an equivalent electrical system must be able to generate, distribute, and produce same amount of thrust with equal or greater reliability than the existing drivetrain that has been perfected over the course of the last century. Turbo-electric Distributed Propulsion (TeDP) is an approach for the electrification of propulsion systems on aircraft that aims to do this. Instead of large turbofan engines used to generate thrust, power in the engines is converted to electricity using electrical generators, and then distributed electrically through a network to propulsion motors placed in aerodynamically advantageous locations, significant fuel savings and performance benefits may be realised. Electrification of the propulsion system comes with large weight penalties. It is critical that the weight of the electrical power system does not mitigate the benefits of

electrification. Superconducting electrical machines have been proposed as a route to lightweighting the electrical power system due to their promising high power densities compared to conventional electrical machines. It is proposed that the rest of the electrical power system be superconducting as far as technically possible to minimise heat sinks within the system.

Integration of superconducting materials into the most safety critical aspects of commercial aviation raises multiple research questions regarding the design of resilient systems and how appropriate electrical protection strategies can be designed given the strict electric, magnetic, and thermal operating requirements that these components have. All electrical systems experience faults. This Thesis investigates how these faults manifest within a compact, power-electronically interfaced, superconducting network. The research presented in this thesis captures electrical protection requirements through modelling, simulation, and experimentation to develop requirements for TeDP feeder cables. By building on these requirements this thesis will then show how cable design can be optimised to withstand faults and present a control method which enables maximising throughput of cables during temperature rise events. This knowledge aims to improve availability, in terms of reducing the amount of superconducting network de-rating required, and power provision of superconducting feeder cables during adverse conditions encountered by superconducting TeDP aircraft.

Contents

List of Figures

List of Tables

Glossary

1G First Generation. **2G** Second Generation. **BLI** Boundary Layer Ingestion. **BPR** Bypass Ratio. **BSCCO** Bismuth Strontium Calcium Copper Oxide. **CB** Circuit Breaker. **CD** Cold Dielectric. **CI** Constant Impedance. **CIM** Current Iterative Method. **CP** Constant Power. **CSA** Cross Sectional Area. **dq** direct-quadrature. **FCL** Fault Current Limiting. **FCT** Fault Current Tolerant. **FDM** Finite Difference Method. **HTS** High Temperature Superconductor. **HWB** Hybrid Wing Body. **LN2** Liquid Nitrogen. **LTS** Low Temperature Superconductor. **MEA** More Electric Aircraft. **MRC** Maximum Recovery Current. **MRT** Maximum Recovery Temperature. **NZPV** Normal Zone Propagation Velocity. **PSO** Particle Swarm Optimisation. **ReBCO** Rare-earth Barium Copper Oxide. **SFCL** Superconducting Fault Current Limiter. **SMES** Superconducting Magnetic Energy Storage. **SSE** Sum of Squares Error. **TeDP** Turbo-electric Distributed Propulsion. **V4C** Voltage-based Current Compensation Converter Control. **VSC** Voltage Source Converter. **WD** Warm Dielectric. **YBCO** Yttrium Barium Copper Oxide.

List of Symbols

A Area.

C_f Filter Capacitance.

E_o Quench Constant.

G_best Best Position Swarm Has Found.

H_C Critical Magnetic Field.

I_C Critical Current.

I_o Operating Current.

I_{MRC} Maximum Recovery Current.

I_{abc} Current Contribution of Each Phase Current.

J_C Critical Current Density.

K_{sh} Capital Cost Coefficient of Shunt Material.

K_{su} Capital Cost Coefficient of Superconducting Material.

L Circuit Inductance.

P_best Best Position Particle Has Found.

Q Heat Flow.

R Circuit Resistance.

R_{crit} Critical Resistance.

R_{fault} Fault Resistance.

R_{sc} Superconductor Resistance.

R_{stab} Stabiliser Resistance.

S Active Power.

S Apparent Power.

T_C Critical Temperature.

T_{Cs} Current Sharing Temperature.

T_{MRT} Maximum Recovery Temperature.

T_o Coolant Temperature.

T_o Operating Temperature.

T_{ref} Reference Temperature.

V Particle Velocity.

W_{sh} Weight Coefficient of Shunt Material.

W_{su} Weight Coefficient of Superconducting Material.

X Particle Position.

Z Impedance.

α Damping Factor.

β Difference Between Old and New Values in Current Iterative Method.

ω_o Natural Frequency.

ρ Area.

ζ Temperature Dependence of the Transition Index..

c Heat Capacity.

$dq0$ Direct Quadrature Zero.

l Length.

n Transition Index.

Acknowledgements

I would like to thank the following people for helping me throughout this study:

Chapter 0.   Acknowledgements

Chapter 1

Introduction

1.1 Project Description

1.1.1 Challenges Facing Commercial Aviation

It is expected that by 2030, 32,600 new aircraft will be required to replace ageing existing fleets and support the anticipated growth in demand for air travel [1]. Much of this demand growth stems from a growing requirement for air transit in emerging economies for both freight and passenger travel [1]. While this growth in air transport presents an opportunity for aircraft manufacturers and operators to increase capital gains, it also places immense logistical pressures on the aviation industry at a time when regulatory oversight is becoming more pronounced due to the harmful emissions produced by flight [2].

Following the Paris Agreement at the 21st Conference of the Parties of the United Nations Framework Convention on Climate Change (UNFCCC), it was agreed that governments around the world would aim to keep the increase of global temperatures significantly below 2° C to prevent the worst effects of climate change, with a long-term goal of limiting the increase to 1.5^o C [2]. It is proposed that this will be achieved by reducing emissions of green house gas (GHG) emissions. The aviation industry represents one of the fastest growing sources of GHG [2]. As of 2018 the amount of CO_2 produced by international aviation reached 895 million tonnes and at current passenger growth rates could, by 2050, consume 25 % of the worlds carbon budget for
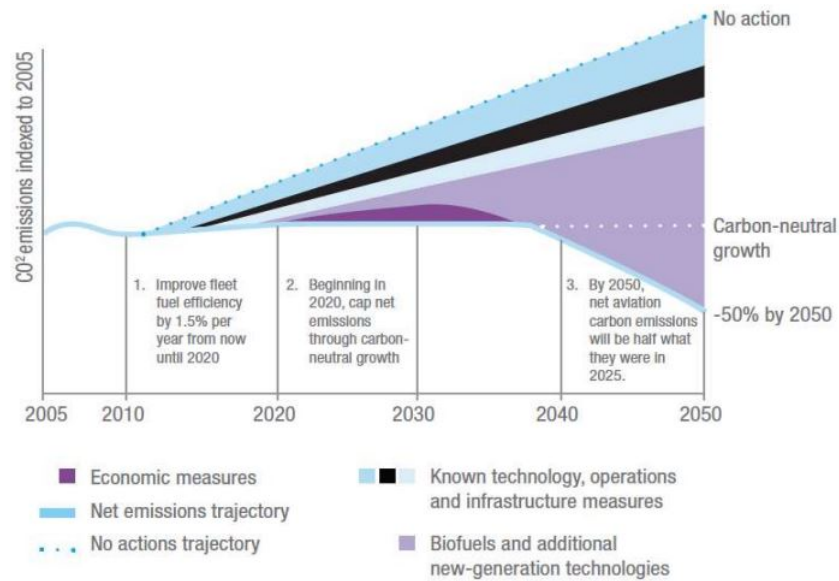
Figure 1.1: ATAG Community Vision for Reducing Aircraft Emissions [4]

maintaining global temperatures less than 1.5^o C above pre-industrial levels [3].

To tackle the challenge of reducing GHG emissions from the aviation industry, a number of government bodies have, in recent years, begun to implement policies that seek to reduce the emissions of commercial aviation. For instance, since 2012 the European Union (EU) airlines have been included in the EU emissions trading system (EU ETS). This requires that airlines to monitor and report their emissions while also capping total emissions using a tradeable allowance system [5]. This only affects flights that operate wholly within the EU [5]. To address emissions globally the International Civil Aviation Organization (ICAO) introduced the Carbon Offsetting and Reduction Scheme for International Aviation (CORSIA) in 2021. This aims to promote carbon neutral growth that will keep emissions at 2019 levels while passenger growth continues [6]. CORSIA aims to force airlines to offset any increases in civil aviation emissions through carbon reduction activities or carbon trading schemes such as the EU ETS [6]. One criticism of these approaches is that airlines can buy emissions allowances and transfer the cost to the consumer, rather than focus on reducing emissions through using clean fuels [7].However, as GHG allowance caps are reduced over time, greater investment in new solutions will become an imperative. Figure 1.1, from the Air Trans-

Chapter 1. Introduction

Technology Benefits	Near Term (2015-2025)	Mid Term (2025-2035)	Far Term (Beyond 2035)
Noise	22-35 dB	32-42 dB	42-52 dB
LTO NO_x Emissions	70-75 %	80 %	>80 %
Cruise NO_x Emissions	65-70 %	80 %	>80 %
Aircraft Fuel/Energy Consumption	40-50 %	50-60 %	60-80 %

Table 1.1: NASA Targets for Future Aircraft

port Action Group (ATAG), illustrates the view of the aviation community of the steps required for carbon neutral growth to be achieved. These include improvements in fuel types, operations and technology.

To address the challenges facing the aviation industry, government bodies such as NASA [4] have set performance and emissions targets that future aircraft will need to meet if the aviation industry is to meet growing demand while fulfilling its environmental obligations. Table 1.1 shows the NASA targets for future aircraft. Meeting these ambitious targets will require significant and radical technological advances across a range of disciplines [8].

As shown in the first row of Table 1.1, GHG are not the only emissions aircraft produce that need to be addressed: acoustic noise plays a considerable role in the determination of when and where planes are allowed to fly [9]. Aircraft noise, which can reach 140 dB, can have a significant impact on human health and can significantly affect cardiovascular health, sleep quality and increase psychological effects such as stress and anxiety [9]. Noise is primarily dependent on the the volume of flights, aircraft types and flight path and due to these adverse effects aircraft capacity within a given airspace can be limited or restricted certain times of the day. This can result in reduced throughput at important international hubs such as London Heathrow International Airport (LHR) which has limited night time flying [10]. To accommodate the increased demand in air transit, air craft must be made quieter or new hub airports will be needed to ensure noise restrictions are not exceeded in existing busy air spaces. Even if noise reductions are able to lighten the restrictions around flying at certain airports and increase airspace capacity, expanding existing airports through additional runways, terminals and supporting transport links to final destination can be extremely challenging, costly, and damaging to the local environment [11]. To cope with future

4

demand other alternatives may be needed such as greater use of regional airports.

Currently many regional airports are operating at reduced capacity. This can be due to a number of reasons such as distance from final destination, lack of connecting flights, and weaker ground transport links, but can also be due to lacking long enough runways for which commercial aircraft can safely land on and take-off from [12]. One example of this in London City Airport (LCY), which had a runway field length of only 1080 m until it was extended to 1500 m in 1992 [13]. The short runway restricts the types of aircraft that can land, despite the airports proximity to the cities major financial districts. To ensure that future demand can be met using existing infrastructure, runway field-length performance needs to be improved, in other words, future aircraft must improve short-take-off-and-landing (STOL) capability, if they are to allow for greater use of currently under-capacity regional airports [12]. Electrical propulsion can help achieve this by enabling concept designs that can improve aerodynamic design through optimal placement of propulsion fans and greater effective bypass ratio.

1.1.2 Aircraft Electrification

The rapid development of hydraulic power and bleed air systems following the end of World War 2 led to the majority of commercial aircraft secondary functions, such as actuation and de-icing, being supported by these methods [8]. The use of electricity on-board aircraft was limited to cabin lighting and utility for critical electronic equipment, owing to the greater simplicity and maturity of the other competing systems [8]. However, multiple oil crisis in the 1970s, led aircraft designers to seek alternative solutions to increase aircraft fuel burn efficiency which consequently revived interest in the use of electrical power for auxiliary systems [8]. The application of electrical power to loads traditionally powered through hydraulics, pneumatic, and mechanical systems, is now commonly refereed to as the More Electric Aircraft (MEA) concept. Figure 1.2 shows a modern conventional aircraft engine power flow while Figure 1.3 shows that of a MEA.

MEA is an evolutionary step in aircraft design that seeks to power non-propulsive based subsystems using electricity, a concept which has been enabled by continued
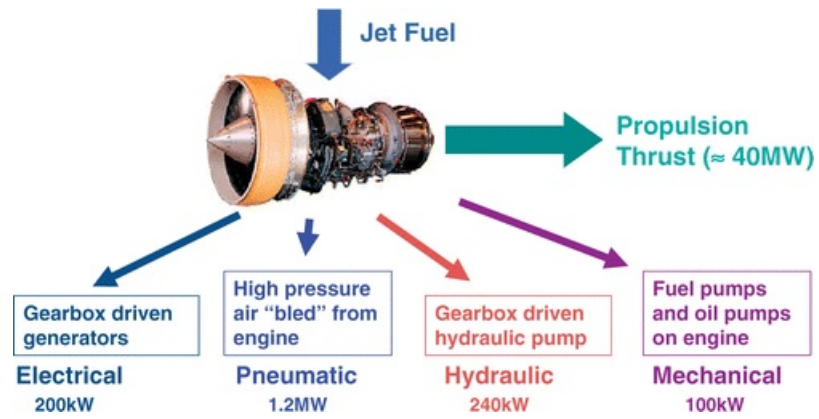
Figure 1.2: Conventional Engine Power Flow [14]
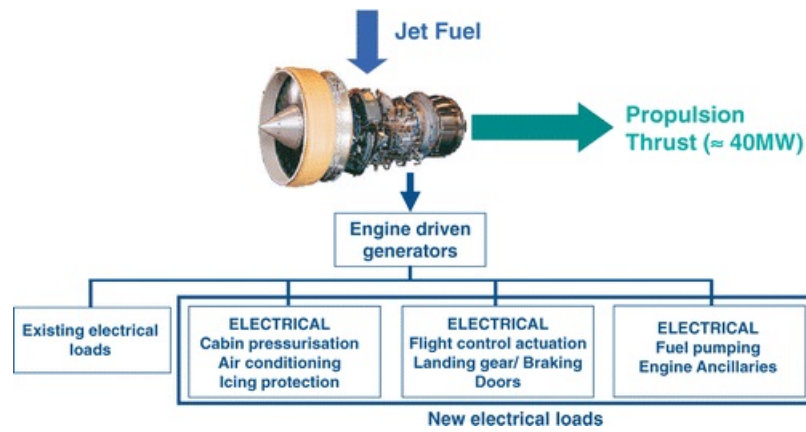
Figure 1.3: MEA Power Flow [14]

improvements in electrical components power density and efficiency [15]. Over the preceding decades, demands for electrical power on-board aircraft have grown significantly and continue to do so. Much of the early growth in this area is the result of an increased demand for in flight entertainment services and flight control systems such as the fly-by-wire system introduced in the Airbus A320 family [16]. More recently however, this growth has been due to the reallocation of functionality to use electrical power, for example the Boeing 787 Dreamliner which presented a major step-change in on-board electrical generation [17].

The Boeing 787 Dreamliner is the first commercial aircraft to have an onboard electrical generation capacity greater than 1 MW [17]. A major change in this aircraft is the introduction of a bleedless system. Bleed air, a resource that is traditionally responsible for wing anti-icing and cabin environmental control, was removed for the 787 model, instead being replaced by a system of electro-thermal plates and compressor pumps powered by the generators [18]. This reduces the amount of power needed to be extracted from the engine by as much as 35 % compared to a bleed air system [18]. Mechanical complexity is reduced by replacing hydraulic systems (e.g. engine start and braking) with electrical systems. Relative to a B767, mechanical complexity has been reduced by more than 50 % due to these changes which can have the knock-on effect of reducing maintenance costs [19]. As well as a more extensive electrical system the aircraft also more than 50 % of the aircraft structure is made from carbon fibre reinforced composites, reducing its weight and therefore fuel burn requirements [20]. Figure 1.4 compares the fuel efficiency of different aircraft to the industry average. The impact of these technological improvements is to significantly improve fuel efficiency compared to other, large passenger aircraft, as shown in Figure 1.4.

While MEA, alongside other technological innovations in air-frame materials can have a significant impact on fuel-economy of commercial aviation, in order to reach the targets outlined by NASA, even more radical changes will be needed [22]. These will need to target the aircraft propulsion system which is, by orders of magnitude, the largest source of power consumption on board aircraft. To meaningfully decrease the energy required per payload there exists four main avenues: reduce aircraft empty

Figure 1.4: Difference From Industry Average Fuel Efficiency for 14 Aircraft Types, 2016 [21]

weight, reduce aerodynamic drag, increase the bypass-ratio of the turbofan engines, drive-train efficiency improvements.

1.1.3 Turbo-electric Distributed Propulsion

Turbo-electric distributed propulsion (TeDP) is proposed as a concept to meet future emissions targets for aircraft. In a TeDP aircraft the large gas turbine engines are replaced with turbine generators which will then transmit power electrically to propulsion motors [22]. This type of architecture opens up a wide range of design freedom in the number, and placement, of propulsion motors, allowing for designers to place motors in aerodynamically advantageous positions to take advantage of effects such as boundary layer ingestion (BLI) while increasing the effective bypass-ratio (BPR) of the propulsion system [22]. Figure 1.5 shows the NASA N3-X aircraft concept which combines hybrid wing body (HWB) with TeDP in an attempt to achieve the goals outlined in Table 1.1.

The use of distributed electrical propulsion can have a number of positive effects

Figure 1.5: NASA N3-X Aircraft Concept [23]

on the overall aircraft system [22] [23] [24]. One of these benefits is the enabling of a very high effective BPR through the use of multiple small fans while ensuring that the efficiency of large turbine generators is maintained through the electrical isolation of generation and propulsion [25]. This electrical decoupling enables the distribution system to act as a variable speed gearbox, allowing the fans and generators to operate at different speeds. This provides further gains in efficiency as shaft speed can be optimised without needing to consider maximum fan tip speed [26]. This can also allow for yaw control [27] through varying of motor speed as well as greater amounts of redundancy and control due to the large number of fans.

A significant challenge for TeDP is ensuring that the weight of the electrical power system does not mitigate the benefits of electrification [28]. The high electrical power requirements for the aircraft, expected to be up to 25 MW at take-off, results in challenging power densities for the electrical equipment to address this challenge. As discussed in Chapter 2, different architectures and rated system parameters (e.g. voltage) can be used to reduce system weight. Superconducting electrical machines have been proposed as a route to meeting high power densities required for these electrical power systems. To minimise electrical losses and weight of the cabling it is proposed that as much of the electrical power system as possible is superconducting including the generators, distribution cables, and propulsion motors [29].

The safety critical nature of the aircraft application, necessitates that the super-

conducting electrical power system has an appropriate electrical protection system. To implement this, the unique electrical characteristics and thermal requirements of superconducting components needs to be understood within the context of a power electronics interfaced electrical power system, such as those proposed for TeDP aircraft, under fault conditions. Critical to the design of the protection system is determining the impact faults have on protection system requirements and how faults can be managed by system design choices. To do this the fault behaviour of the system must be characterised.

While there are a number of existing studies analysing the impact of faults within AC superconducting networks and cables, the impact of faults within compact DC superconducting networks requires work to determine how much of the existing theory for conventional DC networks is applicable. Of particular interest is the impact of capacitive discharge during rectifier interfaced short circuit faults. Additionally, An often cited advantage of the DC TeDP concept is the improved controllability offered by the many power electronics interfaces. However, the way in which this additional controllability can be harnessed during adverse superconducting feeder operating conditions has not been demonstrated in the literature. By focusing on the DC transmission due to the greater controllability, and then narrowing our scope to the superconducting cables within, this work will contribute to these areas by addressing the following questions:

1. What is the likely fault response of a compact superconducting DC network and how will the network and superconducting cable parameters affect this?

2. What Thermal operating margins are required to protect superconducting cables from high currents experienced during fault ride-through and can this be optimised?

3. What control schemes can implemented to improve power availability after a fault that leads to temperature rise within a superconducting feeder cable during ride-through?

1.2 Summary of Contributions

To address the questions numbered in the previous section this work offers the following contributions:

1. **Major:** An optimisation framework for sizing superconducting and conventional current carrying layers with respect to system ride-through requirements.

2. **Major:** Development and analysis of a control scheme that allows greater power flow through superconducting cables following temperature rise event such as a fault ride-through.

3. **Minor:** Analysis of the requirements for a critically damped response in an RLC circuit containing a superconducting tape using modelling and simulation.

4. **Minor:** Experimental results involving the discharge of a capacitor through superconducting tapes to gain a better understanding of short circuits in power electronically interfaced, DC superconducting circuits.

5. **Minor:** Development of fault-ride through limits of superconducting cables based on cable parameters and system cooling capability.

1.2.1 Supporting Publications

The following publications have been made based on the contributions of the research presented in this thesis

Journal Publications

1. **Nolan, S.**, Jones, C. E., Norman, P. J. and Burt, G. M., "Sizing of superconducting cables for turbo-electric distributed propulsion aircraft using a particle swarm optimisation approach", 4 May 2022, In: IEEE Transactions on Transportation Electrification. 8, 4, p. 4789-4798 10 p.

2. **Nolan, S.**, Jones, C. E., Pena Alzola, R., Norman, P. J., Burt, G., Miller, P. and Husband, M., "Voltage based current compensation converter control for power

electronic interfaced distribution networks in future aircraft", Dec 2020, In: IEEE Transactions on Transportation Electrification. 6, 4, p. 1819-1829 11 p.

Conference Publications

1. **Nolan, S.**, Jones, C. E., Munro, R., Norman, P., Galloway, S., Venuturumilli, S., Sheng, J. and Yuan, W., "Experimental investigation into the fault response of superconducting hybrid electric propulsion electrical power system to a DC rail to rail fault", 30 Dec 2017, In: IOP Conference Series: Materials Science and Engineering. 279, 1, 8 p., 012014. First Presented at Joint Cryogenic Engineering Conference and International Cryogenic Materials Conference, Madison, WI. USA.

2. **Nolan, S.**, Jones, C. E., Norman, P., Galloway, S. and Burt, G., "Protection requirements capture for superconducting cables in TeDP aircraft using a thermal-electrical cable model", 19 Sep 2017. 15 p. First Presented at SAE 2017 AeroTech Congress and Exhibition, Fort Worth, USA.

3. **Nolan, S.**, Jones, C. E., Norman, P. J. and Galloway, S. J.,"Understanding the impact of failure modes of cables for the design of turbo-electric distributed propulsion electrical power systems.", 5 Oct 2016, 6 p. First Presented at Electrical Systems for Aircraft, Railway, Ship propulsion and Road Vehicles and International Transportation Electrification Conference, Toulouse, France.

1.3 Thesis Outline

The work contained in each section of this Thesis is outlined here.

Chapter 2 contains a literature review which first discusses superconductors: their history, their applications, the current stage of development and some of the key theories upon which the research presented in this thesis relies. It also introduces superconducting electrical systems applied to TeDP, discussing the main concepts, technologies and targets required for its realization. Finally, this chapter will discusses superconducting cables and their failure modes. In addition to this background knowledge, short topic

12

specific literature reviews are presented in chapters 3 through 6 to build upon this material.

Chapter 3 focuses on the fault behaviour of superconductors in a converter interfaced DC network. The basic principles of the fault circuit are discussed before a superconducting tape model is described and implemented in MATLABs Simulink. The influence of circuit and tape parameters on the fault circuit response is then discussed. The experimental capture of capacitor discharging through a superconducting tape, mimicking the initial moments of a rectifier interfaced faced, is described and discussed.

Chapter 4 presents a finite difference method based modelling approach to evaluate hot spots on superconducting cables and discusses this failure mode with respect to two cable design concepts: fault current limiting, and fault current tolerant. The concept of maximum recovery temperature and maximum recovery current are introduced here. These provide operating limits for cables, which are demonstrated in Chapters 5 and 6.

Chapter 5 presents a framework for the sizing of superconducting TeDP cables with respect to fault ride through protection constraints using an optimisation based approach. As such, this chapter presents a method for minimising the lifetime cost of the cable design with respect to initial capital and on going costs due to weight (fuel).

Chapter 6 develops a power electronic control scheme which maximises the amount of power that can be transmitted through superconducting cables that have undergone temperature rise. The chapter describes the operation of the scheme, and demonstrates its capability in a test network in a MATLAB Simulink based system simulation.

Chapter 7 concludes this work by summarising the key points of each chapter and highlighting future work opportunities.

Chapter 2

Background

2.1 Superconductivity

2.1.1 History of Superconductivity

Superconductivity is the phenomenon of zero electrical resistance that occurs in certain materials below a critical temperature, T_c. It was first discovered in 1911 by Heike Kamerlingh Onnes [30]. Following this discovery, which occurred in mercury below a temperature of 4.2K, it was quickly discovered that superconductivity was present in other materials at a variety of temperatures. Figure 2.1 shows the time-line for the discovery of superconducting materials and their corresponding T_c.

It was also found that superconducting materials also exhibited another important property: the expulsion of magnetic fields from the interior of materials operating in the superconducting state [31]. This is now known as the Meissner effect and is illustrated in Figure 2.2. The first significant step to understanding the Meissner effect came in 1935 with the London equations. These equations presented a phenomenological model that could describe the exponential expelling of magnetic fields from the superconducting material as a function of penetration length into the material [32]. Up to this point all superconductors discovered so far fell into the category of Type-I superconductors, those that completely expel all magnetic fields below the critical field. However, it was around this time a new type of superconductor, named Type-II superconductors, were discovered.
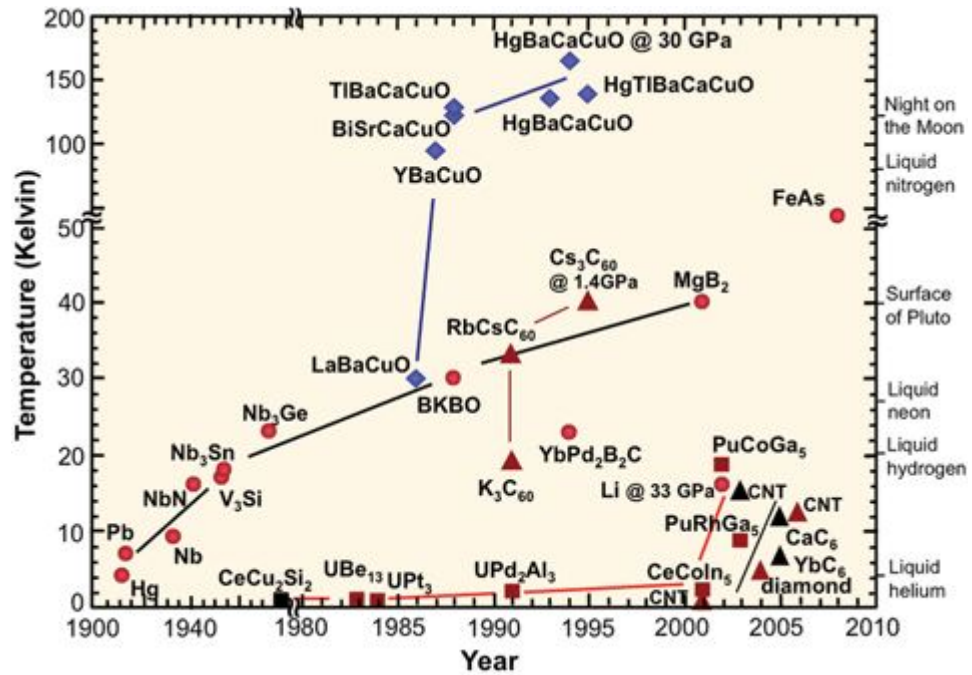
Figure 2.1: Time-line of Superconductivity Discovery in Different Materials and Their Critical Temperature [30]
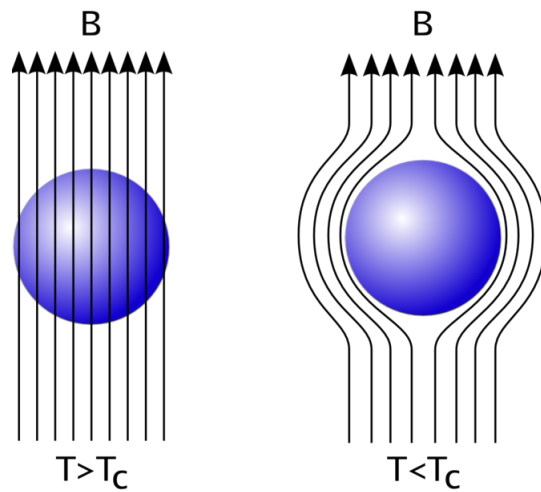
Figure 2.2: Illustration of the Meissner effect on a sample of superconducting material [33]

Chapter 2. Background

Type-II superconductors allow for a mixed state to exist above a lower critical field (while still producing no resistance to electrical current), before complete penetration at a second, higher, critical field value [31]. In 1950 the Ginzburg-Landau theory emerged and classified the two types of superconductors, Type-I and Type-II, based on the energy interface between the superconducting and normal states [34]. A major breakthrough in the understanding of superconductivity came in 1957 with the Bardeen Cooper Schrieffer theory (BCS theory). This theory describes superconductivity as being caused by a net attractive force between electrons that allows the formation of Cooper Pairs, creating a condensate that requires much more energy to disrupt than the oscillating atoms within the material can produce at temperatures below 30 K [35].

As well as developing fundamental understanding of the superconductivity phenomenon, applications of early superconductors began to take off the second half of the twentieth century. However, due to the low critical temperatures requiring the use of expensive cryogenic coolants, and the cost of manufacturing superconducting components, application of these early superconducting materials were limited to specialized equipment such as magnetic resonance imaging (MRI), mass spectrometers, and particle accelerators for fundamental physical research. These two applications continue to dominate the demand for superconducting materials to the present day [36].

The large rise in the maximum critical temperature during the 1980s, seen on Figure 2.1, is due to the discovery of cuprate based materials that could produce superconductivity at temperatures greater than 30 K. These are commonly referred to as High Temperature Superconductors (HTS). The existence of materials capable of operating at temperatures above 30 K was first discovered in 1986 by IBM researchers Georg Bednorz and Karl Alexander Muller who found that a sample of lanthanum-based cuprate had a transition temperature of 35 K [37]. Superconductivity at these temperatures cannot be explained by BCS Theory and a full description of their fundamental properties is still in development.

Following this initial discovery, a number of other cuprate based superconductors were found such as Yttrium Barium Copper Oxide YBCO and Bismuth Strontium Calcium Copper Oxide BSCCO materials which exhibited critical temperatures of 93 K
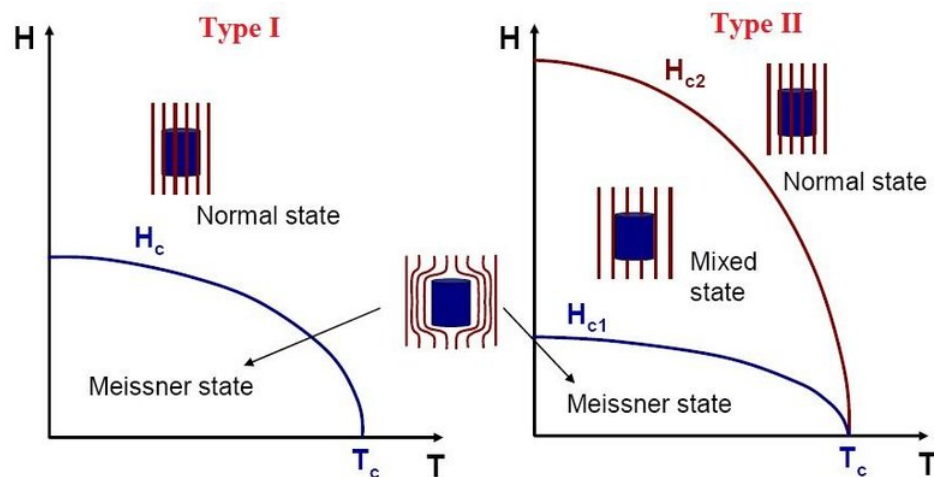
Figure 2.3: Influence of a Magnetic Field on the State of a Type-I (left) and Type-II (Right) Superconductor [39]

and 108 K respectively. These discoveries marked an important milestone as the critical temperature exceeded the boiling point for liquid nitrogen (LN_2), a cheap and easy to produce cryogenic agent [38]. This increased the economic feasibility of superconductors penetrating other industries such as power transmission and commercial transportation.

2.1.2 Critical Properties of High-Temperature Superconductors

Critical Magnetic Field

All HTS materials are Type-II superconductors that contain two critical magnetic fields. A lower critical field, H_{c1}, below which the material exhibits both zero DC-resistivity and the Meissner effect; a high critical field, H_{c2}, that when passed the material ceases to be superconducting. In between these two values is known as the mixed state in which the material allows magnetic flux to penetrate it although, it is still considered to be superconducting. An illustration of the superconducting states in relation to applied field and temperature is shown on Figure 2.3.

Within the mixed state the magnetic field penetrates the material at discrete points known as fluxons [40]. In the presence of an electrical current, fluxons would move due to the Lorentz force exerted on them were it not for flux pinning [40]. Flux pinning uses the manufacturing of defects in the material to prevent the movement of flux by

creating energy barriers that can not be overcome by the force produced by the flow of current [40]. In the absence of pinning, the movement of flux would create an electric field due to Faraday's law, leading to electrical resistance.

Critical Current

The requirement of maintaining a critical magnetic field value below the H_{C2} (A/m) threshold leads directly to the formation of a critical current, I_C (A), a maximum current that the material can transmit before the properties of superconductivity are lost. This is due to the destruction of superconductivity as the magnetic field produced by the flow of electrons, the self-field, exceeds H_{C2} [41]. This can be shown using the relationship for the magnetic field produced by a conductor:

$$I_c = 2\pi r H_c \tag{2.1}$$

Where r (m) is the radius of the conductor. In practice, I_c is normally defined as the point at which the measurable voltage across the superconductor reaches 1 μ V/cm.

Critical Temperature

While most materials have a negative resistance-temperature coefficient, causing resistance to reduce in line with the temperature, superconductors are set apart by the complete loss of DC electrical resistance below T_C (K). This illustrated on Figure 2.4 which compares the resistance temperature relationship of a conventional conductor and a superconductor.

While superconductivity is present in HTS materials below T_C, the critical field, and current, has been found to be strongly temperature dependent, approaching zero as temperature reaches T_C. Thus manufacturers will often quote critical current with respect to a specified operating temperatures. One example is 77 K, the boiling point of LN_2, which is often used when describing tape and cable critical currents.
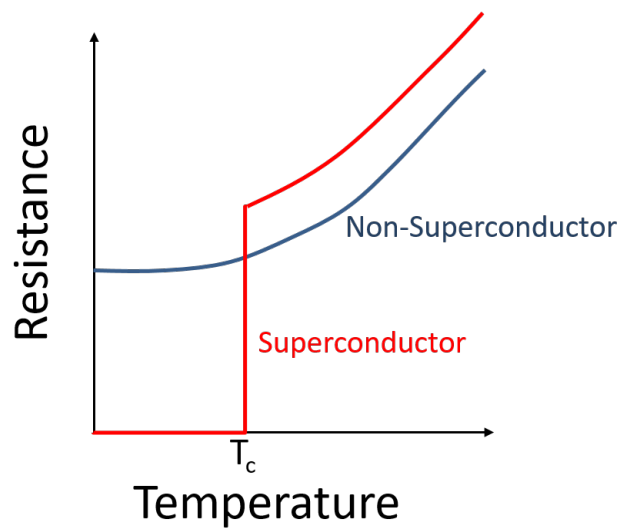
Figure 2.4: Relationship between Resistance and Temperature in a Superconductor

Critical Surface of Superconductivity

The interdependence of the three critical values, I_C, T_C, and H_C leads to the development of the critical surface of superconductivity as illustrated on Figure 2.5. If the HTS material exceeds this surface, it undergoes quench, the term used for the state-transition from superconducting operating mode to resistive operating mode. In their resistive state, HTS materials are generally very poor conductors, providing high amounts of resistance to the flow of current and thus dissipate large amounts of energy as heat due to Ohmic losses. Uncontrolled, this can lead to damaging of the HTS material [41].

Critical current improvements have led to the development of extremely high current density HTS materials at a range of different operating magnetic field strengths and temperatures [43]. Figure 2.6 shows the variation in whole wire critical current density with applied magnetic field for a variety of HTS materials operating at 4.2 K. Each material has its own strengths and weaknesses, thus it is unlikely that any single material will emerge as dominant for all applications and temperature ranges. However, BSCCO and YBCO are considered the most mature HTS materials in the literature, having been the subject of intense research since the 1980s [41]. Of these

19
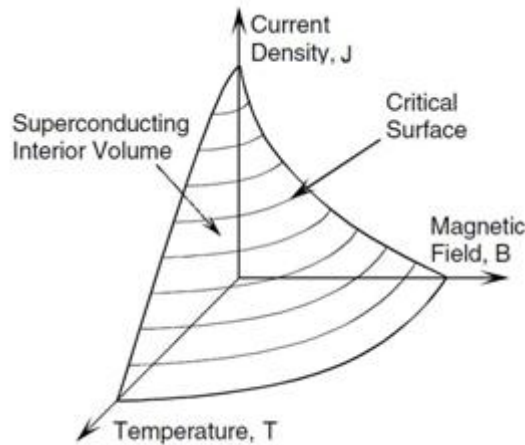
Figure 2.5: Illustration of the Critical Surface of Superconductivity [42]

two YBCO is likely to be the preferable material for Superconducting TeDP cables due to the advantages discussed in Section 2.3. Magnesium diboride is another promising HTS material, however as this work focuses on superconducting cables operating at at LN_2 Temperatures, it is not discussed here due to its low critical temperature of 39 K.

2.1.3 Applications of High Temperature Superconductors in High Power Applications

This section will give a brief overview of the main applications that HTS materials have within high power systems to highlight the benefits these materials may unlock within a future TeDP system.

Superconducting Fault Current Limiters

There are a variety of potential applications for HTS materials in power system components, one of which is the superconducting fault current limiter (SFCL). Faults in an electrical system can cause a large current to flow within the network which can be harmful to all components in the fault path. By reducing fault current magnitude through the use of SFCLs, the amount of overcurrent experienced by these components can be reduced. This can limit damage, but also enables the use of smaller circuit-breakers (CBs) which can be less expensive and light weight [44]. SFCLs can also
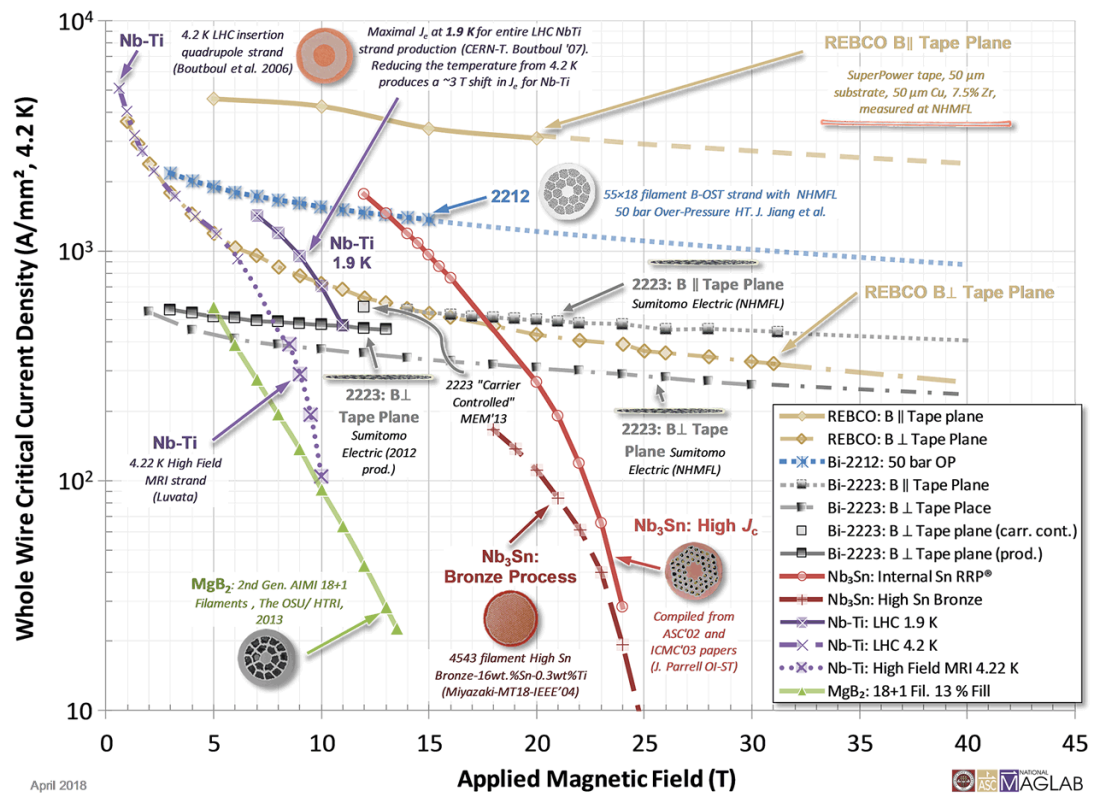
Figure 2.6: Critical Current for Different Superconducting Material Types w.r.t. Applied Magnetic Fields [43]

Figure 2.7: Example of RSFCL [47]

reduce the need to upgrade and replace protection equipment required to accommodate higher fault levels as electrical power demand increases in a network [44].

SFCLs are an area of intense research and as such have a much higher TRL than most other superconducting power system components. Many demonstrator projects have been field tested within transmission and typically adopt one of a few design types, including inductive, resistive, and a hybrid between the two [45]. Resistive SFCLs (R-SFCLs) have a number of advantages for aerospace applications, primarily lower weight and volume than inductive type SFCL types and the simplicity of its design and operation [46]. A concept design of an R-SFCL is shown on Figure 2.7.

R-SFCLs work by taking advantage of the large step change in resistance between the superconducting and non-superconducting phases of the material. During normal, non-faulted operation, they have zero resistance to the flow of current. Once a low impedance fault occurs, the current rises above the critical current level causing the device to undergo quench. This causes a large step change in circuit resistance and rapidly reduces the current flowing in the faulted section, providing passive protection

of the network [44].

   While R-SFCL devices present the opportunity to reduce current during a fault, a disadvantage is the time it takes to reset them due to the large temperature rise they undergo through absorbing fault energy. This requires time (several seconds to several minutes) and energy for the cooling system to remove the excess heat and allow temperature to fall below the critical current before normal current can flow [48]. This recovery time could be unacceptable in a TeDP application where loss of power can lead to loss of propulsion, although it is likely there will be significant redundancy given the safety critical application of commercial aviation.

Distribution Cables

Superconducting cables are proposed for the TeDP electrical power systems to avoid heat sources within the transmission network and to allow the entire network to be embedded within a single cryogenic cooling system [29]. An additional benefit of superconducting cables is the potential for distribution at much lower voltages compared to conventional cables for comparable power levels. Superconducting cables form a core aspect of this research and are discussed further in Section 2.3.

HTS Machines

HTS machines are another application for superconducting materials in situations where high power density is a requirement such as TeDP. Within the TeDP network HTS machines will provide for both power generation and conversion into propulsion. HTS field coils are capable of carrying large amounts of current with low loss. This allows them to support very high magnetic fields as well as enabling an air-core machine design which removes the heavy iron core normally required to reduce the magnetic reluctance of the machine design [49]. These factors significantly increases the power density compared to conventional machines. Partially superconducting machines have been presented wherein the superconducting materials are used within the field coils to produce high magnetic fields while maintaining a conventional armature circuit [50]. This so-called partially-superconducting machine has the potential for significant power
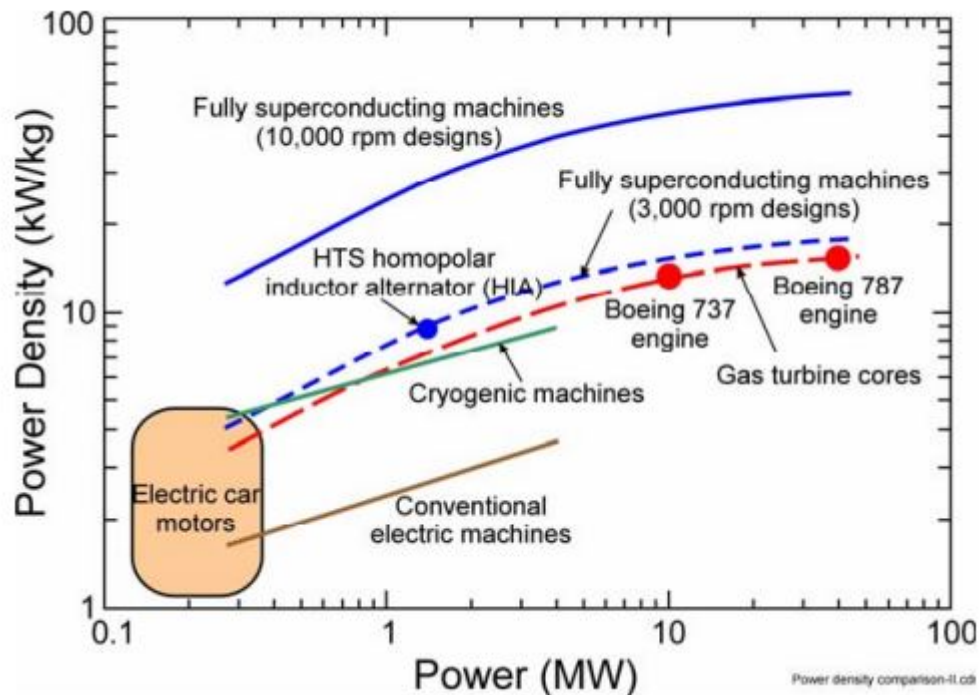
Figure 2.8: Power Density Comparison for a Variety of Propulsion Technologies at Different Power Levels [53]

density gains but is not enough to enable a TeDP aircraft at commercial size as the large air gaps in the design reduce the flux density of the magnetic field and thus limit their potential [51].

To achieve the construction a fully superconducting machine, the primary problem that needs to be addressed is the AC losses produced in the superconducting armature as a consequence of the high rpm speeds needed to achieve power density goals [52]. These losses increase the amount of power that needs to be consumed by the cryogenic cooling system and significantly impact overall weight. Despite this there is potential for fully superconducting machines with power density's of up to 40 kW/kg [49]. Figure 2.8 shows a graph that compares the power density capability of different Machine technologies with increasing power level. It can be seen from this figure that the potential gains in power density for high RPM (10,000 rpm) superconducting machine designs are considerable and have the potential to be more power dense than contemporary jet engines.

Figure 2.9: Nasa N3-X Concept Aircraft illustration [54]

2.2 Superconducting Turbo-electric Distributed Propulsion

2.2.1 Overview of System Concepts

NASA N3-X Concept

The NASA N3-X aircraft concept, shown in Figure 2.9, utilises a range of current state of the art and future, technologies to meet the targets outlined by Figure 1.2 [29]. The baseline concept for the aircraft places the power generation on the wing-tips and distributes power electrically to the propulsion motors placed along the body of the aircraft [29]. This allows for a high effective by-pass ratio by using sixteen propulsion motors rather than the typically found two or four engine configurations of a contemporary aircraft. This also increases the level of propulsion motor redundancy. As well, it allows boundary layer ingestion which increases thrust by reducing the average inlet velocity of the air entering the fan as well as reducing drag [55]. These features increase the aerodynamic efficiency, reducing fuel burn and subsequent emissions. Additionally, this location of the propulsion motors along to top of the fuselage allows the airframe

Figure 2.10: EADS E-Thrust Concept Art [57]

to provide noise shielding [56]. The hybrid wing body (HWB) design also improves the lift to drag ratio of the aircraft as lift is generated across the entire aircraft.

EADS E-Thrust Concept

Another concept aircraft that adopts a similar electrical architecture is that of the EADS E-thrust which is shown on Figure 2.10 [57]. First proposed in 2013, this concept maintains many of the same features as the NASA N3-X such as superconductivity, HWB airframe, distributed electric propulsion. One major difference between the designs are the placement of the HTS generators, which are moved from the wing-tips to a central location, reducing the need for long cable runs and allowing for further noise reduction. Central placement of the gas turbine generators is also being explored for the N3-X+ [56].

The EADS E-Thrust Concept uses a series-hybrid electrical architecture [58]. Whereas a purely turbo-electric architecture is one in which the gas turbines drive electrical generators, the series-hybrid architecture has a battery which stores energy and can also contribute to propulsion [58]. This configuration can reduce overall emissions compared to traditional aircraft, however the weight of the energy storage can be a significant drawback compared to turbo-electric architectures [58].
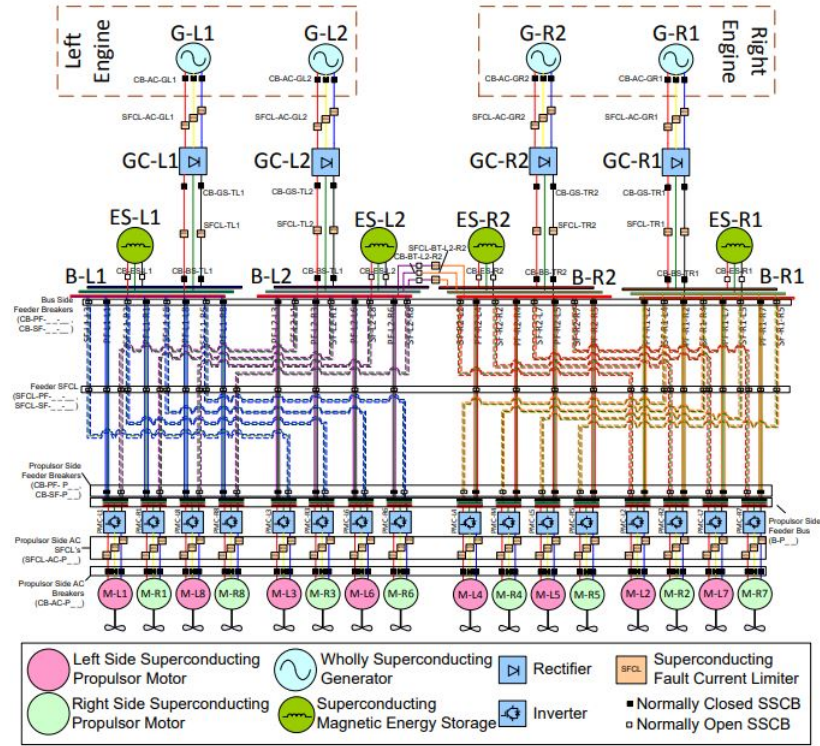
Figure 2.11: DC system Architecture Example [29]

2.2.2 Electrical Network Architectures for TeDP

DC and AC Distribution Concepts

A key design decision for TeDP is whether the network architecture adopted should be predominantly AC or DC. A majority DC design has been proposed through a joint study conducted by NASA and Rolls Royce [29], however a study conducted by DEAP [59] highlighted significant trade-offs between the two distribution modes. An example DC architecture developed as part of a NASA consortium trade-study is shown on Figure 2.11.

One of the primary motivations for a DC distribution architecture is the electrical decoupling of electrical generators from the propulsion motors [60]. This is achieved through the power electronics modules in the distribution network enabling the generators and motors to operate at different shaft speeds without the need for a mechanical gearbox. In a contemporary turbofan engine, shaft speed is limited by maximum tip

27

speed, by using a DC distribution this is no longer the case, allowing the generator and fan to operate at their optimal speed at all points in the flight [61]. In this way the distribution network works as a variable gearbox controlled through power electronics. This also allows for greater control options, as fans can be controlled individually using the power electronic interfaces.

The use of multiple power electronics interfaces in the DC architecture creates a number of technical challenges for its design and implementation. These challenges are, first the weight of the power electronic converters [28], and secondly the impact they have on electrical protection and fault response [62]. With TeDP expected to operate at around 25 MW, even if power electronics undergo rapid increases in power density, they will account for a significant fraction of overall system mass, as will be shown in the next subsection. Additionally, even if lofty efficiency targets are met($> 99\%$), a 1% power loss within a multi-MW converter translates to tens of kW that need to be removed by a cooling system. If these power converters are operated at cryogenic temperatures, as is proposed in [63] to improve efficiency, the cooling system will have to remove these losses with an associated penalty due to Carnot efficiency, further driving up mass.

Given the safety critical nature of aircraft application, being able to manage and protect the system when electrical faults take place is of paramount importance. Power electronics influence the short-circuit current fault shape and size due to the filtering elements they require [62] and, in some cases, the control schemes they utilise. An example of when a control algorithm influencing a fault can occur is in the case of a power electronics module controlling an energy storage device. In this case the module can discharge into a fault in attempt to regulate bus voltage [64]. This is a condition known as protection blinding [64].

Although DC distribution has been the focus of more research, AC distribution concepts exist such as the one shown in Figure 2.12. AC-based distribution architectures offer weight savings when compared to DC-based architectures, as they do not require power electronic converters, for AC to DC power conversion [59]. Superconducting cables do exhibit losses in AC due to superconducting hysteresis and eddy current
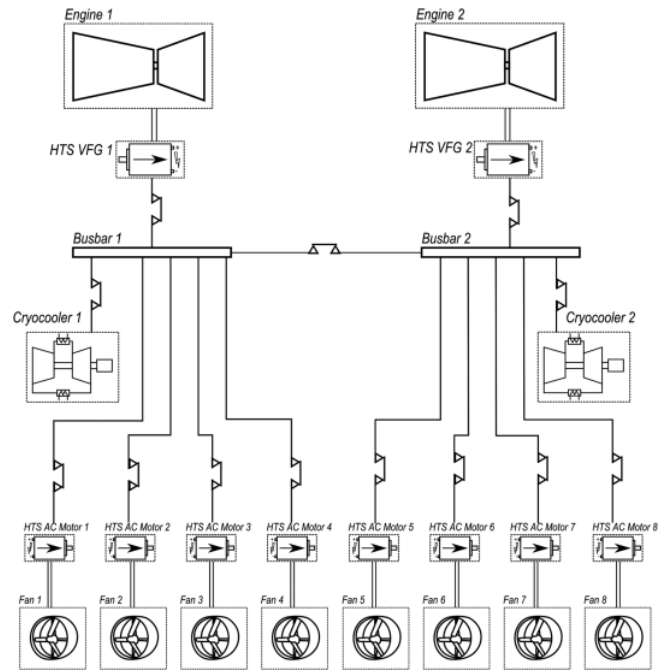
Figure 2.12: AC Superconducting TeDP Network Architecture Example [59]

losses, this loss has to be weighed up against the losses from power electronic converters in the equivalent DC architecture. All losses are dissipated as heat, which increases the power requirement, and physical size, of the associated cryogenic cooler [28]. Jones et al. compared 3 architectures, a DC distribution network, an AC distribution network, and a hybrid AC-DC system that contained a back to back rectifier-inverter at the motor [28]. The study found that not only was the AC system lighter, but also far more efficient from a power loss perspective due to the inefficiencies of the power electronics modules [28].

The increased mass of a DC network is further exasperated by the weight of the protection system due to the low power density of DC circuit breakers [29]. Despite this, a DC distribution system remains the focus of much research due to the greater controllability it offers.

Voltage Level

As of 2019 the Boeing 787 Dreamliner presents the highest use of electrical power on board aircraft at 1 MW rated capacity. However, this substantial amount of power is

transmitted at either $230VAC$, $100VAC$, or $\pm270VDC$ [65]. As such, on state-of-the-art aircraft, the voltage levels remain within the limits of Paschen's law [66]. Paschen's law describes the minimum voltage required to breakdown an air-gap between two conductors as a function of air pressure and reaches a minimum at $327VDC$ [66]. By operating systems below this voltage magnitude, the risk of arcing is limited.

In contrast terrestrial electrical distribution networks universally use higher voltages as power requirements increase to reduce voltage drop between network nodes, and the conductor cross-sectional area (CSA) requirements associated with resistive materials. TeDP represents an order of magnitude increase in the consumption of electrical power on board and aircraft. Using conventional conductors for on-board electrical power systems on large, TeDP aircraft such as the N3-X would require significant increases in the cross-sectional area of components assuming the limits of Paschen's law are kept.

Unlike a conventional conducting system, the weight of a DC superconducting TeDP network is largely independent of the current transmitted due to the negligible losses of superconducting components and the large critical current densities offered [90]. For comparison, the current density of copper conductor in coil is typically around $3A/mm^2$ while Nexans Superconductor offer YBCO tapes at densities of $100A/mm^2$ [67]. However, the YBCO tapes need to be cooled to $77K$ to maintain this current density. Hence, the total weight of superconducting components are more significantly impacted by cooling requirements than conventional components [28].

While the weight of the superconducting materials does not vary significantly with current and voltage, the protection equipment, namely the DC circuit breakers, and the power electronic converters are dependent on these parameters. The results of the sensitivity analysis conducted in [29] found a voltage level greater than $5kV$ to be optimal for a wide range of DC architectures when considering both component weight and losses in the overall propulsion system [29]. This varied depending on the system architecture adopted but ultimately found component weight was largely insensitive to voltage across a wide steady-state operating range from $5kV$ to $20kV$. This is indicated in Figure 2.13.
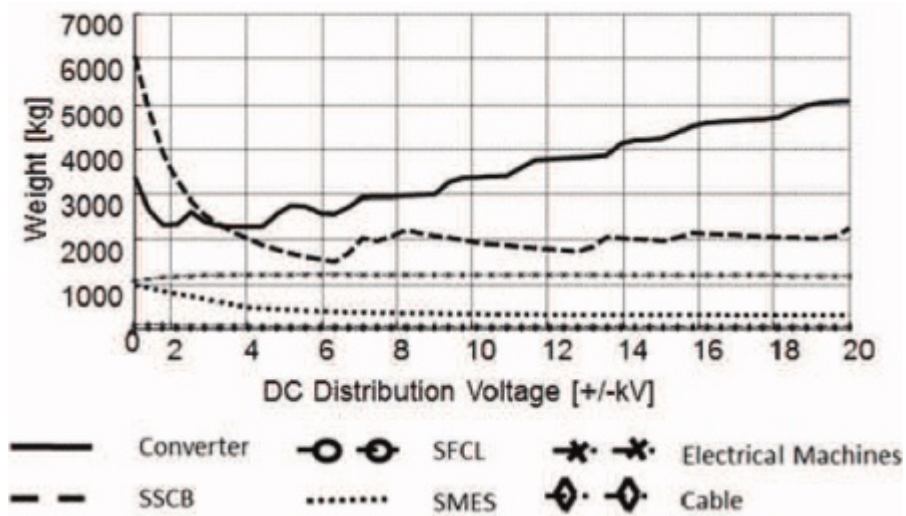
Figure 2.13: Voltage Weight Relationship for Superconducting TeDP Network Components [29]

Cryogenic System

In order to cool the HTS components to temperatures below T_C, a robust cryogenic system is required. The four main cryogenic system options described in the literature are [68]:

1. decentralised cryogenic system: Each component has an independent cooling system.

2. Partially decentralised cryogenic system: Localized cooling of network sections while maintaining a network of circulating cryogen fluid.

3. Centralized cryogenic system: Centralized cryocoolers provide cooling for the whole network of superconducting components.

4. Boil-off cryogenic system: Cryogen fluids are deposited into the network at the start of the mission and expended to keep components at nominal operating temperature.

A decentralised system allows for individual components to operate at their optimal temperature and the failure of any single cryogenic device is also limited to the affected

Component	Power Density (kW/kg)	Efficiency (%)
HTS Generator	78.5	99.3
HTS Propulsion Motor	47.1	99
HTS Cables	500 $A/kg/m$	≈ 100
Power Converter	40	99.8
Cryo-cooling System	0.333	30
DC Circuit Breakers	200	N/A

Table 2.1: Superconducting TeDP Component's Power Density and Efficiency Targets

component. Conversely a centralized system reduces the number of components in the aircraft, reducing complexity and allowing for system with less total mass [68]. A boil off system removes the need for the bulky cryocoolers. However a primary disadvantage of a boil off system is the need for airports to have the infrastructure to provide cryogen refuelling. This may limit the number of flight destinations as well as require significant investment to achieve widespread availability. The boil off system may also limit the cryogen fluid selection to inert elements such an LN_2 due to the obvious safety implications. Cryocoolers for TeDP are targeting a specific power of 3kg/kW [63].

2.2.3 Component Targets and Requirements

To achieve the power densities required to make superconducting TeDP economically feasible, component targets that have been identified in the literature are shown on Table 2.1 [63], [69], [70], [29]:

2.3 Superconducting Cable Design

2.3.1 HTS Wire Development and Properties

Early attempts to fabricate HTS materials into wires for creating electrical components lead to the creation of first generation (1G) HTS multi-filament wire. This was achieved in the early 1990's with the BSCCO material using a powder in tube (PIT) process [71]. As a result of this manufacturing process, the HTS material is encased by a metallic
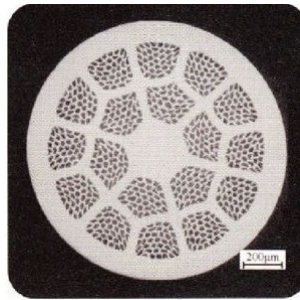
Figure 2.14: BSCCO Multi-Filamentary Wire [72]
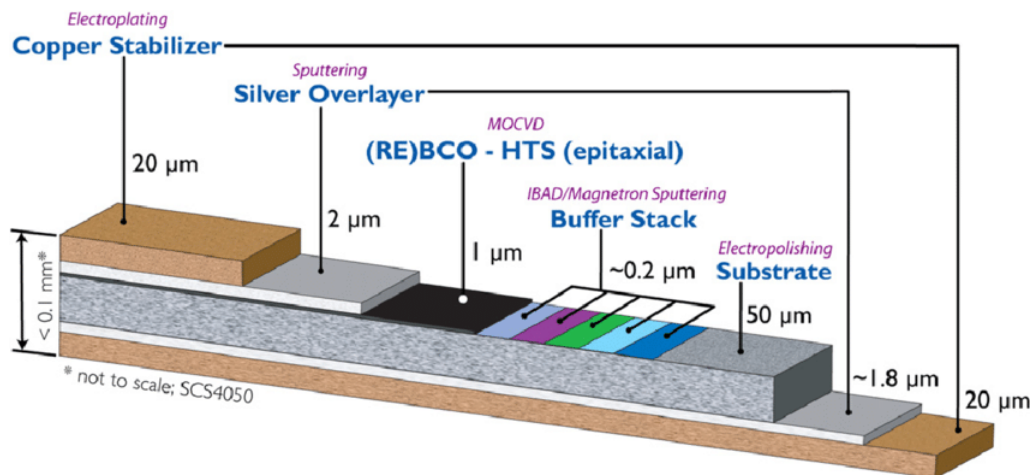
Figure 2.15: Structure of REBCO Tapes used to Produce Superconducting Components [76]

matrix of silver alloy. The cross section of a BSCCO wire made using this process is shown in Figure 2.14. While 1G multi-filament wires can achieve high current densities, as demonstrated by the trace for BSCCO in Figure 2.1, the use of the silver metallic matrix in its construction increases costs significantly [71].

Due to the high production costs of BSCCO wire, second generation (2G) HTS tapes have been developed. These have a structure as shown in Figure 2.15 and are create using a deposition process that adds rare earth elements with barium and copper oxide (ReBCO) to grow a thin film of superconductor on a substrate [73]. A major advantage of 2G tape is that it is primarily made up of inexpensive materials, allowing for cost savings compared to 1G cables [74]. In addition the manufacturing process can be automated providing further cost saving and scaling potential [75].

As well as the potential for reduced cost, 2G tape has a number of significant practical advantages over its 1G counterpart. First, 2G HTS tape achieves higher critical current densities at the same temperature [77]. 2G tape also has better magnetic field performance and greater mechanical properties, being able to withstand higher magnetic field and shorter pitch twists with less degradation to critical current [75] [74]. For the reasons outlined in this section, the work presented in this Thesis will focus on 2G HTS tapes and cables. From now onward in this work, when HTS is used it should be assumed that it is in reference to 2G HTS unless explicitly stated.

2.3.2 HTS Cables Designs

Cable design concepts

An example of a superconducting cable made using HTS tape is shown on Figure 2.16. As shown, this cable is a single core, cold-dielectric (CD) concept. This CD refers to the electrical insulation that, in this design, is kept within the cryostat and is thus kept at cryogenic temperatures [78]. The full design is made up of a variety of material layers. The innermost layer is the nitrogen inlet that allows the coolant to flow through the cable, removing heat generated by transmission and environmental losses. The nitrogen coolant is contained within the second layer, the former of the cable. This part of the cable is made of a conventional material which is generally copper, brass or stainless steel depending on the application. During a fault, the vast majority of the current will flow through this part of the cable due to the large impedance of the superconducting material at currents exceeding the critical current [79].

The next layer is the superconducting tapes. The tapes are wound around the former, with the final critical current of the cable being determined by the number of tapes used in the creation of the cable and the rating of each tape. Critical current degradation can occur due to the twisting of the tapes and the pitch angle is optimised to maximise critical current over the length of the line [81]. A second later of HTS tapes is used in the screening layer. During normal operation the HTS screen provides complete magnetic shielding as the current induced in the screen layer cancels the magnetic field produced in the conduction layer [82]. This ensures that the magnetic
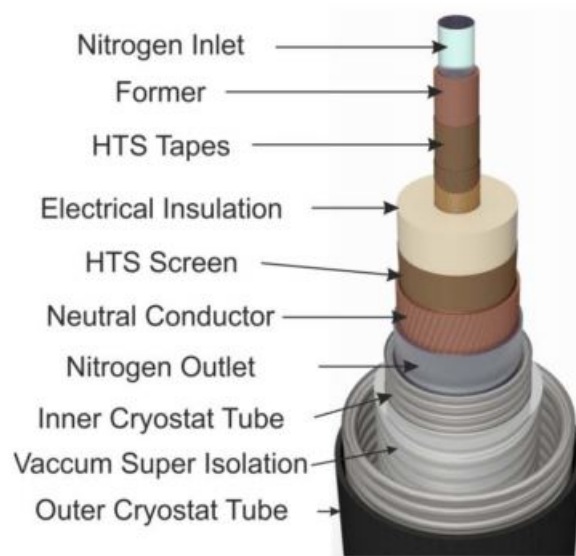
Figure 2.16: Single Core Cable Design [80]

field within the cable cannot interfere with other nearby circuits. A nitrogen outlet provides the coolant return path.

In contrast to the CD design, a warm dielectric (WD) cable design utilises electrical insulation on the outside of the cryostat. Figure 2.17 shows the different insulation design approaches for a three core cable concept in both warm and cold dielectric designs. A three core cable allows for three phase power distribution using a single cryostat. In the CD design presented the remaining volume inside the cryostat outside of the cores is used as the return path, submerging the dielectric in the cryogen.

A CD design exhibits lower AC-loss than a WD design and can have a higher transport current [82], [83]. However, the WD approach allows the use of conventional insulation material and uses less superconducting tapes since there is no shield layer [82]. This comes at the penalty of electromagnetic shielding. This allows CD designs to offer overall less volume as cable spacing is not a constraint [82]. As such, a CD design is better suited to TeDP than a WD design and will be the focus of this thesis going forward.
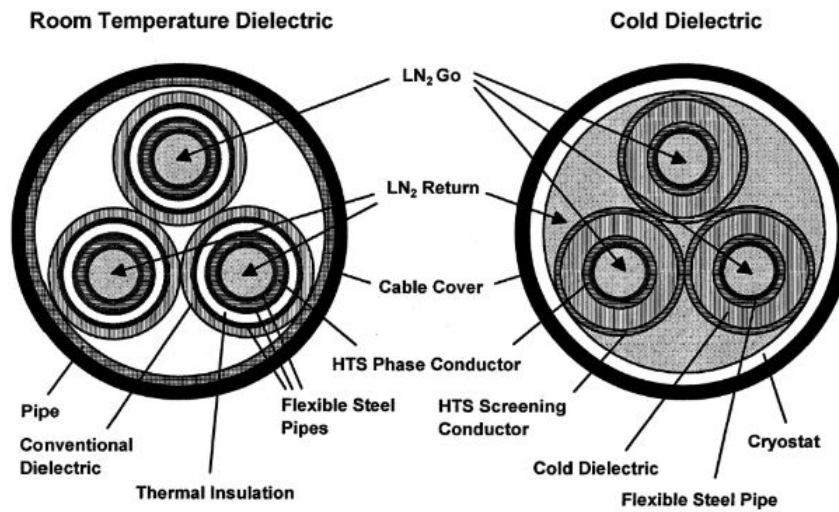
Figure 2.17: Three Core Cable Warm and Cold Dielectric Design [78]

Power Loss and Heat Sources in HTS Cable

The main sources for power loss in HTS cables are as follows:

1. Flux-creep and flux-flow loss: As the current in a superconducting cable increases, fluxons are able to overcome the energy barrier created by pinning sites. This causes a potential difference to be generated by the movement of the magnetic fluxons that leads to energy dissipation as current passes through these areas. [84].

2. AC loss (in AC system only): The three main drivers for this loss mode are the superconducting hysteresis effect, eddy currents induced in the conventional parts of the superconducting component, and coupling loss [84].

Within a DC system the main driver for losses are flux-creep and flux-flow. This loss mode can be minimised by maintaining sufficient margin between operating current and the critical current.

2.3.3 Fault Current Limiting (FCL) and Fault Current Tolerant FCT Cables

To design superconducting cables robust against electrical faults, two design approaches can be considered: the fault current tolerant (FCT) and fault current limiting (FCL) cable designs. The major difference between the two design choices is in the quenched impedance of the cable, which is altered by changing the type of material and thickness of the conventional materials that act as a parallel shunt during quench [85].

For the FCT cable, the former is made of highly conductive material such as copper, with a large enough cross sectional area to provide a high-volume, low impedance, path for the fault current to pass through during a fault scenario [86]. During a fault, the amount of energy dissipated does not result in a significant rise in temperature if the former is large enough [86]. Additionally, if the temperature rise is large enough to remove the cable from service, the time for the cable to recover will be reduced due to the lower temperature reached during the fault period.

A low impedance path can offer thermal stability during faults and small over-current transients for these reasons. However, the size of the former may introduce larger weight and volume penalties. A further drawback of this design is that the low impedance provided by the cable could lead to other components on the network dissipating a larger proportion of fault energy [87]. This will require other system components to be overrated to withstand the higher fault currents, incurring size and weight penalties which have a large impact on the performance (weight and efficiency) of the TeDP aircraft.

An alternative cable design is the FCL. The FCL design uses materials with a much higher impedance such as stainless steel for the tape Stabiliser and cable former, or smaller cross-sectional areas of higher conductive material. Hence, if fault current causes the superconducting material to go above the critical surface, it must travel through a highly resistive former. The resistive former can be sized to provide a large impedance that can limit the amount of fault current able to travel through the cable, reducing the amount of fault current experienced by other power system components [88].

The possibility to use the FCL cable design in a TeDP architecture will depend strongly on the available length of cable runs on the aircraft because the cable must have sufficient volume to area ratio to provide impedance while ensuring that the resulting temperature rise is not excessive. For instance, the authors of [89] present a FCL cable design concept but utilize a cable length of 19.8 km. In contrast cable lengths are unlikely to exceed 100 m given the dimensions of an aircraft. The resistive nature of the former used in the FCL design results in a greater possibility of hotspots occurring when the current levels are elevated. This is because of the reduced current sharing with the former during the initial moments of a fault and the significantly lower thermal conductivity of stainless steel (two orders of magnitude lower than that of copper) [90]. Hence the spread of the normal zone created by the hotspot could be slowed, leading to a smaller volume of material absorbing the fault energy as a result of the reduced normal zone propagation velocity (NZPV) [91]. However if fast acting, solid-state, circuit breakers (¡ 1ms) can be developed FCL cables may be able to reduce the impacts of capacitive discharge during a rail to rail fault without excessive temperature rise as is shown in [88].

Finally, from a protection perspective, FCL cables are 'one-shot' devices. A one shot protection device is only able to interrupt a fault once, and is not easily re-settable after use. In this sense, FCL cables will require time to re-cool to normal operating temperatures before being placed back into service. This may take a more significant period of time to achieve than in FCT designs, owing to the larger temperature rise during the fault period and the cooling required to resume the superconducting state. Due to the limitation of the cable run length on aircraft, to maintain the FCL capability, dedicated FCL devices may be required to operate with FCT cables and/or converters with FCL capability may be required (if a TeDP architecture requiring power electronic converters is selected).

2.4 Failure Modes of Superconducting Components

2.4.1 Critical Current Degradation

Critical current degradation is a reduction in the maximum current a superconducting component can carry without quench occurring at a given temperature. Degradation can occur as a result of a number of processes relating to the thermal, physical, and electrical stresses the superconducting material is subjected to during operation [92], [93]. During normal operation superconductors will be in a cryostable environment due to the need to maintain operating temperatures below the critical temperature. This means temperature will vary over a very small range during normal operation. This is in contrast to conventional distribution networks in which components regularly see temperature swings throughout the day due to short term weather conditions, and changes in electrical demand.

Thermal cycling is one of the main degradation mechanisms of conventional components as expansion and contraction of materials with respect to temperature can lead to defect formation and growth. By maintaining a cryostable environment superconductors are expected to have greater service life and lower maintenance requirements as a result [94].

Faults in superconducting systems can however cause large rises in temperature depending on the fault level of the system and the components heat capacity [85]. Temperature rise can be damaging to superconductors as exposure to high temperatures can cause a superconducting material's I_C to degrade [92]. For ReBCO material, research has shown that exposure to temperatures of 400 K or greater will lead to I_C degradation [95]. This failure mode can lead to greater losses in the short term as the difference between load current and critical current is narrowed. Significant critical current degradation due to heating could make the component unable to fulfil it's load conditions or lose it's superconducting properties completely [96].

Physical stress on the component can also lead to critical current degradation. Research conducted by the authors of [97] shows that the critical current varies due to tape bending and mechanical stress exerted on the tapes. TeDP is a distribution system

for an aircraft, which throughout the course of a flight can go through mechanical stress due to turbulence and normal flight manoeuvres and vibrations. The impact this can have on critical current over the lifetime of an aircraft is unknown.

2.4.2 Localised Thermal Runaway

Whilst quench provides an opportunity to dampen fault current through the sudden and large resistance increase of the material, large amounts of heat can be generated through this process due to Ohmic losses. If the quench is not managed through appropriate means, either through passive protection methods such as parallel shunts or active dump loads and heating mechanisms, severe damage to the component will occur [96]. An issue surrounding the quench behaviour of superconducting components is the prospect of a hotspot occurring. A hotspot is the result of a non-uniform quench, when one part of the component ceases to be superconducting before the remainder of it [98].

Hotspots can occur due to the difficulty in manufacturing superconducting components with consistent I_C along the entire length due to intrinsic microscopic defects [99]. The small size of the hot spot relative to the full size of the component means that a large current can still flow in the device as the resistance created by the quenched region is small, relative to the size of the component. This in turn means the hotspot can be forced to dissipate large amounts of heat for a period of time before the quenched zone spreads to the surrounding superconducting material and the quench becomes detectable, leading to a potential for damage [100].

Due to the relatively high heat capacity of high temperature superconducting components compared to their low temperature counterparts, the velocity at which the normal zone spreads throughout the superconducting component can be prohibitively slow [91]. This can be as low as centimetres per second [91]. Due to this potential for damage, a protection system for superconducting systems must be able to detect quench quickly.

Their small size and low propagation velocity can make hotspots very difficult to detect using conventional quench protection techniques, which are reliant on detecting

voltage drops across components [101]. Hotspots are most likely to occur due to over-current conditions that bring the superconductor to current levels near and above the boundaries of the superconducting state where current is not high enough to fully quench all parts of the material [102]. This means that it represents a failure mode that could occur at currents that components may be expected to ride through. Hence when designing the system, it may be necessary to over-rate components sufficiently to reduce the impact of this failure mode on the TeDP power network. However, increasing the amount of superconducting material used in the component will invariably impact its final cost.

A common approach to the protection of superconducting components involves minimising the damage caused by fault currents and hotspots through built in features. One such feature is the use of parallel paths of conventional material built into the material that provides an alternate path for current to flow through during quench [91]. This reduces the level of temperature rise experience locally due to the highly conductive nature of the materials used (typically brass or copper). These materials also have high thermal conductivity, allowing for heat dissipated to more quickly spread throughout the component, reducing the localised impact and damage from hotspots [91]. This is exemplified in Figure 2.18 which shows the current path for in a superconducting tape undergoing localised quench. This is the design approach taken for superconducting materials made from ReBCO tapes.

The authors of [103] present a method for preventing hotspots using parallel super-conducting shunt tape that creates a superconducting mesh network throughout the cable, allowing current to be redistributed amongst the superconducting tapes during transmission across the cable. This method can be shown to aid in equalizing the quench profile experienced by the individual tapes [103].

2.4.3   Thermal Runaway and Cryogenic stability

HTS components have significantly higher thermal stability when compared to low temperature superconducting components. This is due to the higher specific heat capacities of materials operating at higher temperatures [90]. Figure 2.18 shows the relationship
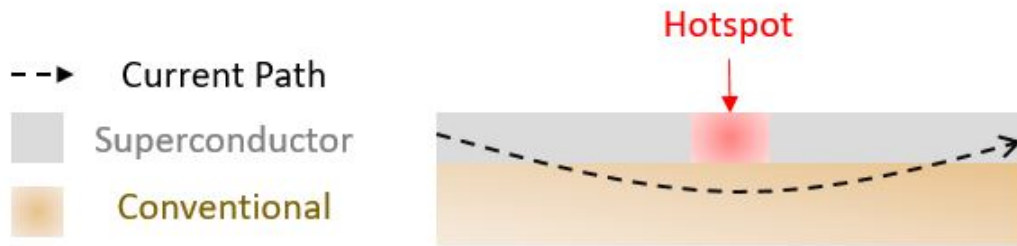
Figure 2.18: Parallel Shunt used to Redistribute Current into Conventional Conductors to Prevent Hotspot Thermal Runaway

between heat capacity and temperature for a range of conventional materials including brass, copper and stainless steel. These materials typically form the parallel shunt layers within superconducting components that carry current when the critical current is exceeded. It can be seen from this figure that as temperature increases, heat capacity increases and this relationship is particularly significant at low temperatures. As such, by operating at higher temperatures HTS components are able to dissipate more energy without enduring as great a temperature increase.

Cryostability is the term used to denote cryogenic conditions that are inherently stable, the energy put into the cryogenic system in the form of losses and intrusion is less than or equivalent to the energy removed from the system [105]. The opposite of this is thermal runaway in which the energy deposited into the system through loss mechanisms are greater than the energy that the cryo-cooling system is able to remove. This leads to uncontrolled temperature rise that can damage the component [105].

Temperature Margin

Figure 2.19 shows the relationship between current in a superconducting material and conventional shunt as a function of operating temperature. Temperature margin, ΔT (K), is the difference between the operating temperature, T_o, and the current sharing temperature, T_{cs} (K) [105]. T_{cs} is the temperature at which the current starts to flow in the conventional parts of the component. This leads to increased losses as Joule heating occurs in the conventional conductor within the component. As temperature
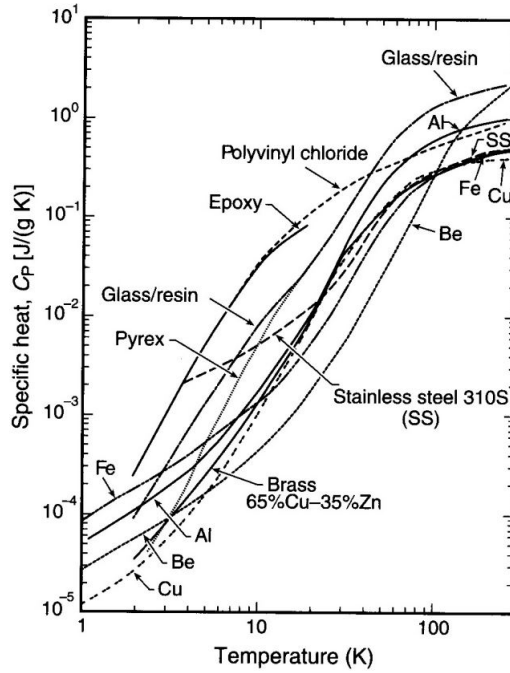
Figure 2.19: Heat Capacity of Conventional Materials with Respect to Temperature at Low Temperatures [104]

rise increases, more current is directed into the shunt material, increasing losses and therefore accelerating temperature rise [105]. Once the material reaches T_c (K) virtually all of the current is flowing in the conventional conductor.

Requirements for Cryostability

In the absence of cooling, the conditions of cryostability, steady state operation of the superconductor without thermal runaway, are as follows. The amount of thermal energy added to the system, ΔE_T (K), must be less than the amount of energy required to cause the superconductor to reach T_{cs}. This can be calculated using the component's heat capacity, c (J/K), and the difference between the operating T_o and current sharing temperatures [105]:

$$\Delta E_T \leq \int_{T_o}^{T_{cs}} c\,dT \tag{2.2}$$

Once the current sharing temperature is reached, Joule heating will lead to thermal
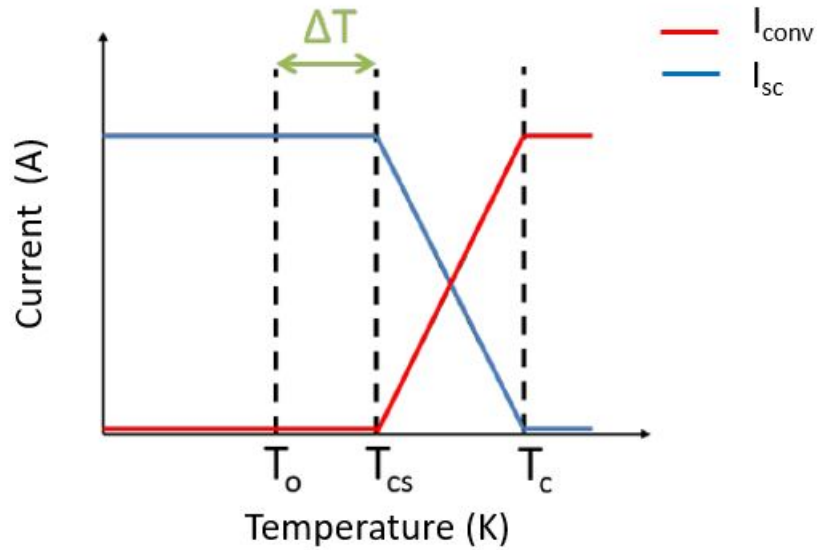
Figure 2.20: Current Sharing Between Superconducting and Conventional Materials with Respect to Temperature

runaway unless current is removed. In practical conditions, the cooling system's impact on cryostability needs to be considered. The amount of heat that can be transferred to the cooling system, $Q_{out}(W)$, depends on the heat transfer coefficient, $h(W/m^2)$, the surface area, $A(m^2)$,and the difference between operating temperature of the component and the coolant, T_{cool}. In the simplest case of a linear heat transfer relationship this can be expressed by [105]:

$$Q_{out} = hA(T_o - T_{cool}) \tag{2.3}$$

The heat transfer coefficient is dependent on a number of variables including the contact surface area, the type of cryogen, the matter state of the cryogen, and its flow properties. This results in a highly non-linear relationship between heat transfer coefficient and temperature [105]. However, in order to keep the focus of the analysis contained within this thesis on the electrical system, a linear relationship is adopted throughout this Thesis.

Current Margin

The current margin, ΔI (A), describes the difference between the operating current, I_o and the current level that will cause current sharing with the conventional parts of the component to occur, I_{cs}. In an ideal superconductor I_{cs} is the I_C at T_o.

2.4.4 Faults in Compact Superconducting DC Electrical Systems

Electrical propulsion for TeDP requires the generation, distribution, and consumption of 25 MW of power within a confined space and is subject to strict reliability requirements: for twin-engine aircraft, 180-minutes extended twin engine operations (ETOPS) requires an engine in-flight shutdown rate of less that 0.02 per 1000 flight hours [106]. To disrupt the market, TeDP will need to demonstrate that it can meet and exceed the standards set by the modern aircraft drive train. However, electrical faults cannot be prevented in any electrical system, they can only be mitigated through the use of activate and passive fault management strategies. The efficacy of a fault management strategy depends on the architecture of the system they are intending to protect. While there are benefits and drawbacks to both AC and DC electrical propulsion architectures for TeDP, this Thesis will focus on the impacts of faults within DC superconducting networks due to the greater controllability this network offers to the sTeDP concept.

Within conventional DC networks, the electrical system transient fault response is determined by the nature of the power electronics used to interface the generation source with the rest of the network [62]. This is primarily due to the filtering components (inductors and capacitors) used within the converter to improve the quality of power transfer between the AC and DC circuits by reducing voltage and current oscillation. These components impact faults due to the energy stored in the electric and magnetic fields they create as part of normal operation.

In the case of a highly inductive filter, such as that found in a current source converter, the large inductance can reduce the severity of the fault by limiting current [107]. In the case of a capacitor dominated filter, such as that found in a voltage source converter (VSC), a large discharge of current can occur due to the electric field stored on the capacitor plates at the time of a short circuit fault. This discharge of current can

cause damage to components in the fault path, and the converter itself [108]. Within a superconducting network, the negligible resistance of superconducting feeders could lead to rapid generation of, and high peak values of fault current [88] which will also lead to quench within the superconducting feeder cables. This near instantaneous change in resistance will further affect the dynamics of the fault response of the superconducting network when compared to a network made with non-superconducting components.

While previous work has been done on conventional compact DC networks [62], it remains to be seen how much of this knowledge is directly transferable given the unique operating characteristics of superconducting components. The impact of DC faults on a compact, power electronics interfaced, superconducting network, are not well understood and the implications of these transients on system and component design need to be considered in any TeDP solution. This Thesis will first investigate the response of superconductors within power electronically interfaced networks using VSCs and the potential for superconducting component damage due to high and over-current conditions caused by the capacitor discharge during a fault.

Chapter 3

Fault Behaviour of Superconducting TeDP Networks

3.1 Fault Behaviour of Conventional Power Electronic Interfaced DC Systems

This chapter focuses on the general behaviour of superconducting tapes in converter interfaced systems under short circuit conditions. This begins with a review of the fault analysis in conventional VSC DC systems to form a basis for comparison with a superconducting system and demonstrate why the same methods used for conventional networks cannot be directly applied to their superconducting counterparts. This will be done through the development of superconducting tape models, produced from literature and simulations within Matlab's Simulink software package. This analysis is then extended through experiments to capture impact that DC faults can have on superconducting components.

To this end, Section 3.1 focuses on the fault behaviour of a conventional rectifier interfaced DC distribution network. Section 3.2 describes the superconducting modelling process that is used to allow for superconducting tapes to be embedded within a circuit model. Section 3.3 focuses on the RLC response of superconducting tapes, characterising the initial capacitor discharge phase of a fault on a superconducting DC-link for underdamped, critically damped and overdamped systems. Section 3.4 describes the
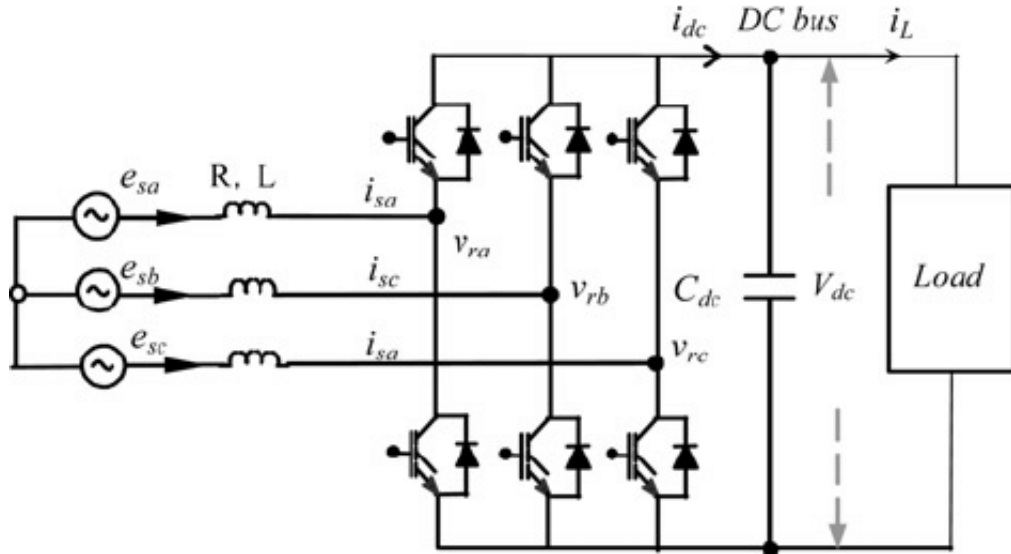
Figure 3.1: Circuit Diagram of Three-Phase VSC with Filtering Capacitor and Load Resistor [109]

capacitor discharge experiments which demonstrate the physical response of superconducting tapes to a large pulse of current similar to that which would be experienced during the initial moments of a DC-link fault. Section 3.5 concludes this chapter.

3.1.1 Rectifier Interfaced Fault Behaviour

A conventional DC link is interfaced in terrestrial systems using power electronics. These power electronics contain switches and filtering elements that allow for the high quality conversion of power from AC transmission mode to the DC mode. While vital for reducing circuit noise these filtering elements ultimately have a profound impact on the shape of the fault response of the network, and the severity of the faults experienced [62]. A three phase active rectifier converts power from AC to DC using diodes to ensure the current flows in a single direction, while switches are used to control the power flow as required. The fault behaviour of VSC interfaced DC link can be analysed with the following circuit [109]:

This circuit is connected to a distribution line. When an ideal rail-to-rail short circuit occurs on this network, the voltage at the fault location generally drops to zero due to the very small impedance of the fault path [62]. This causes the filtering
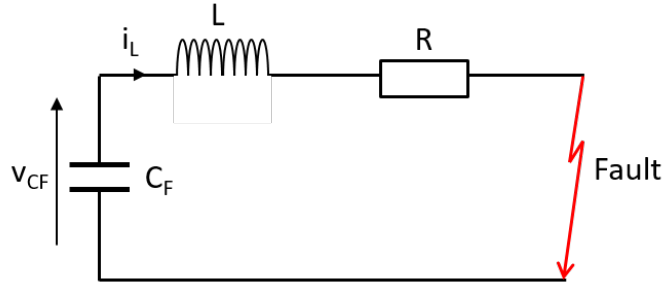
Figure 3.2: RLC Fault Discharge Circuit

capacitor to discharge into the fault path, leading to extremely high currents as the impedance between the locations is very low [62]. This is the first stage, known as the capacitor discharge stage, of a DC-fault response and takes place in microseconds within compact, low-inductance systems. The second stage of a VSC interfaced DC fault is the shoot-through current stage. As the capacitor discharges through the fault, the voltage across it decreases and as a result of this the voltage can become negative leading to large currents flowing through the rectifier diodes as they are unable to block the flow of current [108]. This current can potentially destroying the diodes [62]. The third stage of the fault current is the steady-state fault response.

Stage 1: Capacitor Discharge

The initial capacitor discharge can be analysed by considering a series RLC circuit with a fault path as shown in Figure 3.2 [110]. With given component values for filter capacitor size, line inductance, and resistance, the variable states, the fault current and capacitor voltage, can be calculated by considering the natural response of the circuit. This circuit can be modelled using the 2nd order linear differential equation shown in (3.1):

$$L\frac{d^2 i_L}{dt^2} + R\frac{di_L}{dt} + \frac{1}{C_F}i_L = 0 \tag{3.1}$$

Where i is the instantaneous current, L (H) is the inductance of the circuit, $R(\Omega)$ is resistance, and C (F) circuit capacitance. Taking the Laplace transform of this and putting it into standard form the following characteristic equation is obtained:

49

$$s^2 + \frac{R}{L}s \pm \frac{1}{LC_F} = 0 \tag{3.2}$$

Solving for the roots of this equation leads to:

$$s = -\alpha + -\sqrt{\alpha^2 - \omega_0^2} \tag{3.3}$$

Where α is the damping factor and ω_0 (rads^{-1}) is the natural frequency of the circuit. These are calculated in (3.4) and (3.5) respectively:

$$\alpha = \frac{R}{2L} \tag{3.4}$$

$$\omega_0 = \frac{1}{\sqrt{LC_F}} \tag{3.5}$$

These values determine the nature of the response, whether it is over-damped, under-damped or critically damped in accordance with the following conditions [111]:

- Over-damped: $\alpha > \omega_0$. Under this condition the circuit is the sum of two exponentially decaying components with no sinusoidal oscillations. This causes the circuit to reach steady-state very slowly without any oscillations.

- Critically damped: $\alpha = \omega_0$. Under this condition the current decays exponentially without a sinusoidal component. The circuit reaches steady-state without any oscillations in the shortest possible time.

- Under-damped: $\alpha < \omega_0$. Under this condition the circuit response leads to a decaying sinusoidal oscillation. The circuit responds fast but oscillates around steady state.

Figure 3.3 illustrates the over-damped, critically damped, and under-damped response of a second order system.
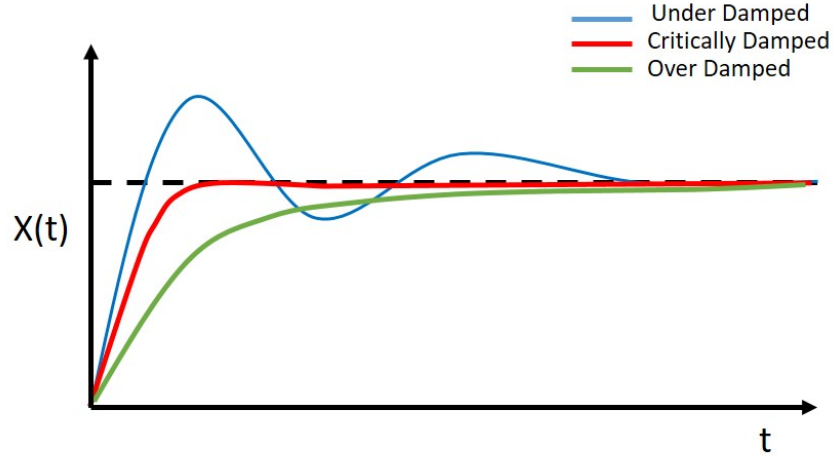
Figure 3.3: Example of Under, Over, and Critically Damped System's Step Response

Stage 2: Diode Continued Flow Stage

This stage occurs as the capacitor discharges and energy becomes stored in the inductance of the fault circuit. In this stage the voltage across the capacitor drops significantly and can even be reversed if the system is significantly under-damped [110]. During this event, the fault current circulates through the anti-parallel diodes of the power converter, which are required to prevent arcing during normal switching cycles. Because of the size of this current, the anti-parallel diodes are at high risk of being destroyed [112]. This current decreases exponentially in accordance with the RL time-constant of the fault circuit:

$$i(t) = I_0 e^{-(\frac{R}{L})t} \tag{3.6}$$

Where I_0 is the peak magnitude of the discharge current.

Stage 3: Steady State Fault Current

The final stage of the DC fault is the steady state current that flows into the faults from the power generation source upstream of the converter [113]. In this stage the switches are blocked and the converter behaves as an uncontrolled rectifier discharging into a fault [113]. The current contribution of the AC system, which produces the
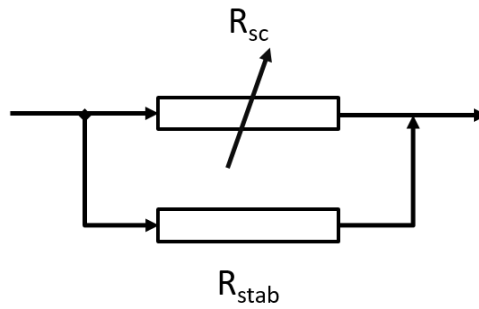
Figure 3.4: Circuit Model of Superconducting Tape

steady state fault response,I_{abc} is the sum of the positive three phase fault currents:

$$i(t) = \Sigma I_{abc}(t) \tag{3.7}$$

Where I_{abc} is the current contribution of each phase.

3.2 Modelling Superconducting Cables for DC Faults

While conventional DC systems have broadly constant resistance, superconducting components have to consider the impact of quench and temperature on the resistance of the component. For instance during normal operation superconducting material has near zero resistance to the flow of current, hence by inspection of (3.4), this will result in a system that is very under-damped under fault conditions. However as the current rises the superconducting material undergoes quench and becomes highly resistive, making the system appear over-damped.

Development of the superconducting cable model first requires the formulation of a superconducting tape. Superconducting ReBCO tape, as shown earlier in Figure 2.15, contains both a superconducting layer and a layer of conventional material to provide stabilisation. Electrically this is viewed as shown in Figure 3.4, with the superconducting material, R_{SC}, being in parallel with the Stabiliser material, R_{stab}.

3.2.1 Power-Law Model

The superconducting material can be modelled, below the T_C, using the power law model [114]. This approach models the superconducting material's electrical field in accordance with the ratio of operating current $I(t)$ to temperature dependent critical current $I_c(T)$ set to the power of the materials transition index n as shown in (3.8).

$$E(I) = E_0 \left(\frac{I(t)}{I_c(T)} \right)^n.$$
(3.8)

E_0 is the quench constant, commonly taken as 1μ V/cm. Once the component exceeds this value it is said to have quenched. The transition index, n, describes the starkness of the transition between the superconducting and conventionally conducting states [115]. The transition index can be derived from experimental measurements [114]. While Low Temperature Superconductors (LTS) superconductors had relatively high transition indices, creating steep differences in the impedance values above and below the critical current, HTS materials typically have smaller n-values [84]. This causes the transition between the superconducting and conventionally conducting modes to be less stark for HTS materials. This is demonstrated in Figure 3.5 which shows the IV characteristic of a superconducting material with respect to the transport current to critical current ratio.

The temperature dependence of the superconducting material is calculated in accordance with (3.9) [116]:

$$I_c(T) = I_{cref} \left(\frac{T_c - T(t)}{T_c - T_{ref}} \right)^k$$
(3.9)

Where k is the temperature dependence coefficient, T_{ref} (K) is the reference temperature, I_{cref} (A) is the critical current at the reference temperature. T_C is the critical temperature. (3.9) can be assumed linear, k equal to unity, between 77 K (the boiling point of LN$_2$) and T_C for ReBCO tape [116]. The transition index, n value, of HTS materials is temperature dependent as well and can be modelled using the relationship given in (3.10) [91]:
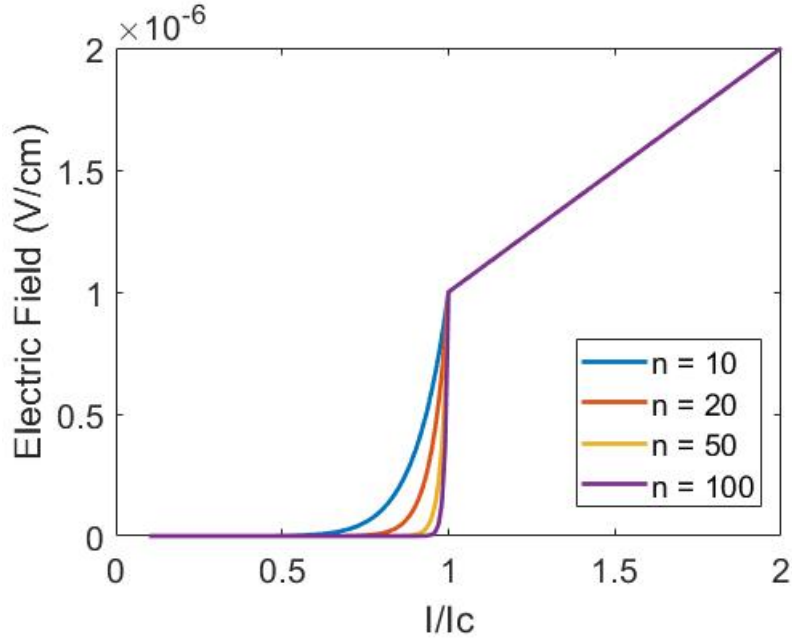
Figure 3.5: Impact of Transition Index on Quench Curve Steepness

$$n(T) = \frac{n_{ref} - 1}{2}(\frac{T_c - T(t)}{T_c - T_{ref}})^\zeta + 1 \tag{3.10}$$

Where ζ is the temperature dependence coefficient. The electric field generated by the superconducting material creates an impedance against the flow of current. The resistance of this is can be calculated according to:

$$R_{sc} = \frac{\frac{E(t)}{J(t)}L}{A_{sc}} \tag{3.11}$$

Where A_{sc} (m^2) is the area of the cross-sectional area of the superconducting tape, $J(t)$ (A/m^2) is the instantaneous current density, and l (m) is the length of the tape. The resistance of the Stabiliser is calculated by (3.12):

$$R_{stab} = \frac{\rho L}{A_{stab}} \tag{3.12}$$

Where $\rho(\Omega.m)$ is the resistivity of the Stabiliser material and A_{stab} is the cross-sectional area of the Stabiliser.

3.2.2 Current-Iterative Method

To analyse the current distribution between the superconducting part of the tape and conventionally conducting part, the current sharing equation between two parallel resistors can be used (3.13):

$$I_{stab} = I_{tot} \frac{R_{sc}}{R_{sc} + R_{stab}} \tag{3.13}$$

Where I_{tot} is the total current flowing in the tape and I_{stab} is the current flowing in the stabilising layer. However because R_{sc} is directly dependent on the amount of current in the superconducting material, an algebraic loop is formed which can lead to incorrect results and long simulation times. To prevent this the current sharing between the superconducting and conventional layers can be calculated using a current-iterative method (CIM), demonstrated in [117]. The CIM iteratively calculates the current in the superconducting layer until it converges on the correct solution and is described by the flow diagram in Figure 3.6.

The CIM works by taking an initial estimate of the current in the superconducting layer, I_{HTSOLD}, that is calculated by using the resistance value of the HTS material in the previous time-step, R_{HTSOLD} [117]. This value is then used to calculate the resistance of the HTS layer under the present current-temperature conditions, R_{HTSNEW}. Using this new resistance value, the amount of current in the superconducting layer, I_{HTSNEW}, is recalculated in accordance with (3.13). The new value for the current in the HTS layer and the previous value is compared to determine the error between iterations as shown in (3.14) [117].

$$Error_{NEW} = 100 \frac{I_{HTSNEW} - I_{HTSOLD}}{I_{HTSNEW}} \tag{3.14}$$

If the error value between iterations is below the tolerance threshold, then the CIM has solved the current sharing problem and the equivalent impedance is determined and can be used in solving the wider circuit equations. The equivalent resistance, R_{equiv} seen by the rest of the circuit is calculated in accordance with the parallel resistance rule as shown by (3.15):
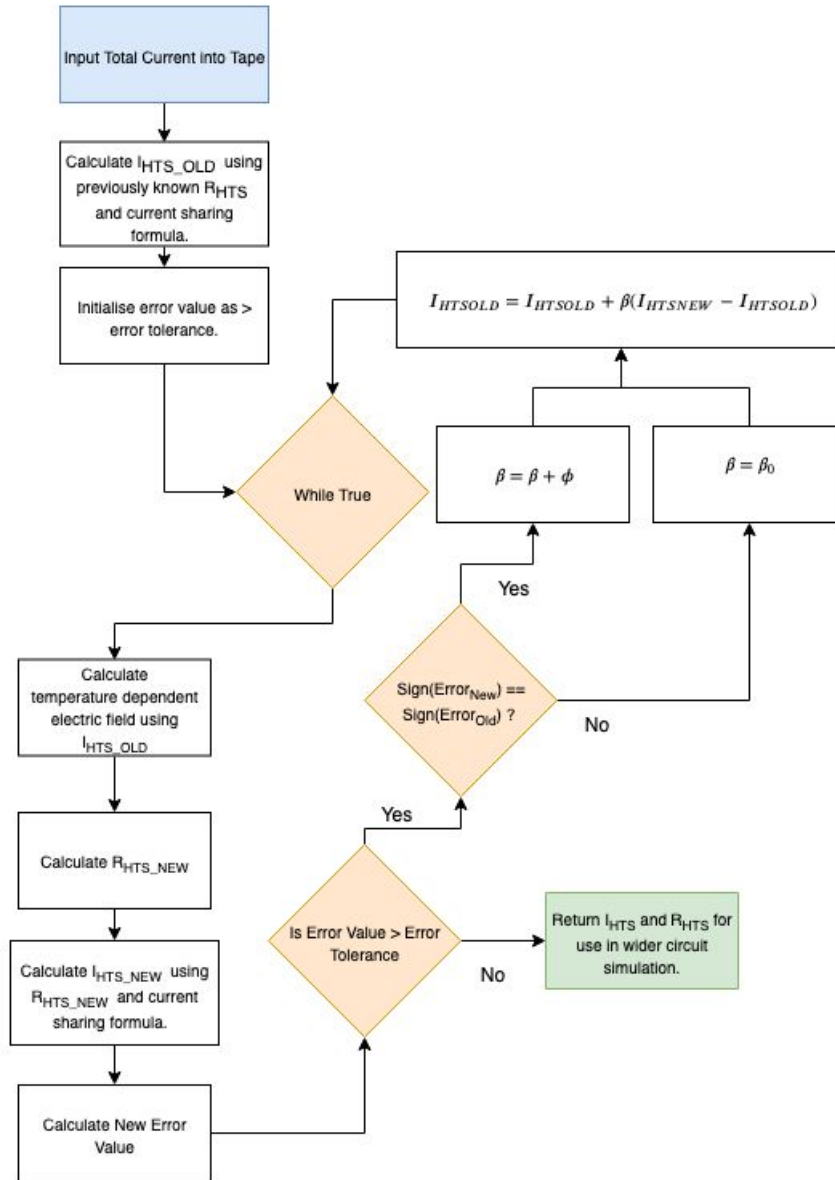
Figure 3.6: Flow Diagram of CIM Implementation

$$R_{equiv} = \frac{1}{\frac{1}{R_{sc}} + \frac{1}{R_{stab}}} \tag{3.15}$$

However, if the error value is greater than the required tolerance threshold then another iteration is required. This next iteration uses the information gained from the previous calculation to create a new guess of the amount of current in the HTS layer based on a fraction of the difference, β between the initial guess and the calculated result [117].

$$I_{HTSNEW} = I_{HTSOLD} + \beta(I_{HTSNEW} - I_{HTSOLD}) \tag{3.16}$$

The value for β can be modified by a constant value, ϕ, when the program detects that the solution is likely above or below the current search area [117]. This is done by comparing the signs of the two previous error values. This allows amplification of movements in either the positive or negative direction to increase convergence on the correct result during large changes in current and temperature.

3.2.3   Simulink and Thermal Modelling

The superconducting tape is modelled thermally by considering the amount of heat input into the system through dissipation in the superconducting and stabilising layers of the material. The electric field created by the superconducting component during quench produces a potential difference which must be overcome by the flow of current in order to transmit power. This leads to losses in accordance Ohmic heating. In addition, current flowing in the stabilising shunt will experience Ohmic losses due to the resistance of the material. The total energy dissipated in the tape is calculated according to the voltage drop, $V(t)$, and current carried by the tape, I_{tot}, as shown in (3.17).

$$Q_{in}(t) = I_{tot}(t)V(t) \tag{3.17}$$

Where $Q_{in}(J)$ is the instantaneous energy dissipation. The temperature rise of the tape due to this power loss can be calculated using (3.18) where Q_{out} is the heat

removed by the coolant.

$$T = \frac{1}{c_{tot}} \int_{t_0}^{t_{end}} Q_{in} - Q_{out} dt \tag{3.18}$$

The total heat capacity, c_{tot} of the superconducting tape is calculated in accordance with the volumetric heat capacity equation:

$$c_{tot} = \sigma V_u c_{cv} \tag{3.19}$$

Where σ is the density of the material in kg/m^3, V_u is the volume of the tape in m^3, and c_{cv} is the heat capacity of the material per unit volume.

The superconducting tape can be modelled in MATLAB's Simulink software package according to the block diagram in Figure 3.7 which shows the process that Simulink follows in its execution of the model. The superconducting tape is implemented using a controlled voltage source that is embedded within a wider circuit model created in Simulink's power system library. While the rest of the circuit is modelled as a traditional electrical system, the controlled voltage source of the superconductor will change its electric field strength, in accordance with the equations developed in this section, depending on its internal temperature and the current flowing through it.

3.3   Analysis of Superconducting Tape RLC Response

3.3.1   Overview

The response of a superconducting tape to the discharge of the capacitor is significantly affected by the tape design, in terms of superconducting and Stabiliser CSA, as well as circuit parameters. At the instant of the capacitor discharge, the circuit has very low damping, leading to a high rate of change of current. This can result in a very large peak current discharge, which can be an order of magnitude above the critical current. As this current rises above the critical current, the tape quenches and current is diverted into the stabilising layer. This is exemplified in Figure 3.8 which compares the current in the superconducting layer and the stabilising layer of the tape over the
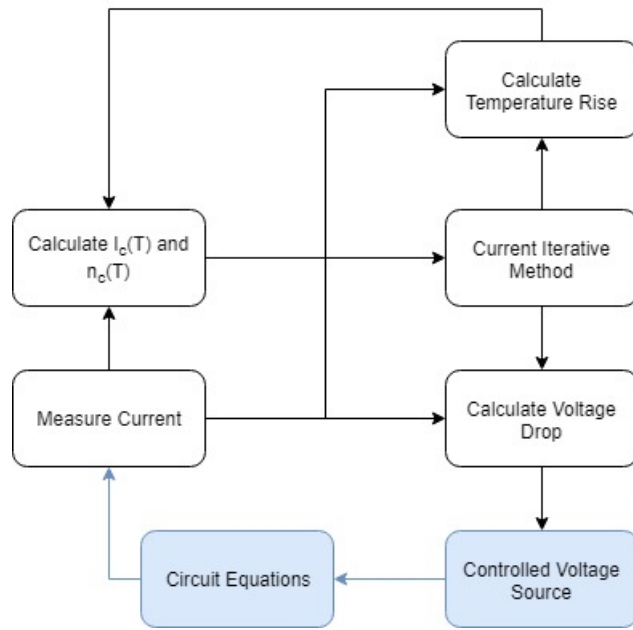
Figure 3.7: Flow Diagram of Simulink Model Implementation

course of a single capacitor discharge simulation.

During the response, energy is dissipated in the tape due to the voltage drop created along the superconducting and resistive layers as a result of the current flow. This causes the temperature to rise within the tape, depressing the critical current and causing more current to be directed into the resistive Stabiliser. This has the macroscopic effect of increasing the resistance of the discharge path which will continue until all of the current is contained within the Stabiliser. At which point, the total resistance produced by the tape is equal to R_{stab} (3.15).

Whether the circuit ultimately exhibits an over, under or critically damped response depends on the tape reaching the critical temperature, and the impedance it is subsequently able to provide. This is assuming that the fault resistance is significantly lower than the quenched resistance of the circuit, which may not be the case for all faults.

3.3.2 Requirements for an Underdamped Response

Figure 3.9 shows the current profile of an underdamped, superconducting RLC circuit, created using Simulink. The response of the superconducting tape can be separated
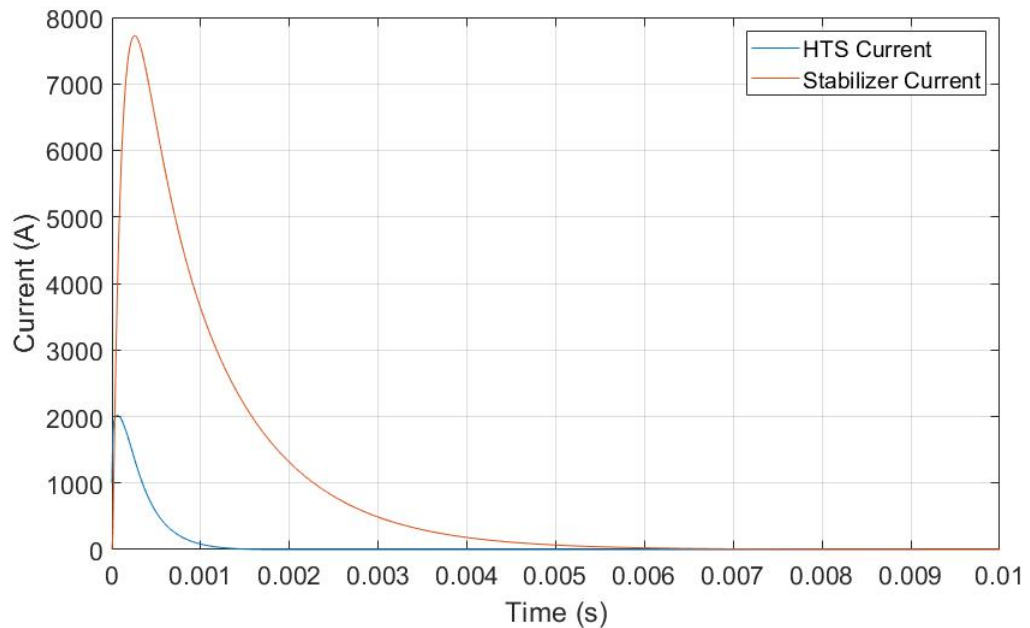
Figure 3.8: Current in HTS Layer and Conventional stabilising Layer Throughout Simulation

into three main stages. In the first stage, which lasts microseconds to milliseconds, the current rises rapidly due to the low impedance of the circuit. The second stage occurs once the current exceeds I_C. In this stage current begins to transfer from the superconducting layer to the resistive Stabiliser. Ohmic losses then cause heating in the superconducting tape (Figure 3.10), and the resistance of the circuit rises (Figure 3.11).

This stage continues until an equilibrium is reached, where the energy remaining in the circuit is no longer able to cause the current to exceed I_C. The temperature of the tape stops rising and the resistance begins to reduce with each successive cycle. In the third and final stage the current oscillates until the resistance of other sources in the circuit are able to dissipates the energy. In this example, that would be the resistance of the fault path. Superconducting AC loss mechanisms would also dissipate energy in this stage but its effect is assumed to be negligible compared to the fault impedance.

From observation it can be stated that the system will exhibit an underdamped response if the following conditions are met. Firstly, the resistance of the fault must be
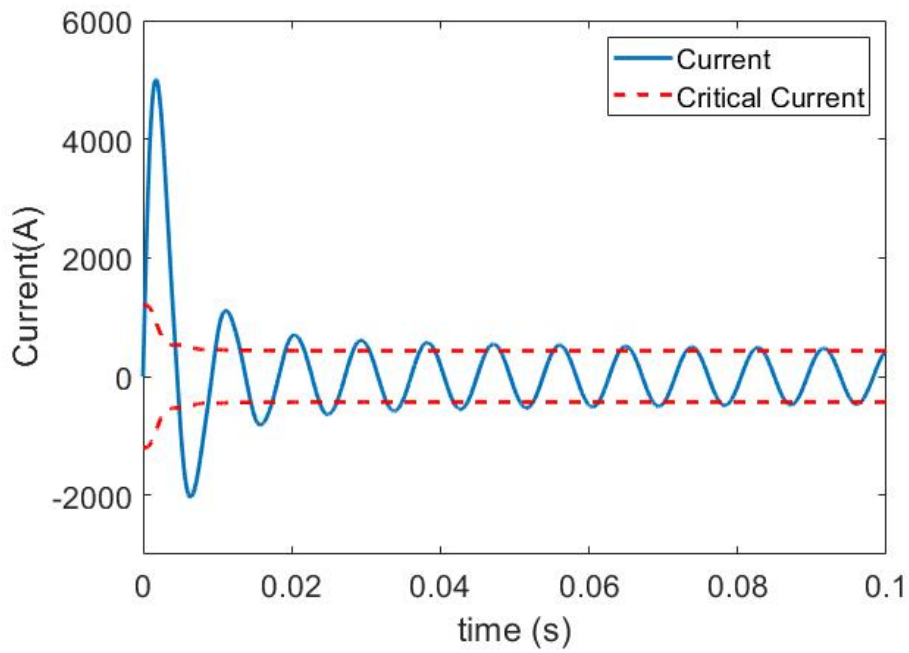
Figure 3.9: Current Profile for Underdamped Superconducting RLC Circuit
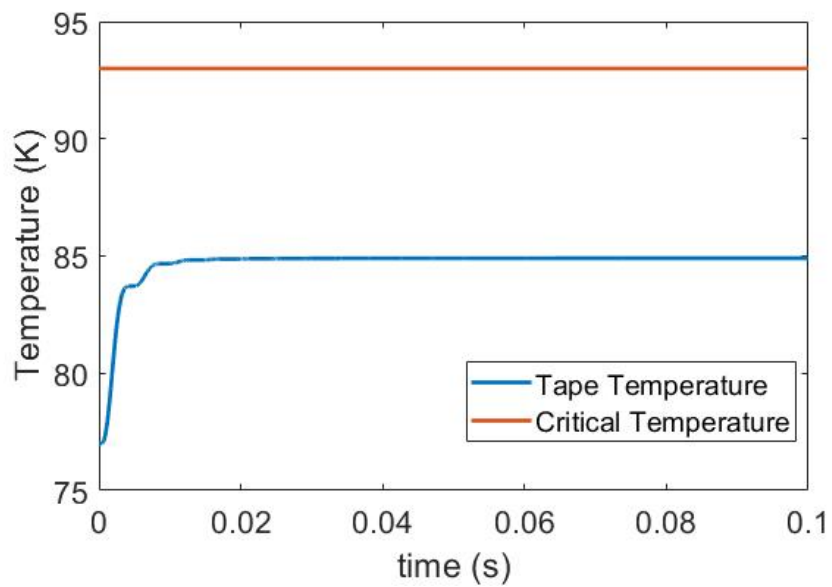
Figure 3.10: Temperature Profile for Underdamped Superconducting RLC Circuit
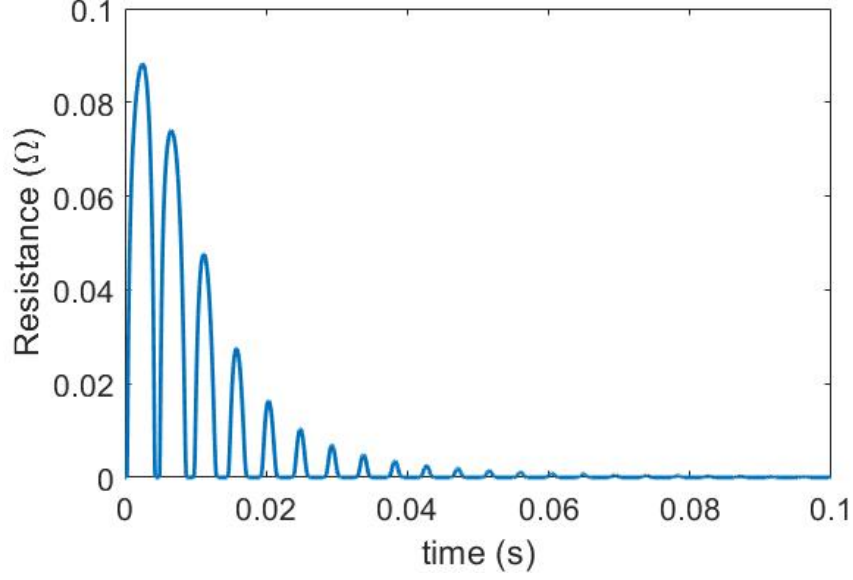
Figure 3.11: Superconducting Tape Resistance During Simulation

less than R_{crit}, the value of resistance required to produce a critically damped response, which can be calculated by setting (3.4) and (3.5) equal to each other and solving for R.

$$R_{fault} < R_{crit} \tag{3.20}$$

Secondly, the energy stored in the capacitor must be insufficient to quench the superconducting tape. This condition is expressed in (3.21). Quenching of the superconducting tape must also take place within the first half-cycle of the discharge (before the current reverses) to prevent an oscillatory response.

$$\frac{1}{2}CV^2 < \int_{T_O}^{T_C} H_{sc} dT \tag{3.21}$$

Additionally, it can be shown that the system will also exhibit an under damped response if the resistance of the circuit post quench is unable to provide sufficient damping. This is the case demonstrated in Figure 3.12 which shows current overshoot despite quench taking place and the critical current reducing to 0.
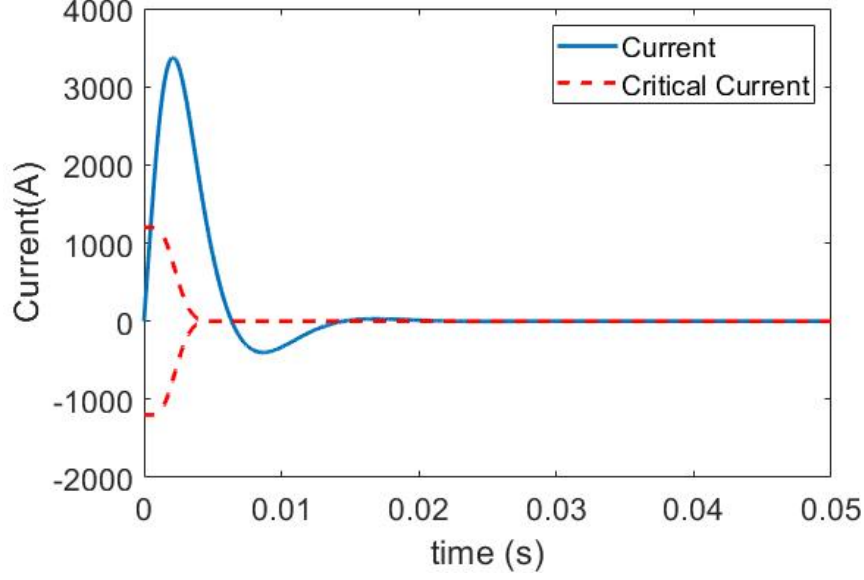
Figure 3.12: Underdamped Response in Superconducting RLC Circuit Due to Lack of Quenched Resistance

3.3.3 Requirements for a Critical or Over-Damped Response

Section 3.3.2 defined the conditions for an underdamped response. From these requirements the conditions under which the circuit will exhibit a critical or over-damped response can be determined. Firstly if the resistance of the fault is greater than R_{crit}, the circuit will exhibit a critical or overdamped response.

$$R_{fault} > R_{crit} \tag{3.22}$$

If the resistance of the fault is less than R_{crit} then the tape can still exhibit a critically damped response if the superconducting tape quenches and contains enough resistance to prevent oscillations. In order for the tape to quench the energy stored in the capacitor must satisfy (3.23) and be fully dissipated within the first half cycle.

$$\frac{1}{2}CV^2 > \int_{T_O}^{T_C} H_{sc} dT \tag{3.23}$$

A baseline case is evaluated that is able to provide a critically damped circuit response. Given the number of competing circuit and design variables that affect the

Parameter	Unit(s)	Value
Tape Operating temperature	K	77
Critical Temperature	K	93
Critical Current	A	1200
DC Link Voltage	V	1000
Tape Length	m	100
Stabiliser Resistance	Ω	0.11
Tape Inductance	H	$1e^{-5}$
DC Link Capacitance	mF	1
Resistivity at $77K$	$\Omega.m$	$2e^{-9}$

Table 3.1: Simulation Parameters for Base Case

response of superconducting tapes and the lack of analytical solutions to the circuit problems, a batch simulation is conducted to determine the dependence of these values on meeting the criteria for over, under, and critically damped circuit responses.

From the batch simulation a critically damped case is first identified with the circuit and material parameters detailed in table 3.1.

The rest of this section will define the relationship that each variable has with the required Stabiliser resistance to provide critical damping. To do this each variable in the base case is altered in turn, and the new value of Stabiliser resistance required to provide critical damping is determined.

To determine the R_{stab} value required for critical damping, each time a variable is changed a simulation is run. A scripting program in Matlab determines whether the new response is under-damped or not. If the response is under-damped the Stabiliser resistance is increased for the next simulation. Otherwise, if the program determines an overdamped response, it will take action to determine whether the response is critically damped. It will do this by varying the Stabiliser resistance slightly, searching nearby solutions to see if they exhibit a faster response that does not contain overshoot.

Tape length

A consequence of (3.23) is that increasing length of the tape can decrease the damping it provides if the area of the Stabiliser is kept the same (Ω/m constant). This is in stark
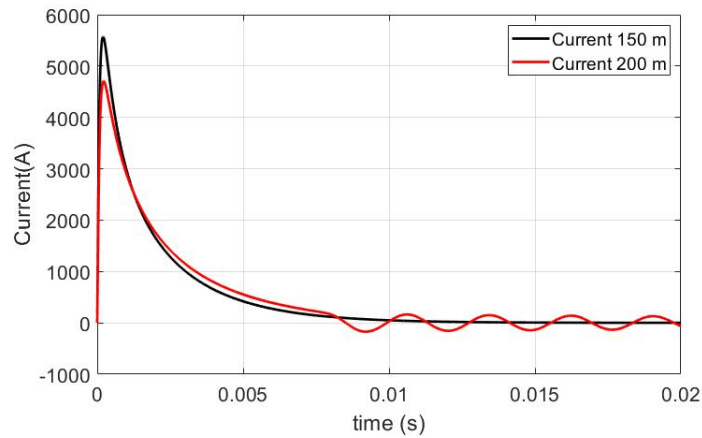
Figure 3.13: Comparison of Critically damped and Underdamped Response for Tapes of Different Length (Change this to show 100m Case)

contrast to conventional cables which typically provide greater damping as resistance increases proportionally with length for all operating currents. This can be seen in Figure 3.13 which shows that while a longer tape reduces the peak current the circuit experiences, the circuit begins to oscillate as the energy of the capacitor is insufficient to drive the temperature above T_C due to the greater heat capacity of the longer component.

Figure 3.14 shows the variation in quench resistance required for a critically damped system and tape length. This relationship can be modelled with (3.24). This approximation is created in Matlab's curve fitting toolbox and is found to have an R-square value of 0.995 and a sum of squares error (SSE) of $3e^{-4}$, signalling good agreement with the simulated results.

$$R_{Q_c} = 1.328e^{-5}l_e^{1.964} \qquad (3.24)$$
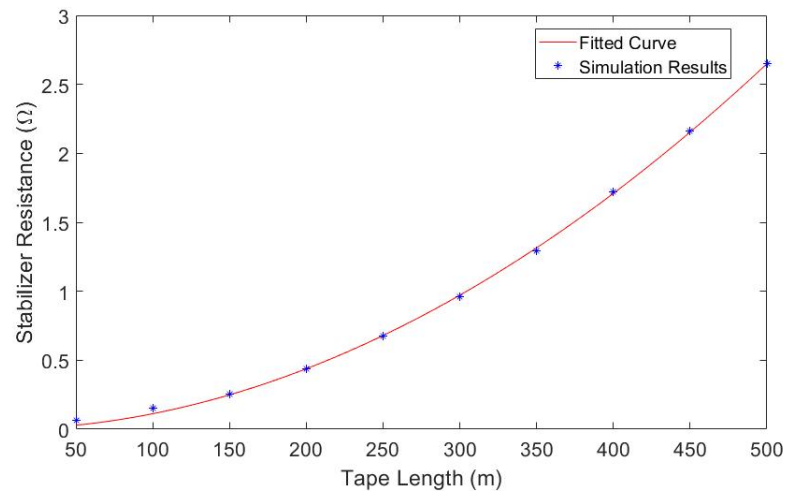
Figure 3.14: Variation in Stabiliser Resistance Requirement with Respect to Tape Length

Capacitance

From (3.23) it is clear that the size of the capacitor will have an impact on the whether the superconducting tape quenches and exhibits a critically damped response. This is because the energy in the circuit at rest is determined by the capacitor size and the voltage across its plates. The size of the capacitor also influences the natural frequency of the circuit, with a larger capacitance leading to a smaller natural frequency, increasing the time taken for voltage reversal to occur. These two factors cause an increase in capacitance from the baseline of 1 mF to decrease the amount of resistance required to provide critical damping. This can be seen on Figure 3.15 which shows that the required Stabiliser resistance reduces as capacitance increases for the range simulated. The range of capacitance values is not meant to be indicative of a typical TeDP system. These results can be fitted to the relationship shown in (3.25) which has an R-square value of 0.9963 and an SSE value of $3e^{-4}$.

$$R_{Q_c} = 0.0001461C^{-0.9431} \tag{3.25}$$

Figure 3.16 shows the variation in peak discharge current with capacitance at the critically damped Stabiliser resistance.

Voltage

Another significant difference between conventional and superconducting RLC circuits is that the magnitude of the voltage affects damping. This is clear from the condition set in (3.32). Taking the baseline case, that is critically damped, and varying the voltage, Figure 3.17 shows that increasing voltage decreases the required stabilising resistance up to a certain limit. This is because the energy on the capacitor is increasing and therefore larger heat capacities (higher CSA Stabilisers) can be used while still ensuring T_C is reached during the discharge. Figure 3.18 shows that discharge current increases in line with voltage at critically damped Stabiliser resistances.

This reaches a limit, which can be seen on Figure 3.17, beyond which greater in-
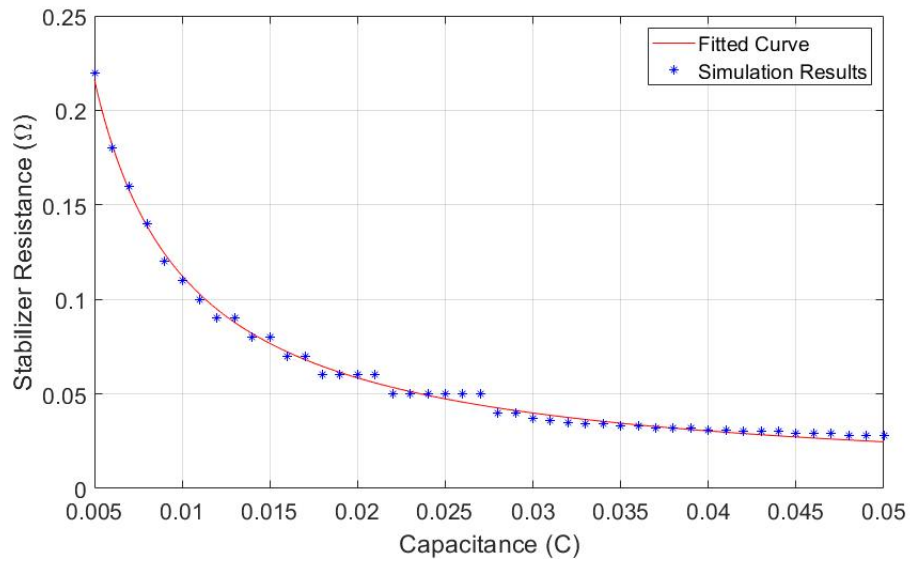
Figure 3.15: Variation in Stabiliser Resistance Requirement with Respect to Capacitance
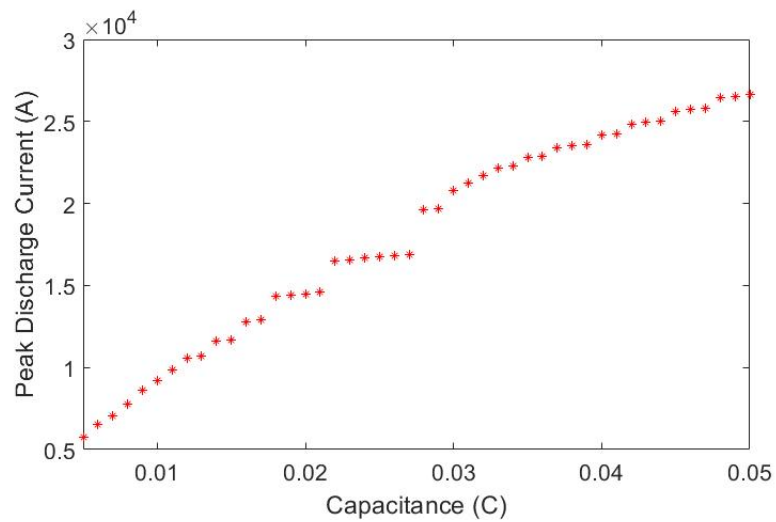
Figure 3.16: Variation in Peak Discharge Current with Respect to Capacitance
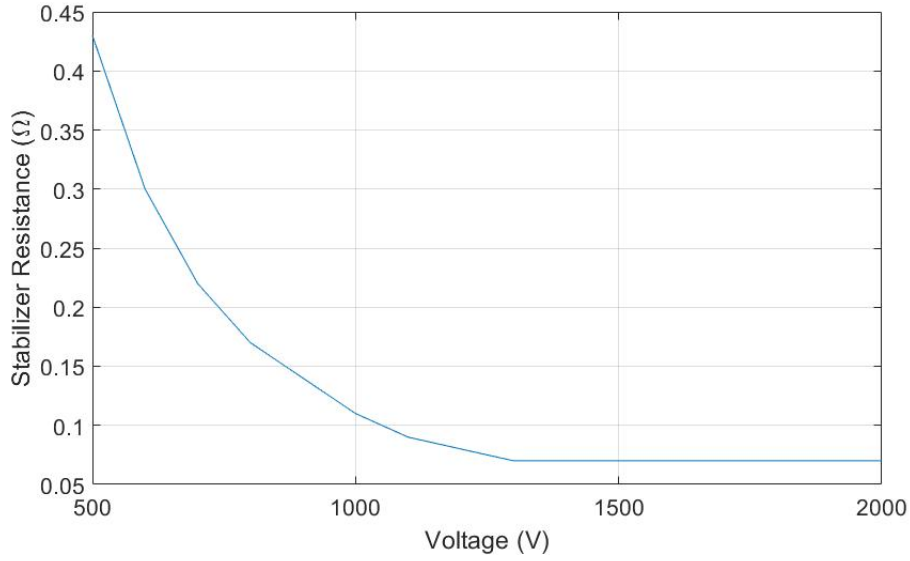
Figure 3.17: Variation in Stabiliser Resistance Requirement with Respect to Voltage Level

creases in voltage do not lead to smaller Stabiliser resistances. This is because any further reduction in the Stabiliser resistance would reduce the quenched resistance of the circuit below the conventional limit for a critically damped response (3.4) and violating (3.23). In addition, the temperature of the tape at the end of the simulation starts to rise significantly as shown on Figure 3.19. This is because circuit energy increases while cross sectional area, and therefore heat capacity, stays the same. This is the hard limit for Stabiliser resistance with a critically damped response.

Line Inductance

Figure 3.20 shows that line inductance is found to have a linear relationship with the required Stabiliser resistance for a critically damped system that is in agreement with the $R/2L$ relationship of Equation 3.4. The peak current discharge decreases non-linearly as circuit inductance increases at critically damped Stabiliser resistance as shown by Figure 3.21. This is due to the greater amount of impedance, reactive and resistive, in the circuit.
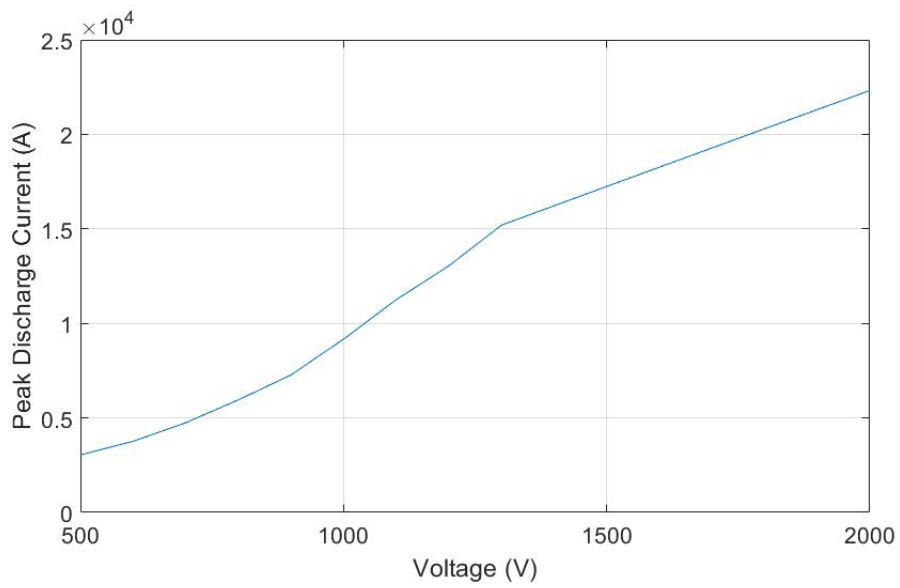
Figure 3.18: Variation in Peak Discharge Current with Respect to Voltage Level
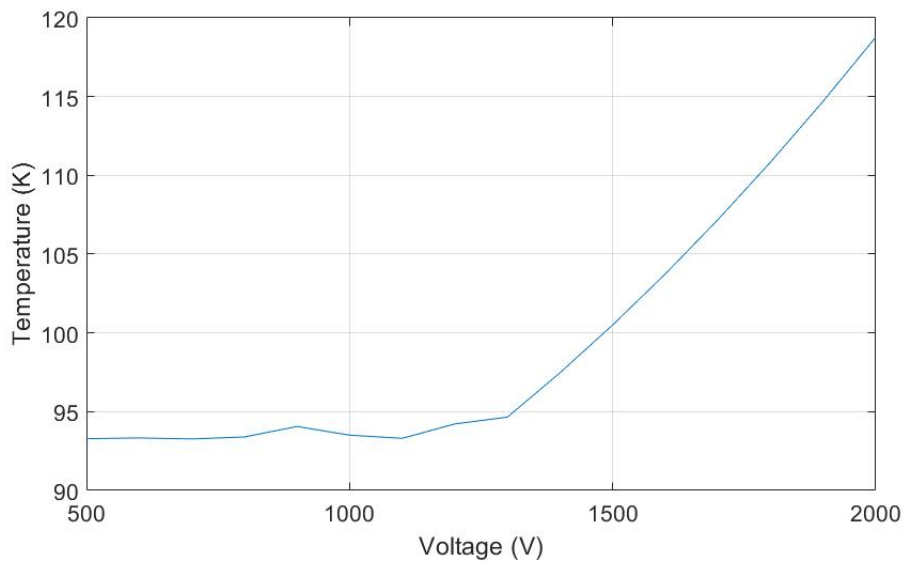
Figure 3.19: Variation in Peak Temperature with Respect to Voltage Level
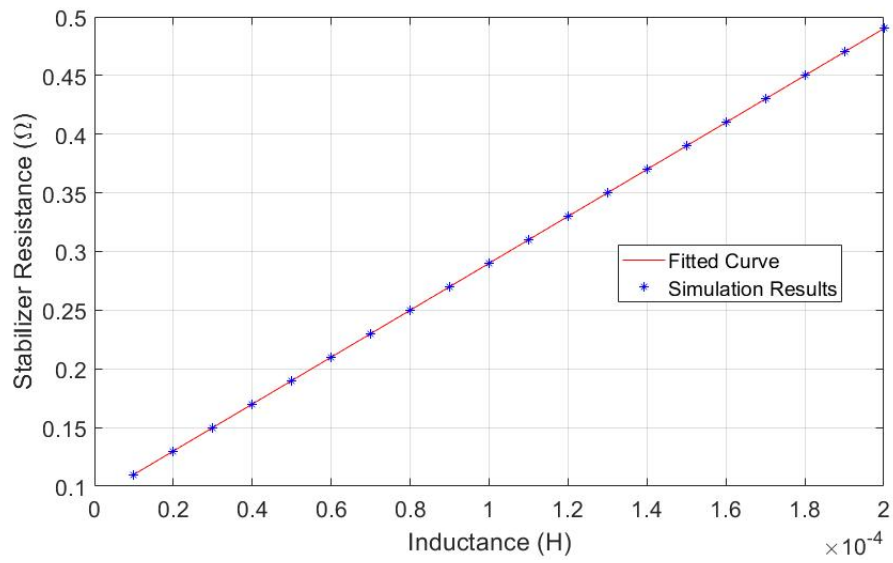
Figure 3.20: Variation in Stabiliser Resistance Requirement with Respect to Inductance
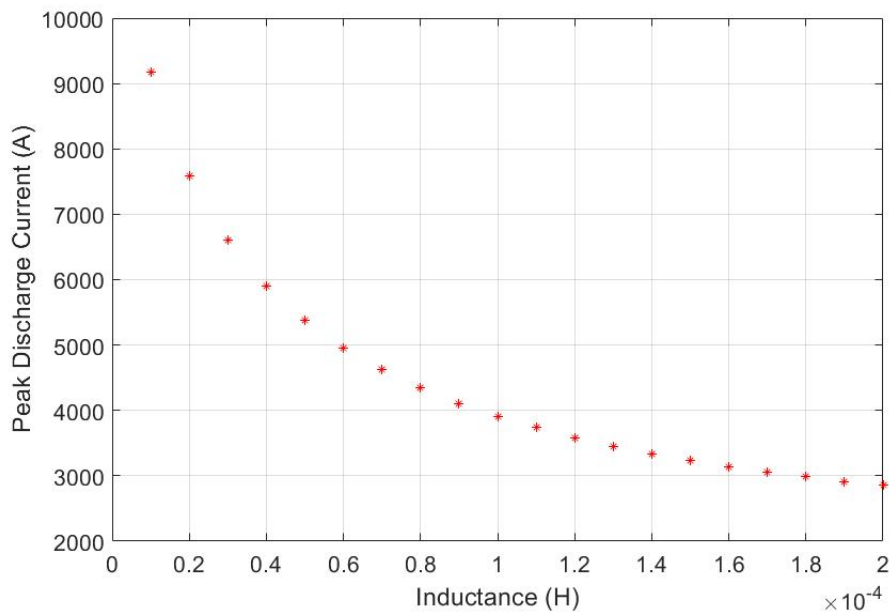
Figure 3.21: Variation in Peak Discharge Current with Respect to Inductance
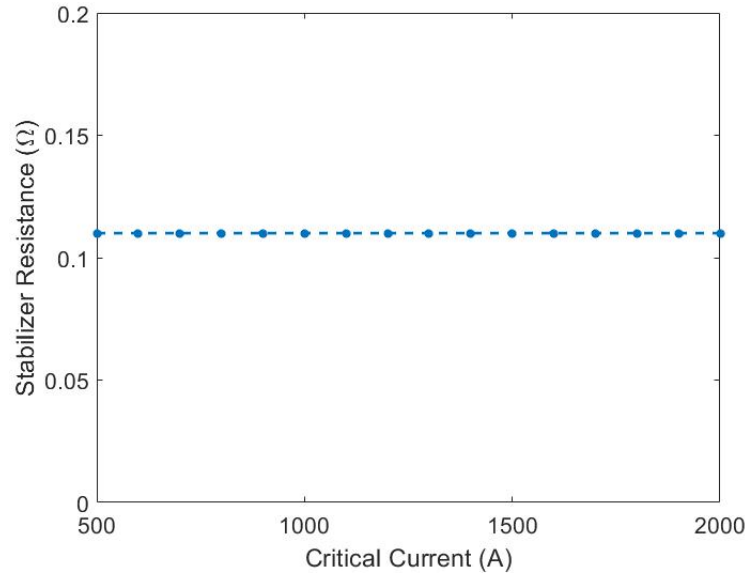
Figure 3.22: Stabiliser Resistance Stays Constant with Respect to Critical Current

Critical Current

Critical Current is varied from the base case and found to have no impact on the size of Stabiliser required to provide a critically damped response as shown on Figure 3.22. This is because a reduction in the critical current creates an effective increase in resistance but has a negligible impact on the heat capacity of the tape due to the very small CSA of the superconducting material.

It does however have an impact on size of the peak fault current, as can be seen from Figure 3.23. This relationship appears approximately linear over the range considered which is likely due to the fact that when the peak fault current occurs almost all of the current is flowing in the resistive stabiliser.

Operating Temperature

It is important to note that an implication of (3.23) is that a superconducting system could exhibit under-damped and over-damped responses to the same electrical conditions, depending on the component's operating temperature, T_0. To illustrate this, Figure 3.24 compares the current response of a superconducting tape with initial oper-
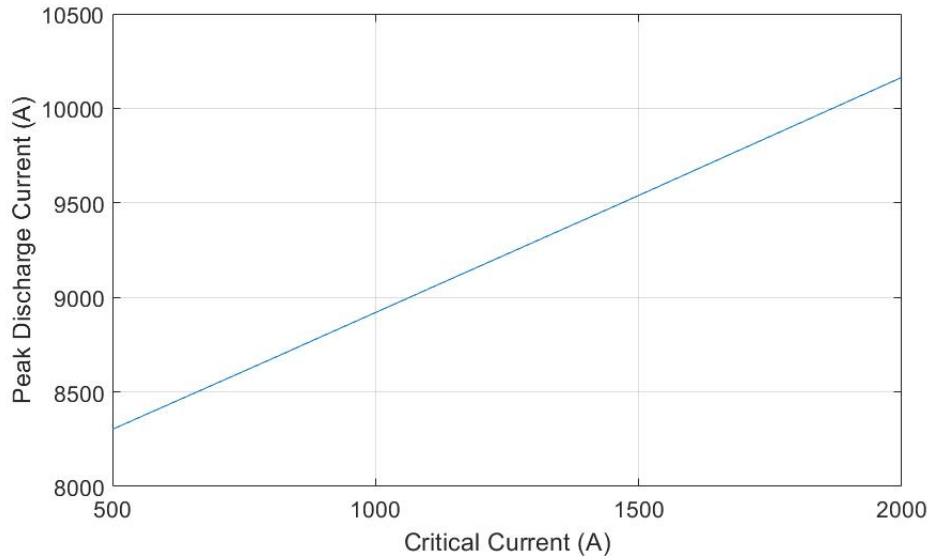
Figure 3.23: Variation in Peak Discharge Current with Respect to I_C

ating temperatures of $65K$ and $77K$ to identical circuit parameters and with the same Stabiliser resistance.

It can be seen on Figure 3.24 that while the the simulation with initial temperature $77K$ is critically damped, the simulation with initial temperature of $65K$ is very underdamped. Figure 3.25 shows the temperature profile for these simulations, illustrating that there was not enough energy stored on the capacitor to quench the simulation with initial temperature $65K$.

3.4 Experimental Discharge of Capacitors Through Superconducting Tapes

Experiments were conducted as a part of this work using a capacitive discharge rig in which the capacitor was discharged into a variety of different tapes and a cable arrangement. This was done to capture the response of YBCO superconducting tape to high rate of change current pulses as well as to validate simulation models. For this experiment two different types of tape was used: one with a high resistance parallel path made of very thin silver; one with a low impedance copper Stabiliser. A superconducting
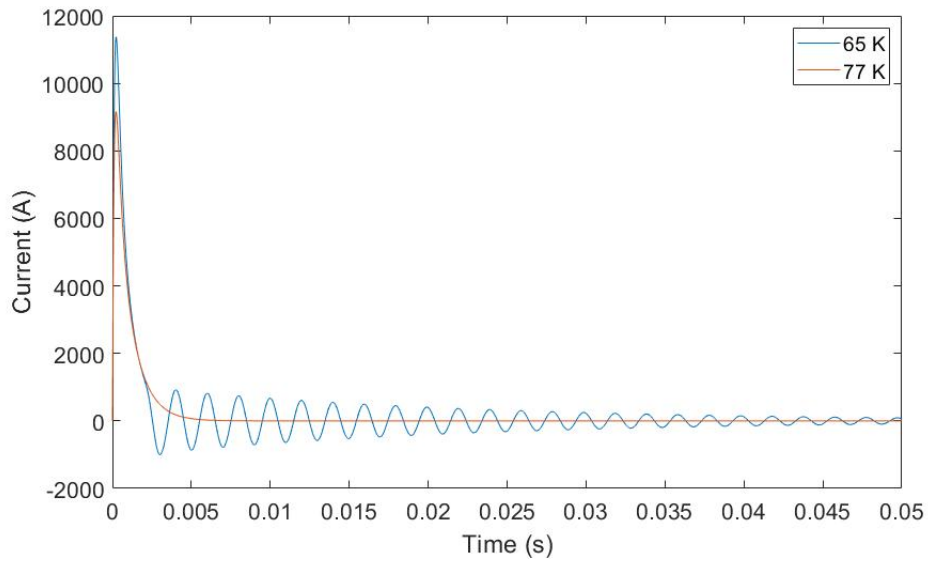
Figure 3.24: Current Profile for Capacitor Discharge in $65K$ and $77K$ RLC Circuit
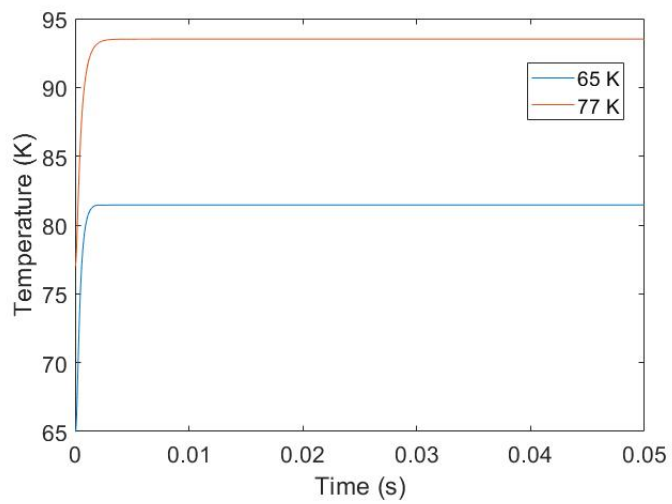
Figure 3.25: Final Temperature Reached After Capacitor Discharge in $65K$ and $77K$ RLC Circuit

cable was also used as part of the discharge experiments. These allowed investigation of over-damped and under-damped superconducting fault responses to the capacitor discharge. In addition, a parallel tape discharge experiment was conducted in order to investigate the impacts of current sharing between tapes during DC-fault events.

3.4.1   Experimental Setup

The aim of the experiment was to capture the response of a capacitive unit discharging through superconducting tapes. To achieve this, the experiment proceeded in two phases. The first phase of the experiment was to charge of a $47mF$, $100V$ rated capacitor using a controlled voltage source. This was disconnected from the circuit using a mechanical breaker following the charging phase completion.

The second phase of the experiment was the discharge of the capacitor. This was realised through the operation of three MOSFETs [118], connected in parallel to ensure that the rated current of the individual MOSFETs was never exceeded ($400A$). These switches were controlled via LabVIEW. An inductor was embedded within the discharge circuit to ensure a smooth discharge curve. The discharge circuit was connected to the superconducting tapes through $100A$ rated copper cables. All superconducting components in this experiment used YBCO as the active material. The superconducting components were submerged in a bath of liquid nitrogen to achieve an operating temperature of $77K$. Figure 3.26 shows the circuit used for the experiments. To provide a baseline for comparison, Figure 3.27 shows the results of the capacitor discharge through a copper cable rated for $100A$ continuous current at a variety of discharge voltages that will be used for the superconducting tape experiments.

3.4.2   Experimental Results

100 A Copper-Stabilized Tape Discharge

A controlled discharge of the capacitor was carried out through a $100A$ Superpower Inc. YBCO tape at a range of pre-fault voltage levels from $5V$ to $80V$. The superconducting tape was $4mm$ wide, $10cm$ long with a $100\mu m$ copper Stabiliser. Figure 3.28 shows the discharge current for each of these tests while Figure 3.29 shows the voltage drop
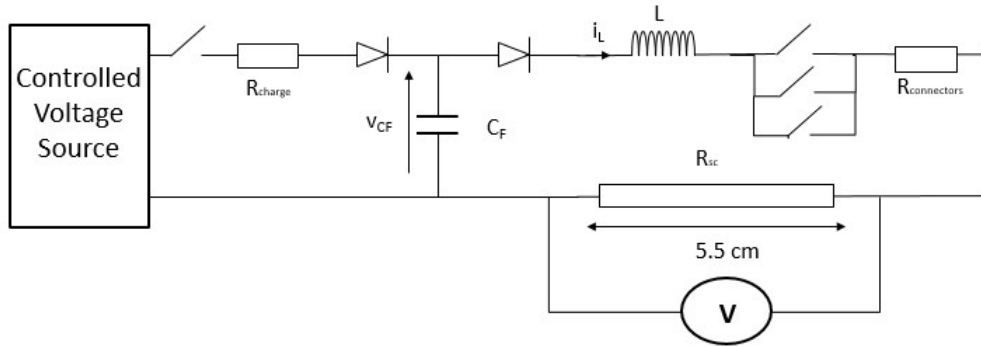
Figure 3.26: Circuit for Experiment
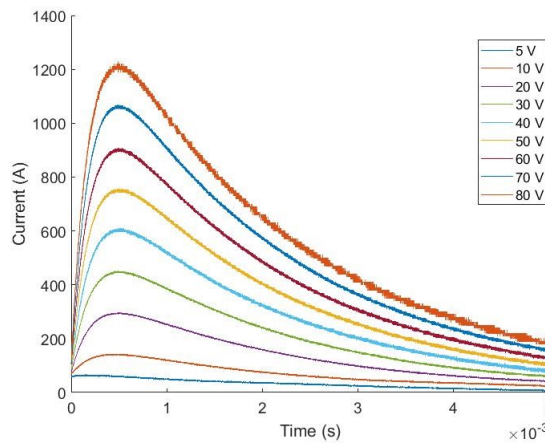
Figure 3.27: Discharge of capacitor through 100 A Copper Cables
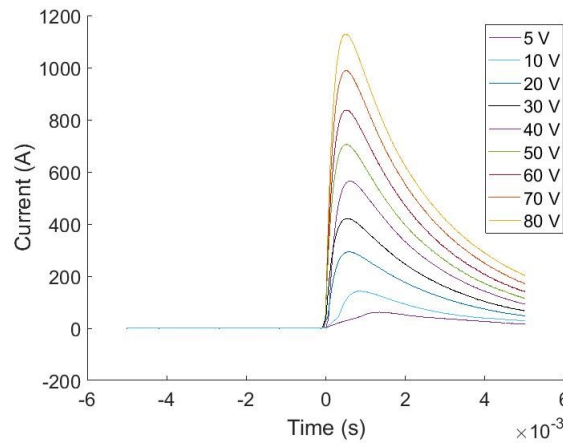
Figure 3.28: Stabilized Tapes Current Profile
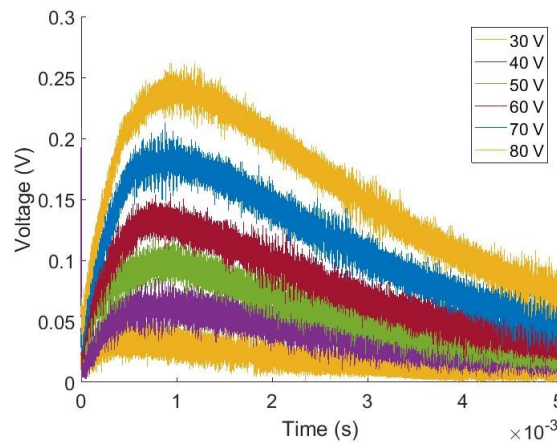
Figure 3.29: Stabilized Tapes and Voltage Developed

produced across the superconducting tapes.

It can be seen by comparing the current profile between Figures 3.28 and 3.27 that a slight reduction in the peak current occurs due to the electric field generated across the tapes. From Figure 3.29 it can be seen that above a $30V$ charging voltage level, that the superconducting tape starts to produce a noticeable voltage signal between the measurement taps, which are placed across $5.5cm$ of the tape length. This indicated that quench had taken place.

The critical current of the superconducting tape was measured before and after the discharge experiment and the results indicated that no degradation of I_c had taken
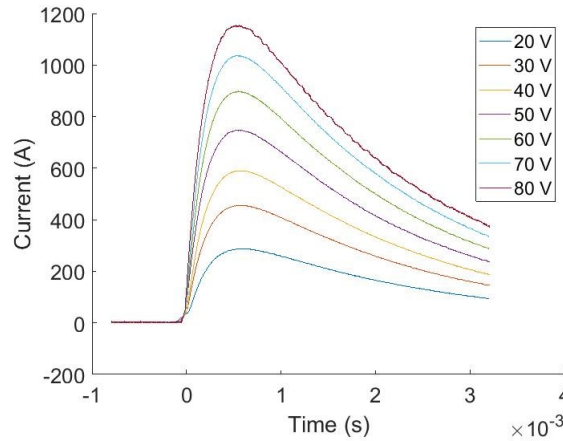
Figure 3.30: Current Profile of 420 A Cable Discharge

place. This is because the energy dissipated in the superconductor during the experiment resulted in a temperature rise which was not high enough to cause degradation to take place, normally estimated as $400K$ [95]. This demonstrates that these tapes are capable of withstanding short periods of transient over-current many multiples of the critical current. However, they will have a negligible effect on reducing fault current experienced by the system because of the low impedance path offered by the copper Stabiliser, resulting in a very under-damped response to fault current discharge.

420 A Cable Discharge

The $420A$ superconducting cable was constructed of a $20mm^2$ copper former with 4 copper stabilized superconducting tapes wound around this core. This is within the correct order of magnitude of current levels that feeder cables are expected to provide within a 1-5kV TeDP system. The cable measured approximately $30cm$ in length. The cable provided negligible impedance to the discharge current as evidenced by the current profile shown on Figure 3.30.

The voltage profile is almost indiscernible from background noise, and as such is omitted. This is due to the copper former providing a very low impedance path for the excess fault current to traverse in the case of currents exceeding I_c.

By inspection, neither the cable nor the stabilized tape are seen to have a significant
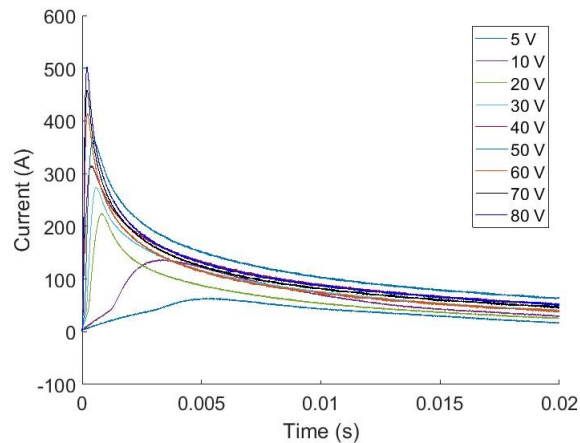
Figure 3.31: Non-stabilized Superconducting Tapes Discharge Current Profile

impact on the fault current profile when compared to the discharge through the copper cable. Hence, without including additional damping, fault currents would be extremely high due to the initial discharge of DC link capacitors. A consequence of this would be that other components in the system, such as the diodes in the power electronics converters, would have to dissipate large amounts of fault energy.

Large currents flowing in the power electronic diodes can result in the damage of components critical to the safe flight of an aircraft. The fast discharge of the capacitor in this very low impedance scenario could cause significant voltage depreciation throughout the system as DC-link capacitors connected across healthy branches also begin to discharge into the fault. This would impact on voltage stability. To counter this, extremely fast acting ($< 1ms$) protection systems may be required. It can be seen however that the critical current of the superconducting cable and tape does not degrade due to the high fault current, despite it being significantly above the critical threshold, indicating that these components are tolerant of large over-currents due to the parallel paths provided by the copper materials used in each.

50 A Superconducting Tape Without Stabiliser Discharge

A controlled discharge was performed through a $50A$ tape without a copper Stabiliser, which was replaced by a thin layer ($1\mu m$) of silver laminated across the superconducting
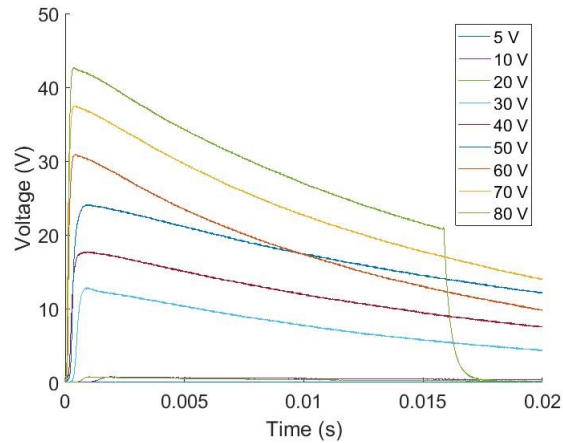
Figure 3.32: Non-stabilized superconducting tapes Voltage drop

material of the tape. Figure 3.31 shows the current profile resulting from the capacitor discharge, and Figure 3.32 shows the voltage profile. In contrast to the previous results, it is shown on Figure 3.31 that there is a reduction in the peak current when compared to the original discharge through standard copper connectors. For the $80V$ discharge test this reduction was approximately $700A$. The voltage drop across the superconductor is also orders of magnitude larger in comparison to the discharge through the copper stabilized tape.

The voltage signal for the $80V$ test (Figure 3.32) rapidly drops to zero after $0.0015s$. This is because the temperature reached by the superconducting material exceeded the melting point of the solder on the connections to the voltage measurement equipment, $461K$. Unlike the results presented for the copper stabilised cable, significant critical current degradation was observed following the $70V$ discharge test for the tape without a Stabiliser. The $80V$ discharge completely destroyed the superconducting properties of the YBCO material. Interestingly, no physical damage was apparent upon a visual inspection.

Scanning electron microscope (SEM) analysis showed scarring of the superconducting layer at the microscopic level which indicates a possible reason for the destruction of the superconducting properties. Figure 3.33 shows the critical current of the superconducting tape following successive tests.
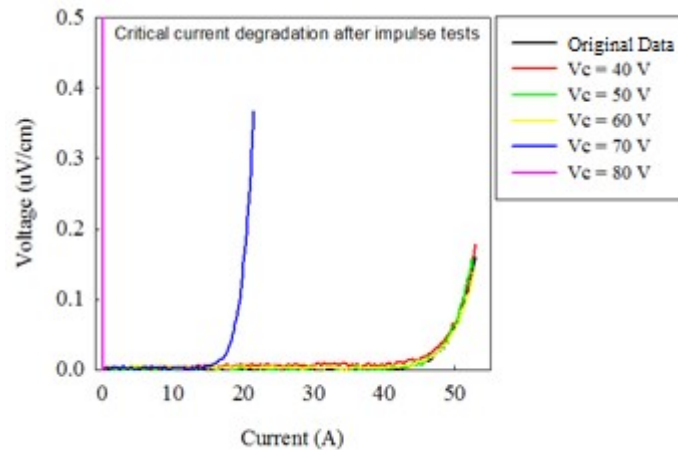
Figure 3.33: Critical Current Degradation of Unstabilized Tape

This series of tests showed that the peak discharge current of the filtering capacitor is significantly reduced by using tapes that are highly resistive post quench. This demonstrates the potential for using superconducting materials in the design of the distribution network which are highly resistive post quench, as a means to reduce the amount of fault current experienced by components on the network. This may allow for certain components to be derated, reducing the weight and volume penalties they incur. Further investigation into the benefits this would bring to the overall performance of the electrical power system is required. The discharge time constant is also significantly larger than the previous experiments that utilised copper to provide shunt paths, due to the higher post quench resistance. This may have benefits for post-fault voltage stability, due to the slower discharge of DC link filters, reducing the speed of fault propagation to healthy branches of the network. However, it must be noted that during this experiment the tape experienced significant thermal and electrical stress, eventually causing the complete breakdown of superconducting properties. In order to take advantage of this potential functionality, components would have to be designed to withstand the maximum current and temperature reached during the fault period. The temperature rise experienced will be directly related to the volume available for dissipating heat. As resistance is inversely proportional to the cable area, a trade-off between fault impedance and temperature rise is created.
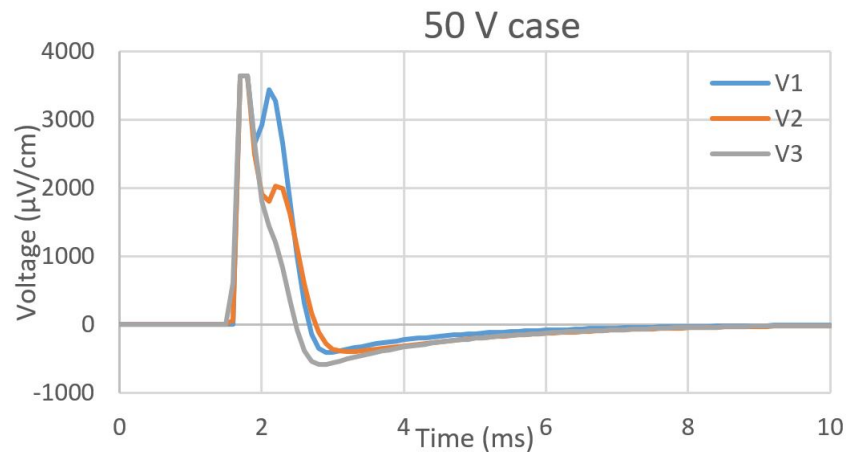
Figure 3.34: Voltage Drop Along Parallel Tapes at 50 V Discharge

Parallel Tape Arrangement

One of the assumptions made at the modelling stage is that the current sharing between multiple superconducting tapes is uniform, meaning each tape receives an equal share of the total current. This allows modelling such that multiple superconducting tapes can be treated as single lumped model, which is required for higher current levels. To this end, a discharge experiment through tapes in parallel was conducted.

The parallel tape discharge test utilised three SuNAM tapes. Each tape was $6mm$ wide, $10cm$ in length, possessing a copper Stabiliser with a $100\mu m$ thickness, and with a critical current of $175A$. Current distribution in each of the tapes was measured using individual hall effect sensors for each of the tapes. Above $50V$ discharge voltage, the quench voltage became noticeable across the tapes. Figure 3.34 shows the voltage profile for a $50V$ discharge test while Figure 3.35 shows the associated current distribution between the tapes.

The small voltage signal highlights the difficulty of detecting the quench voltage at current levels below $1.3 - 1.5I_c$. It is also noted that the current is not shared equally between the tapes. As the voltage of the discharge is increased the uniformity of current sharing increases and the current becomes more evenly distributed between the three tapes. This is because to the inductive voltage produced by the tapes, created by the large rate of change of current outweighs the impedance offered by the quenching
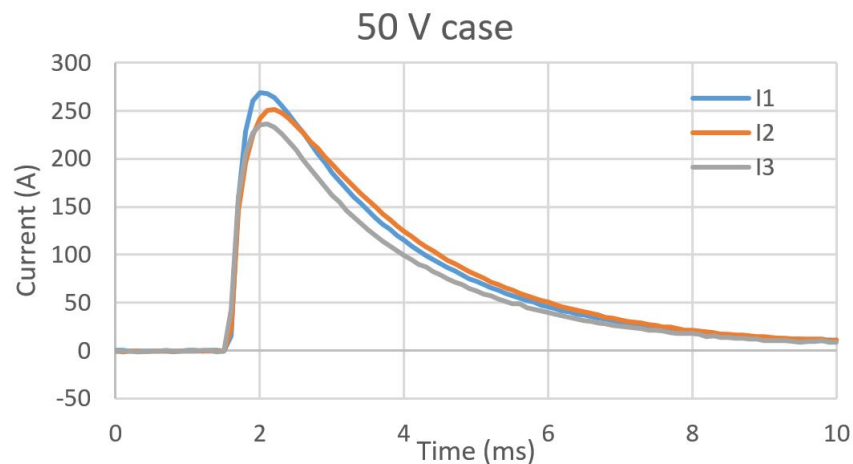
Figure 3.35: Current Distribution Between Parallel Tapes at 50V Discharge

process and any contact resistances present in the tapes connections. This can make it difficult to detect the quench taking place as the detection mechanism will have to compensate for the inductive voltage produced by large transients. This could be even more prominent in cables with tapes wound helically as the inductance would be significantly larger than in the small tapes considered here. Figures 3.35 and 3.36 show the current distribution and voltage drop across the tapes during the $80V$ discharge test.

Current sharing under large transient conditions (Figure 3.37) can be compared to Figure 3.38 where the current is ramped up in a slowly controlled fashion at a rate of $10A$ per second. In the load ramp case it can be seen that the current sharing between the tapes is dominated by contact impedance, causing significant differences between the currents carried by each of the three tapes, reaching a peak deviation of 30%. This shows that under significant transients, inductance is the dominant factor in current distribution between parallel superconducting components in a DC system while contact impedance is more significant in steady state conditions.

3.5   Chapter Summary

This chapter described the fault process for a conventional DC link, focusing in on the initial capacitor discharge, a potentially damaging aspect of VSC interfaced systems
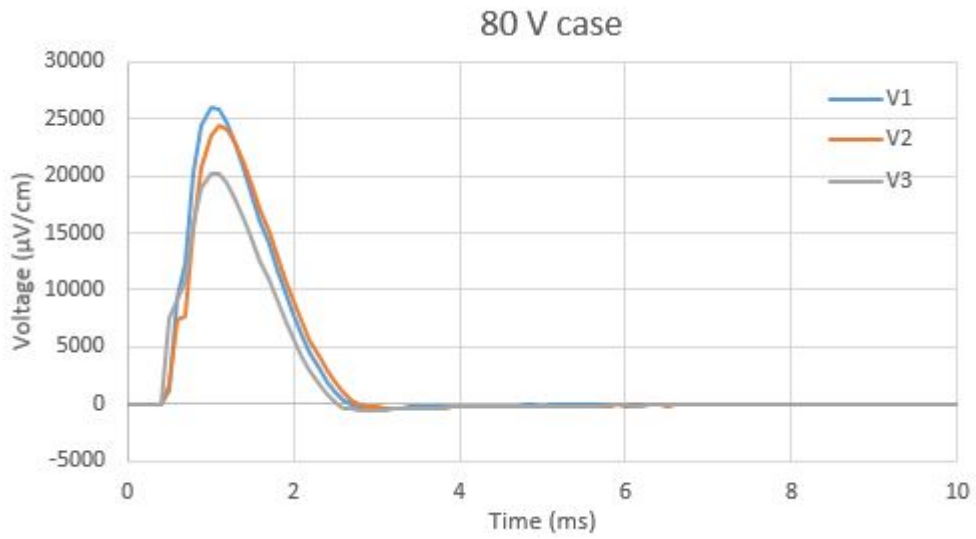
Figure 3.36: Voltage Drop Along Parallel Tapes at 80 V Discharge
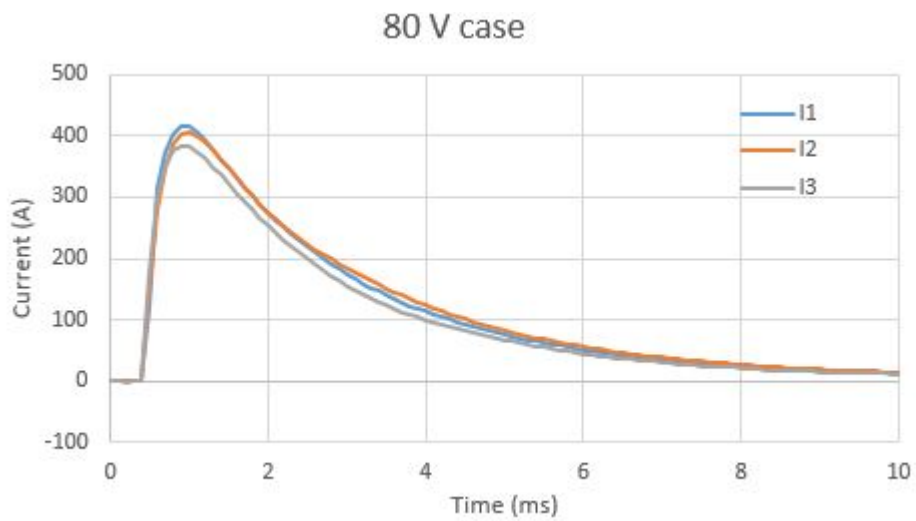
Figure 3.37: Current Distribution Between Parallel Tapes at 80V Discharge
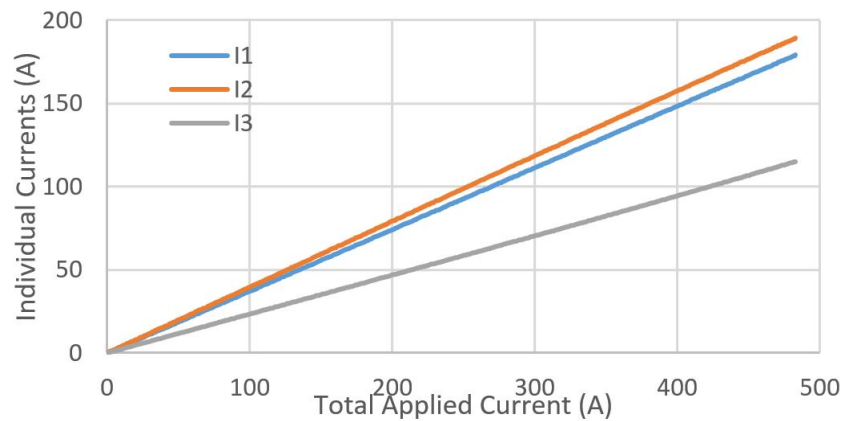
Figure 3.38: Current Distribution Between Parallel Tapes During Current Ramp Test

under fault conditions. Creating models of superconducting tapes from literature, this chapter analysed the impact of the initial discharge of the DC-link filtering capacitor through a fault path that contained a superconducting component. This contributed an analysis of the thermal-electrical circuit requirements for under, over, and critically damped RLC responses in superconducting networks under faulted conditions.

Novel experimental results showed that superconducting tapes can withstand the large discharge currents (Figure 3.27) resulting from a rail to rail fault in an RLC circuit without undergoing permanent damage. However due to the low impedance of these tapes, as a result of the highly conductive Stabiliser, they produce little damping to the fault current which can be potentially damaging for other components in the fault path such as the switching diodes. Conversely tapes with a high impedance shunt path were shown to provide an overdamped response but heat up to the point where critical current is degraded. Thus there is a need for appropriate material selection and sizing of stabilising layers to prevent damage to superconducting materials resulting from high current capacitor discharge.

Future work could consider the use of different materials in order to determine the impact of material constants on the superconducting RLC circuit response, providing a more complete circuit theory understanding. While this chapter has discussed the macro, circuit theory level of superconductors, Chapter 4 will go deeper into the component level of superconducting modelling.

Chapter 4

Finite-Difference Method Modelling of Superconducting Cables

4.1 Finite-Difference Method Superconducting Cable

The previous chapter focused on the development of a superconducting tape model within Simulink to understand the impact of tape and circuit design to the response of an RLC circuit containing a superconductor. This chapter focuses on the development of a Finite Difference Method (FDM) based model. Whereas the Simulink modelling of the previous Chapter allows the observation of the macro circuit impacts of superconducting tapes under fault, FDM allows us to zoom in on the impact that electrical faults and over-currents have on superconducting tapes at the component level. This allows us to better analyse the impact of an electrical fault on superconducting cables and the implications this has for superconducting cable design and electrical protection systems on aircraft. To do this, this work will compare the thermal response of FCL and FCT cable designs to over-current conditions, assessing the impact of electrical faults and hotspots and what this means for protection requirements and cable design choice.

As described in Chapter 2.3.3 there are two design approaches that have system

level implications for protection and fault response: FCT, and FCL. The first of these cable designs uses high impedance shunt paths in the cable design to dissipate energy and reduce peak fault currents. The advantage of this approach is that it can reduce the sizing requirements of other protection equipment in the system such as circuit breakers. However, the superconducting cable itself may undergo significant heating and there may be greater potential for hotspots occurring due to the lower thermal conductivity of the materials used. Hotspots are described in Chapter 2.4.2.

In contrast to FCL cables, FCT superconducting cables are constructed from materials with high electrical and thermal conductivity in parallel with the superconducting material. This serves to reduce the amount of energy absorbed by the cable during an electrical fault. As a result there is less damping in the circuit (Chapter 3). This leads to higher fault currents but also protecting the superconducting cable by reducing the amount of energy absorbed. The high thermal conductivity also helps energy dissipate more evenly throughout the material which can prevent destructive hotspots. This means that while FCL cables are useful for applications where reducing fault current is a primary goal, FCT cables may be more suitable for applications in which minimizing the amount of network isolated is critically important, which could be the case in a compact network with fewer redundant paths.

4.1.1 Modelling Method Implementation

An electrical-thermal model of the superconducting cable, originally developed by [117] has been adapted for both FCL and FCT cable designs to determine the impact that overcurrent has on the formation and severity of hotspots in these two design approaches. The thermal section of the model has been created by discretizing the superconducting cable in the longitudinal direction. The backward time, centered space method (BTCS) is used to model heat conduction throughout the component at discretized intervals, or nodes.

This is expressed in (4.1), where k is thermal conductivity (W/K.m), Cp (J/kg) is specific heat, ρ (kg/m^3) is the density of the material, T (K) is temperature, Q (J) is the heat flux generated within the body and t (s) is time. To simplify the model

87

it is assumed that in over-current conditions the cooling power is significantly smaller than the heating due to flux flow and resistive losses through current sharing with the stabilising layer.

$$\frac{\partial T}{\partial t} = \frac{k}{C_p \rho} \frac{d^2 T}{dx^2} + \frac{Q}{C_p \rho} \tag{4.1}$$

Applying the central difference implicit method to (4.1) produces the (4.2), where T_i^t is the temperature of node i at time t and Q_i^t is the heat flux generated at node i at time t. This discretizes the component into smaller nodes that represent points along the cable's length:

$$\frac{T_i^{t+1} - T_i^t}{\Delta t} = \frac{k T_{i-1}^{t+1} - 2 T_i^{t+1} + T_{i+1}^{t+1}}{C_p \rho \Delta x^2} + \frac{Q_i^t}{C_p \rho} \tag{4.2}$$

which can be rearranged into the following form:

$$1 + 2 F T_i^{t+1} - F T_{i-1}^{t+1} - F T_{i+1}^{t+1} = T_i^t + \frac{\Delta t Q_i^t}{C_p \rho} \tag{4.3}$$

where F is defined as:

$$F = \frac{\Delta t k}{C_p \Delta x^2 \rho} \tag{4.4}$$

(4.3) can be implemented as a sparse matrix and solved at each time-step using MATLAB's backslash operator [119]. Heat generated at each node calculated using $I^2 R$ losses, accounting for current and resistance of the superconducting conduction layer and the conventional stabilising and former materials that are inherent in the overall cable design.

Each node in this one dimensional model characterizes a part volume of the superconducting tape layer. The specific heat and density of the mass encompassed by a particular node is determined based on the ratio of the materials used in the tapes. For this case we consider the material used in the Stabiliser and substrate. Each tape is chosen to be 4 mm x 0.1 mm with a mean critical current of 100 A.

Variations in critical current will be extremely challenging to eliminate as they

arise due to manufacturing defects, poor handling, and operating conditions. Here it is implemented based on a normal Gaussian distribution shown in (4.5) where μ is the mean critical current (A), σ is the standard deviation, and I_p is the list of possible critical currents (A). This is an approach previously seen in [120].

$$I_c(i) = f(I_p | \mu, \sigma) = \frac{1}{\sigma 2\pi} e^{\frac{-(I_p - \mu)^2}{2\sigma^2}} \tag{4.5}$$

This variation in I_C (A) throughout the component is the primary cause of the formation of hotspots, as different parts of the cable are quenched, at different operating currents. This distribution is discretized and then sampled using a roulette wheel selection method to populate the cable with a variety of critical current levels depending on the size of the standard deviation, the level of variability. Figure 4.1 shows an example result of this selection method to populate the critical current of different sections of cable and compares the result to the normal distribution. The number of tapes required is determined by the maximum load current of the system divided by the mean current of the tapes. Additionally, it is assumed that the cable will incorporate a stability margin as in practice this is likely going to be required to prevent areas of localized quench. This is selected conservatively here such that the maximum load current is 60 percent of the critical current.

The HTS tapes are modelled a mesh electrical network where each node is represented by the superconducting material, $R_{SC}(\Omega)$, (YBCO) in parallel with the stabilising layer, $R_S TAB(\Omega)$, that is composed of a conventional material, as shown in Figure 4.2. Contact resistance between the superconducting layer and the Stabiliser is ignored. The impedance of the superconducting material at each node is calculated according to the $E - J$ characteristic described in (4.6), where E_0 is taken as 1 μ V/cm, n is the index of transition, $Jc(T, x)$ is the temperature dependent critical current density at a given node i, and J (t) is the current density within the superconducting layer at a particular time.

$$E(J, i) = E_0 [\frac{J(t)}{J_c(T, i)}]^n. \tag{4.6}$$
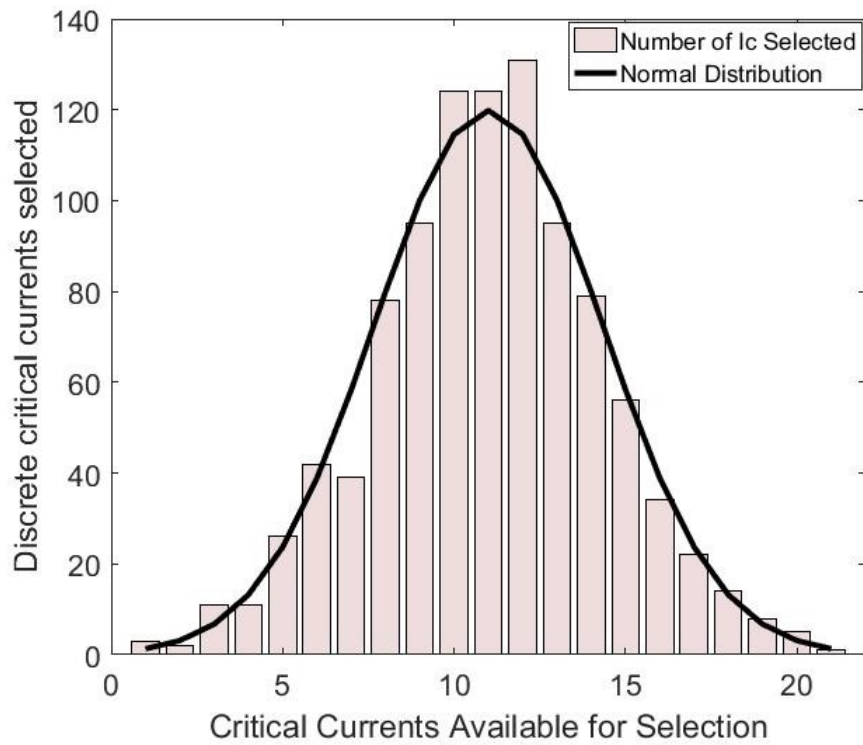
Figure 4.1: Discretization of critical current levels to be interleaved throughout the superconducting cable
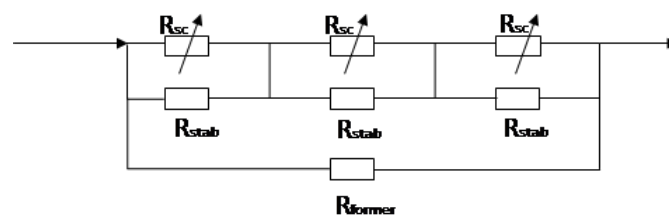
Figure 4.2: Example of electrical circuit discretization used in the model, in which the tapes are made of a mesh network of superconducting and conventional materials while being electrically paralleled with a former.

The resistance of the cable former,$R_{Former}(\Omega)$ is calculated using the cable dimensions and the temperature dependent resistivity of the conventional material used in the former. The former is modelled to be to be in parallel with the HTS tapes and this is also shown on Figure 4.2.

Current sharing between the cable former and the HTS tape, the superconducting material and the stabilising layer at each node is calculated using an iterative current method as described in Section 3.2.2 that has been adapted to include the cable former. This method provides good solutions to the current sharing problem but is a relatively slow method, due to the high number of calculations which must be performed [117]. Greater discretization will also increase how long the process takes. To reduce the simulation time for long lengths of cable it is assumed that cable critical currents, and the associated thermal profile, repeat throughout a length of cable.

The temperature dependence of the critical current is represented by (4.7), which is adapted from (3.9), where $T_c(i)$ (K) is the critical temperature of node i. T_r (K) is the reference temperature, in this case 77 K (the temperature of the liquid nitrogen) and $J_c r$ (A/mm$_2$) is the critical current density of node i.

$$J_c(T_i) = J_c r [\frac{T_c(i) - T(t, i)}{T_c(i) - T_r}]^k \tag{4.7}$$

Similarly The temperature dependence of the transition index, n, is calculated according to (4.8) where $n_r ef$ is the transition index at 77 K and ζ is the index coefficient, taken as 0.25 [121].

$$n(i) = \frac{n_r ef - 1}{2} [\frac{T_c - T(i)}{T_c - T_{LN2}}]^\zeta + 1 \tag{4.8}$$

4.1.2 Hotspot Simulation Parameters

To investigate the formation of hotspots and their impact on cable designs, FCL and FCT cable models are developed for cables rated at 10 MW. This power rating was chosen based on published TeDP architectures [28]. It is assumed that the total cable length is 100 m.

The superconductor material used for both the FCL and FCT cables was YBCO

with a presumed critical temperature of 93 K and initial transition index of 21.For this FCT cable, the former is sized to withstand a fault current 3.5 times larger than the full load current, and to withstand this current for approximately 1s without the former temperature rising by more than 5 K using copper as the former material. The stabilization layer of the superconducting tapes is also chosen to be 50 μm thick copper to provide a low resistance path for the current during quench. Conversely, in the FCL cable design, the former is assumed to be made of stainless steel to provide a high resistance when quench occurs. The cross sectional area is sized to provide an impedance that limits the fault current to 3.5 times full load current. This was calculated as 76.3 mm^2 for a 100 m cable. The stabilization layer of the FCL cable design also uses stainless steel.

The temperature is not allowed to exceed 150 K during the simulations for both cables. This is considered a safe hot spot limit for many low temperature superconducting components [122] Although degradation of critical current is unlikely to occur below 400 K in YBCO Superconductors [95]. Upon reaching this condition, the simulation for FCL cables is be stopped.

The simulations are carried out considering constant current levels exceeding the critical threshold of the cable by 10 % to 50 % in steps of 10%. The measure of variance inherent in the sample is varied by altering the standard deviation (SD) from the mean I_C from 0.06 to 0.01 in steps of 0.01, to incorporate varying quality of tapes with more or less homogeneity in critical current. The tapes themselves are discretized in 1 mm intervals with critical currents interleaved to each node. This was initially carried out for 1000 nodes to produce a component 1 m long. This model was then subsequently cloned 100 times under the assumption that the inhomogeneities are repetitive, to represent the response of a 100 m long cable. Figure 4.3 shows the variation in critical current throughout a 1 m section of cable with a SD of 0.06, with each node representing a 1mm length of the tape.

The initial voltage used for the simulation is 5 kV as this has been previously found to be an appropriate voltage for a TeDP electrical power system with a DC distribution network [29] The operating current and cable critical current are derived
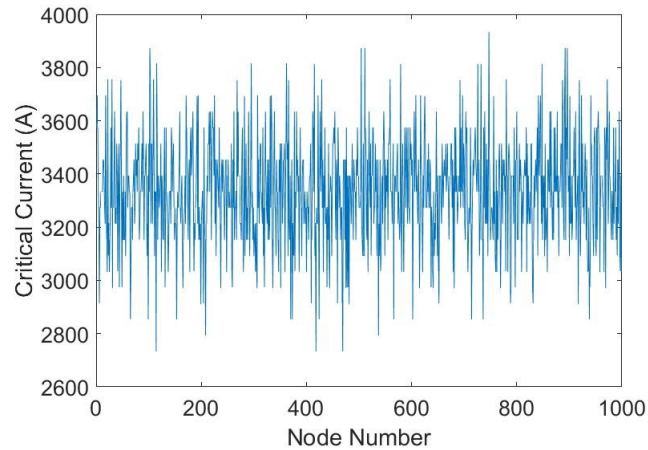
Figure 4.3: Critical current distribution for 5 kV cable used in simulations.

from this voltage level. Figures 4.4 and 4.5 show the case of SD of 0.06 with an over-current of 1.5 I_C that lasts 0.1s. The temperature profiles observed for each of the cable designs are shown in Figures 4.4 and 4.5.

From Figure 4.4 and 4.5 it can be seen that this level of over-current leads to a smooth temperature profile within the FCT cable superconducting layer that peaks close to 79.75 K, far below the critical temperature of 93 K. It can be seen that this temperature rise is concentrated around nodes 400-600 which, as shown on Figure 4.3, contain multiple nodes with low critical current selection. The smooth profile can be attributed to the high thermal conductivity of the copper Stabiliser present in the superconducting tapes. In addition, as a result of the low impedance of the copper former, there is less current flowing through the superconducting tapes, and is instead diverted into the former. This was in stark contrast to the FCL cable design which, due to the low thermal conductivity of the Stabiliser, caused the clear hotspots to form reach much higher temperatures. The large localized temperature rise and the resulting thermal gradient in the tape could potentially degrade or destroy the superconducting effect in these areas as seen in the earlier experiments in Chapter 3. To prevent this higher stability margins could be required through using greater amounts of superconducting material or necessitate higher quality material with a more uniform critical current to prevent hotspots. Both options are likely to lead to higher costs.

93
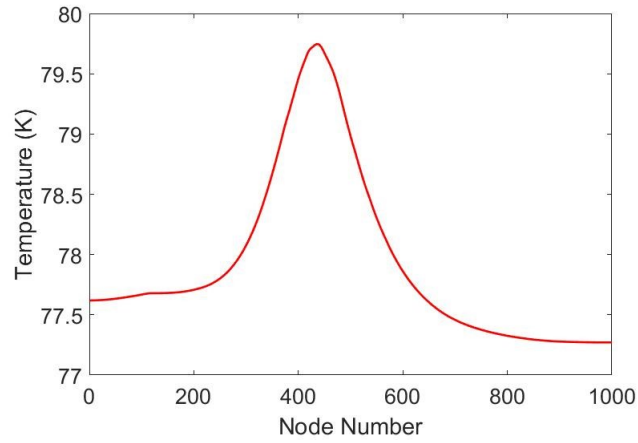
Figure 4.4: Temperature distribution of superconducting layer in FCT cable following over-current simulation.
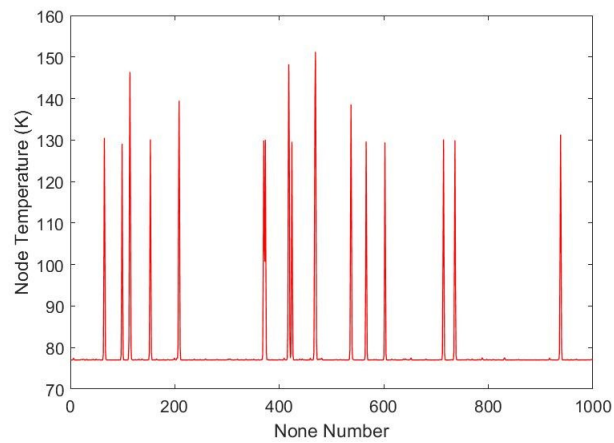
Figure 4.5: Temperature distribution of the superconducting layer in FCL cable following over-current simulation
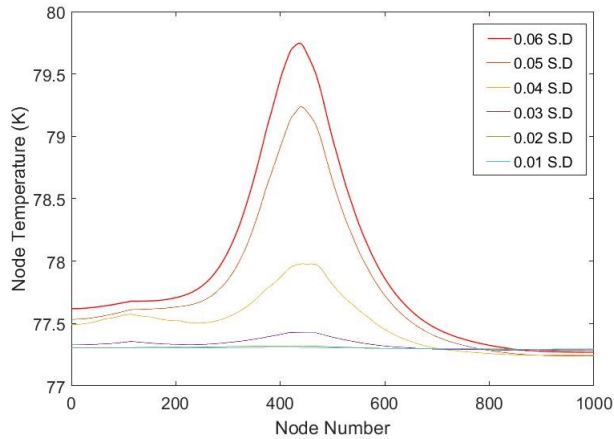
Figure 4.6: Temperature distribution in FCT cable at a variety of cable inhomogeneity levels.

4.2 FCT and FCL Cable Response

FCT Cable Response

The impact of varying the SD of critical current, superconductor quality, and the over-current level on the FCT cable temperature profile is shown in Figures 4.6 and 4.7 respectively. It can be seen from Figure 4.6 that reducing the standard deviation, while keeping the over-current magnitude constant, has a positive effect on reducing the maximum hotspot temperature alongside smoothing the component's temperature profile. Figure 4.7 shows that by reducing the magnitude of the over-current, the peak temperature is also reduced, although the shape of the temperature profile is still non-uniform. The largest temperature rise is generally between nodes 300 to 600, while nodes 0 to 300 experience a moderate increase and nodes 600 to 1000 undergoing only minor temperature rise. This is because there is less current flowing in the resistive part of the superconducting tapes in these areas, leading to reduced Ohmic losses in these areas.

Although the temperature rise appears insignificant for the FCT design, it has a significant impact on the critical current profile of the cable due to the temperature dependency of the critical current. The critical current profile following the over-current for the worst case scenario is shown in Figure 4.8. At its most severe point, the critical
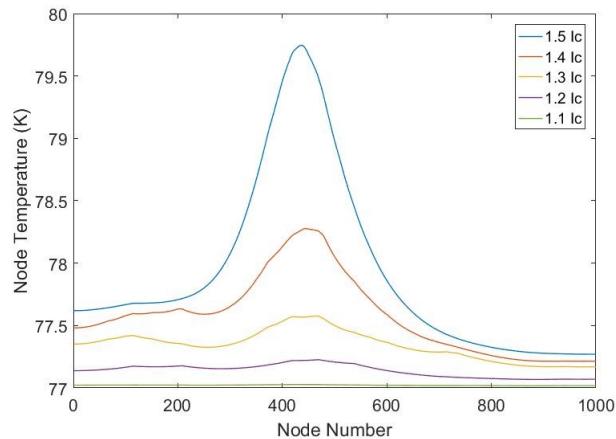
Figure 4.7: Temperature distribution in FCT cable at a variety of over-current levels.

current is reduced to 75.4 % of its initial value. Considering that the assumed stability margin is set such that the full load current is 60 % of the cable's critical current at 77 K, the full load current is now much closer to the critical current limit following the fault. This will lead to greater heat losses, increasing the cooling system requirements. In addition, the cable will now be more susceptible to future faults until it returns to its normal operating temperature due to operating close to the critical current. This will have an impact on protection operating speed requirements. Indeed, these may need to be pre-emptively set to account for the potential variation in, or dynamically adjusted in response to, changing thermal and electrical conditions. To avoid this larger margins between operating and critical current could be used so that transient over currents that exceed the critical current by smaller amounts. This would reduce the overall temperature rise, as shown in Figure 4.7, by reducing the amount current that is passing through the resistive Stabiliser during these periods.

FCL Cable Response

Figures 4.9 and 4.10 show the temperature profile of the FCL cable with a standard deviation of 0.01 and 0.03 respectively. Note that overlaid plots of temperature are not utilised here (unlike the results for the FCT cable, Figures 4.6-4.8) as this would result in a loss of visual clarity. Separate traces for individual cases are instead presented.
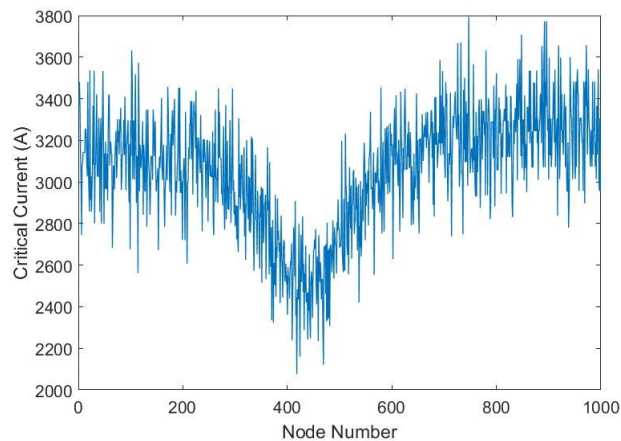
Figure 4.8: Cable critical current distribution following over-current simulation.

It can be observed that hotspots still occur in the cable with the lower modelled SD value, but that there are fewer of them in comparison to the cable with the higher SD value, Figure 4.5. While the reduced number of hotspots is an improvement, they may be more difficult to detect. This is due to a smaller resistive zone dissipating heat, resulting in a lower voltage drop, which is more difficult to detect and locate.

Impact of Voltage Level on Cable Performance

The electrical power system architecture for TeDP is an area of ongoing research and there is a need to explore system design trade around selection of the distribution voltage level. For instance, lower voltage (1 kV) systems could potentially better exploit the power density of superconducting cables while higher voltage (5-10 kV) systems could serve to reduce switching losses within power converters.

To investigate the impact varying the system operating voltage has on both cable types with respect to hotspot severity, this voltage is varied from 1 kV to 10 kV, and the maximum cable temperature after the over-current event is recorded. The discrete voltages used in these simulations were 1 kV, 2.5 kV, 5 kV, 7.5 kV and 10 kV. In addition, the current peak (as a multiple of the critical current I_C) and standard deviation of critical current along the cable were varied from 1 to 1.5 and 0.01 to 0.06 respectively. For each voltage level, the cable former is resized in accordance with the
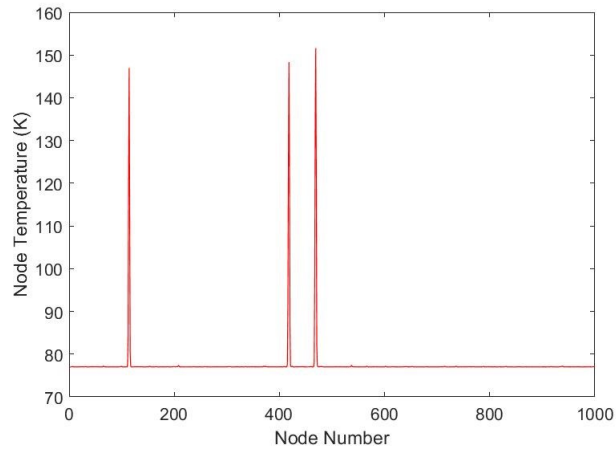
Figure 4.9: Temperature profile following 1.5 I_C over-current in FCL cable with 0.01 standard deviation of I_C
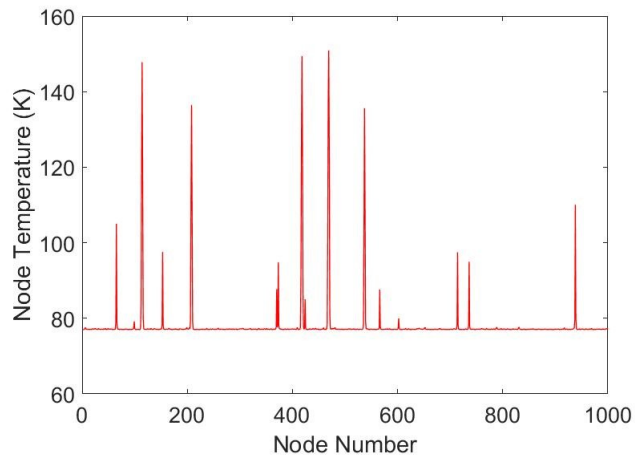
Figure 4.10: Temperature profile following 1.5 I_C over-current in FCL cable with 0.03 standard deviation of I_C

requirements set out in the previous section for each voltage level. In each case the number of superconducting tapes used is selected to provide the same stability margin for full load current calculated assuming a 10 MW cable operating at the selected voltage level. It is assumed that for higher current requirements a single cable is used rather than parallel arrangements, which may well be the case in the final design, to simplify the model.

The results of these simulations are shown in Figures 4.11 and 4.12 for the FCT and FCL designs respectively. These display the variation in peak cable temperature as a function of the operating voltage, fault current peak and critical current SD.

By inspection of Figure 4.11 it can be seen that the peak temperature of the FCT design remains below its critical temperature for the full range of voltages considered. Larger over-currents and greater critical current variations can still be observed to cause a higher peak temperature within the component though. In the worst case scenario considered, the highest temperature reached is approximately 83 K. This would have the effect of reducing the critical current significantly in the area concerned, which may necessitate removing the component from operation until normal operating temperatures are restored. This localized heating behavior may also necessitate a larger stability margin in setting the I_C of the cable to account for transient events such as fault ride-through. This leads to a greater amount of superconducting material used in the component, ultimately affecting cost. By inspection of Figure 4.11 it can be seen that localized heating effects are exacerbated at lower operating voltages. This is because the operating current is much larger and therefore Ohmic losses increase.

Figure 4.12 shows the variation in peak cable temperature as a function of the operating voltage, fault current peak and I_C SD for the FCL design. At over-current levels above 1.1 I_C, the superconducting layer is seen to quench at higher values of inhomogeneity. Indeed, most simulations above this current cause the hotspot temperature to reach the limit of the simulation, 150 K.

Figure 4.13 shows the time taken for the temperature to reach the thermal limit as a function of the operating voltage, fault current peak and I_C SD. It can be seen from this graph that the most important factor in determining how long it takes for the
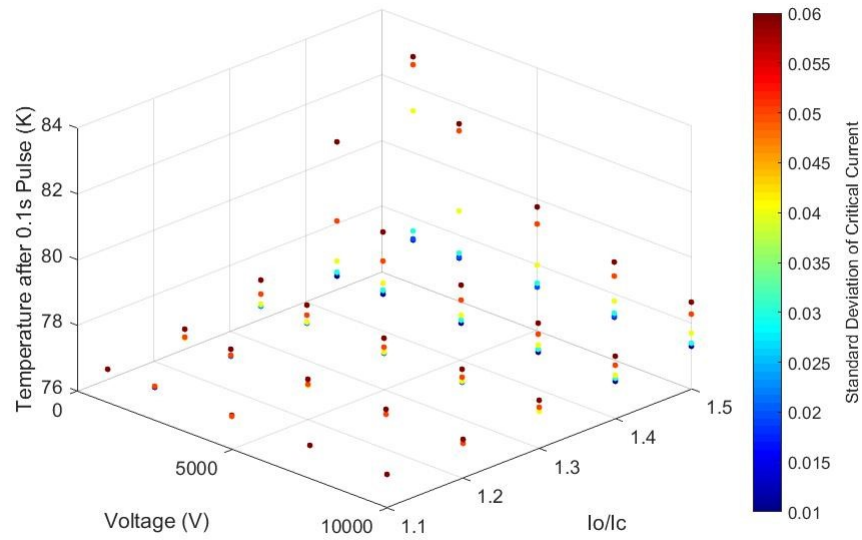
Figure 4.11: Peak temperature in superconducting layer following variable over-current pulse in FCT cable.
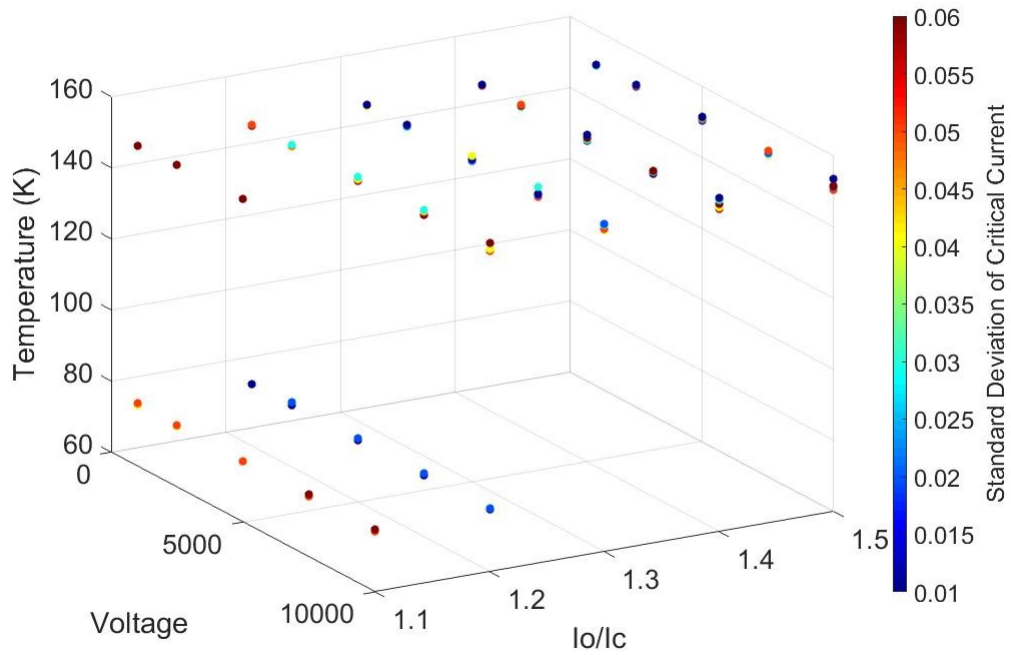
Figure 4.12: Peak temperature in superconducting layer following variable over-current pulse in FCL cable.
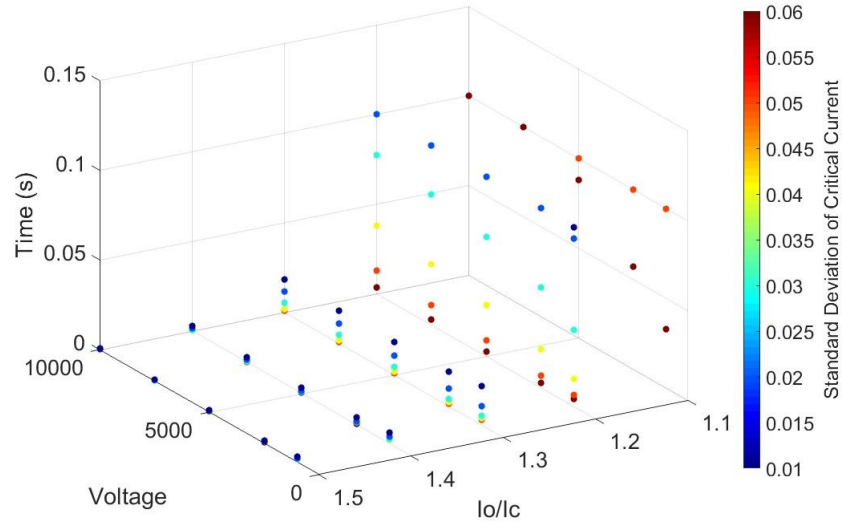
Figure 4.13: Time taken for the over-current pulse to cause the peak temperature in the FCL cable to rise above the 150K limit for the simulation.

superconductor to reach the thermal limit is the over-current level. Higher operating currents associated with lower voltages will lead to quicker quench inception, which occurs in nearly all cases of fault current magnitudes greater than 1.1 I_C

An approach to overcome this disadvantage of the FCL is to use a larger Stabiliser with a higher thermal conductivity. However, the relatively short cable lengths in aircraft applications results in insufficient cable resistance for damping fault current magnitude.

4.3   TeDP Thermal Protection Requirements Capture

4.3.1   Fault Current Limiting Effectiveness of an FCL Cable

For superconducting TeDP cables there is a need to define protection requirements in terms of maximum temperature the component is allowed to reach in order to be able to set interruption devices to respond fast enough. To assess temperature rise in a fault scenario containing an FCL superconducting cable in a TeDP aircraft, a pole to pole short circuit condition is considered for modelling and simulation. For this study a constant DC voltage is used to supply the fault current, I_F which is in turn calculated
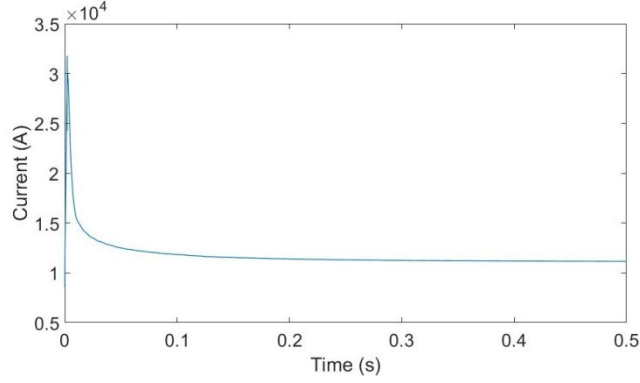
Figure 4.14: Fault Current profile in FCL cable for fault on system operating at 1 kV.

according to (4.9) where i_F is the instantaneous fault current, L is the inductance of the line (assumed to be 100 μH), $r_{FCL}(\Omega)$ is the instantaneous resistance of the cable, and V_0 is the operating voltage of the supply.

$$I_f(t+1) = \int_t^0 \frac{1}{L}(V_0 - i_f(t)r_{FCL}(t)dt \tag{4.9}$$

The range of voltage values considered in these simulations is as previously: 1 kv through 10 kV. The simulation run time is set to 500 ms although the simulation ends if the peak temperature of the tapes or the former exceeds 300 K (room temperature). As before, this temperature is selected as it presents a benchmark beyond which degradation is likely to take place. The inhomogeneity level is kept to a standard deviation of 0.01 for all simulations. It is assumed that the fault happens while a full load current is being drawn through the cables. Figure 4.14 shows the transient current profile through an FCL cable following the occurrence of the fault, with a network operating voltage of 1 kV.

Figure 4.15 shows the temperature profiles of the superconducting tapes in the FCL cables for the range of operating voltages considered. It can be seen that the temperature remains below the I_C degradation point throughout the superconducting tapes for all voltage levels considered. The temperature profile of the tapes is smoother compared to previous tests with small over-current levels, although there are clear areas where very large thermal gradients exist. This is because the fault current is
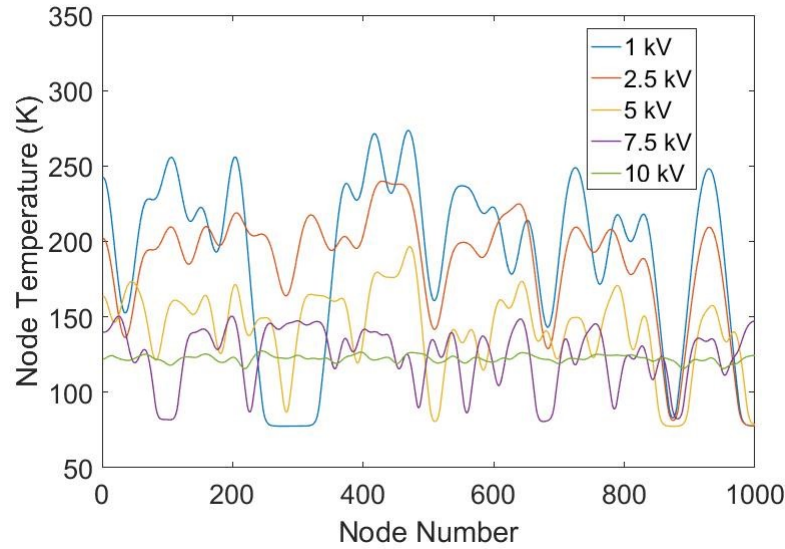
Figure 4.15: The Temperature profile of the superconducting tapes following fault current test in the FCL cable.

large enough to cause a uniform quench before the majority of the current begins to travel in the former material, with larger voltage levels causing greater uniformity due to the greater peak in fault current.

Figure 4.16 shows the temperature reached by the cable's stainless steel former and the time taken to reach that temperature. As shown, the cable former, which transports most of the current following the quench, dissipates much more of the heat in these fault cases, causing it to reach the 300 K limit faster than the superconducting layer during the period observed in all cases except the 1 kV scenario. This heat would transfer via conduction from the cable former to the much smaller superconducting layer, raising the temperature of the latter even after protection has acted to remove the fault. As such, the time graph of Figure 4.16 shows how quickly protection needs to act to prevent further heating that could damage the superconducting tapes for each scenario.

From Figure 4.16, it can be seen that for all operating voltages above 2.5 kV, the peak temperature in the former reaches the maximum temperature allowed by the simulation. This is in contrast to the previous simulations where small over-currents caused lower voltage systems to quench faster. The reason this occurs is two-fold.
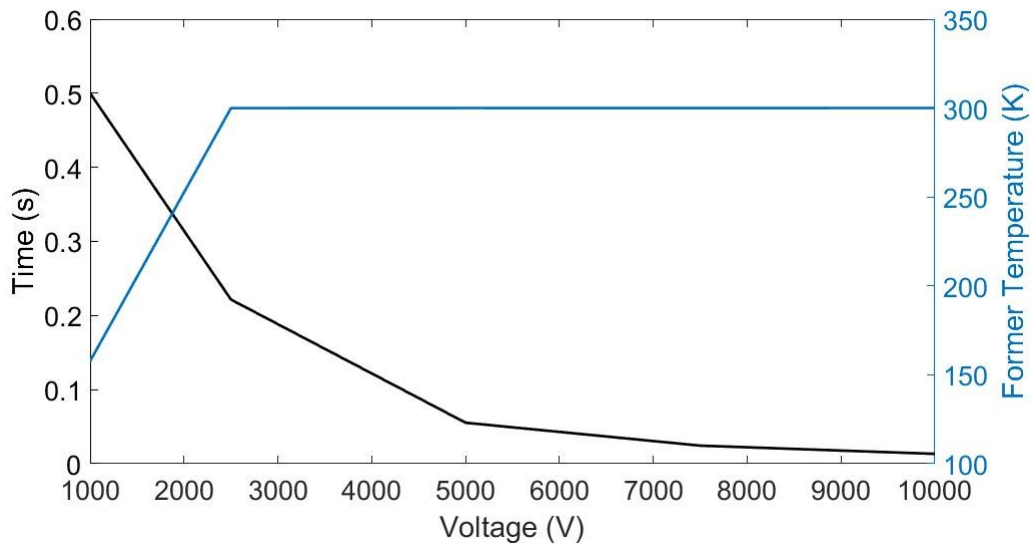
Figure 4.16: Time taken for fault current to cause temperature rise to reach 300K limit (black). Temperature of the former following simulation (Blue).

Firstly, the larger over-current caused by a high-voltage fault in combination with the lower I_c of the superconducting layer helps with uniformity of quench. This can be seen in the temperature profiles of the superconducting layers on Figure 4.15. Secondly, the higher operating voltages require a progressively higher resistance former to be utilised to provide sufficient fault current limiting (i.e. maintaining a constant V/R ratio). This leads to a smaller cross-sectional area of the former, effectively reducing the volume available to dissipate the heat energy of the fault current, causing swift temperature rise in the former.

This simulation also assumes a 100 m cable length which is near the upper bound of cable sizes that would be found on aircraft. Shorter feeder lengths can and will exist in TeDP aircraft. Reducing the length of cable would require the former cross sectional area to also be reduced to provide the same damping, greatly limiting the volumetric heat capacity available. This in turn means that a larger temperature rise would be observed in the cable former in the same time period, requiring protection to act even faster.

4.3.2 Maximum Recovery Temperature and Current

FCT cables have the ability to ride-through faults due to the highly conductive former limiting the temperature rise and ensuring the quenched zone spreads uniformly throughout the cable. However, as shown in this chapter, even a small temperature rise can lead to a significant reduction in critical current until the cooling system is able to remove the excess heat and lower temperature to normal operating conditions. In order for a FCL cable to ride-through a fault and return to normal operation this section will derive operating limits for superconducting cables in terms of maximum temperature that can be reached during a fault and the maximum current that can be carried after the fault takes place.

To develop thermal operating limits with respect to required operating current, two terms are now defined: maximum recovery temperature (MRT), and maximum recovery current (MRC). These will be the operating limits for the superconducting cable. MRT is defined as the maximum temperature the component can carry a given full load current without thermal runaway occurring. MRC is the maximum current that the component can operate at a given temperature without electrical losses leading to thermal runaway.

At the MRT the losses produced by the component, Q_{in} (J), is equivalent the amount heat the cooling system can remove, Q_{out} (J). These values can be calculated for a circular geometry of a cable operated in DC, where the primary loss mechanism considered is due to flux-creep, flux-flow and current sharing with conventional materials [84]. This is caused by operation near and above I_c. The equations for Q_{in} and Q_{out} are shown in (4.9) and (4.10) respectively.

$$Q_{in}(t) = I_{sc}(t)V_{sc}(t) \tag{4.10}$$

$$Q_{out}(t) = hA(T(t) - T_{cool}(t)) \tag{4.11}$$

Where h is the heat transfer coefficient in W/m^{2}K, A is the surface area of the cable in m^{2}2, and $T_{cool}(t)$ (K) is the temperature of the coolant, T (K) is the temperature

of the cable, I_{sc} and V_{sc} are the current carried and voltage dropped across the cable respectively. The voltage drop along the superconductor is calculated using the power law [44] and multiplying this by the length of the cable as shown in (4.11) where n is the transition index, $I_{sc}(t)$ is the instantaneous current carried by the cable and E_c is the quench voltage constant, $100 \ \mu$ V/m.

$$V_{sc}(I, T) = E_c L \left(\frac{I_{sc}(t)}{I_c(T)} \right)^n \tag{4.12}$$

The temperature dependent critical current is calculated according to (4.12) while the temperature dependence of the transition index is calculated according to (4.13) where T_c is the critical temperature and T_{ref} is a reference temperature. I_{cref} and n_{cref} are the critical current and transition index measured at a reference temperature while the indices k and ζ describe the nature of the temperature dependence for the critical current and transition index respectively [121].

$$I_c(T) = I_{cref} \left(\frac{T_c - T}{T_c - T_{ref}} \right)^k \tag{4.13}$$

$$n = n_{ref} \left(\frac{T_c - T}{T_c - T_{ref}} \right)^\zeta \tag{4.14}$$

At the MRT (4.9) and (4.10) are equivalent. Making this equivalency and substituting (4.11) into (4.9) gives (4.14):

$$I_{sc}(t) E_c L \left(\frac{I_{sc}(t)}{I_c(T_{MRT})} \right)^n = Q_{out}(t, T_{MRT}) \tag{4.15}$$

Solving (4.14) for $I_{sc}(t)$ allows for the maximum current carried by the cable, I_{MRC} at the MRT to be calculated in accordance with (4.15).

$$I_{MRC}(t, T) = \sqrt[n+1]{\frac{I_c(T_{MRT})^n Q_{out}(t, T_{MRT})}{E_c}} \tag{4.16}$$

This relationship is represented on Figure 4.17 for a cable with an arbitrarily selected critical current of 1000 A operating with a coolant temperature of 77 K, the boiling point of liquid nitrogen under atmospheric pressure. A heat transfer coefficient of 0.2
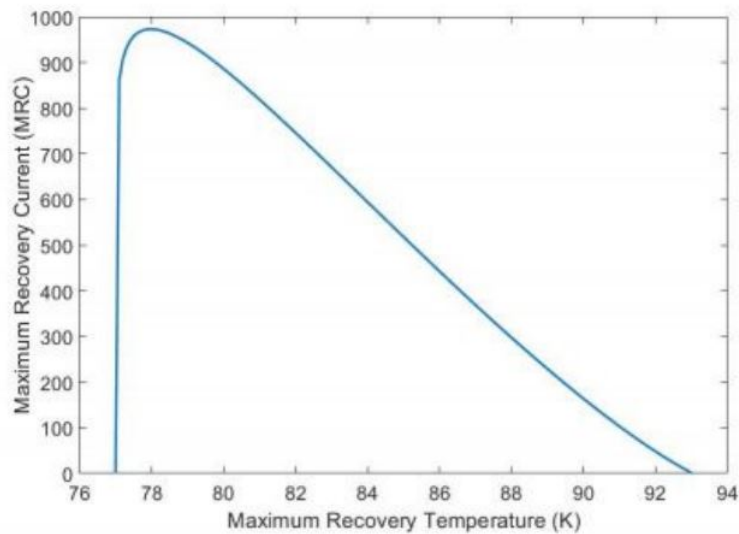
Figure 4.17: Example of MRC w.r.t MRT

W/m^{2}K is used and is assumed to be constant. The rapid rise at 77 K to the peak value is because the cooling system only removes energy from objects of higher temperature than the coolant.

Figure 4.17 demonstrates the relationship between the maximum current that the superconductor can carry at a given temperature without thermal runaway occurring based on the cooling system power and superconductor parameters. With knowledge of the systems required operating current, the protection requirements can then be calibrated such that interruption must react to remove a fault before the temperature reaches the MRT for that desired current. These curves can also be used to determine the appropriate critical current that a superconducting distribution feeder should have based on the specific cooling system capability. And, as will be shown in the proceeding chapters, this measure can be useful aid for sizing cables and within a control system.

4.4 Chapter Summary

This chapter explored the use of an FDM based component level model in order to investigate the factors that can influence the severity of hotspots and the impact of different cable design philosophies on this failure mode. It was shown that at conditions

near and above the critical current, FCL based cables are more prone to hot spot formation and localized thermal runaway than FCT based designs due to the much lower thermal and electrical conductivity of the conventional materials used in their construction.

As well, it was demonstrated that given the relatively short lengths of cable run expected on a TeDP aircraft, FCL cables are shown to be unable to limit fault current to a significant degree without an unacceptably large temperature rise that is likely to lead to degradation. Thus if FCL capability is a requirement for the TeDP protection system, a standalone device is required.

Despite being less prone to hotspots, it was demonstrated that even a small (<10K) temperature rise, can lead to a significant drop in critical current within FCT based designs until temperatures return to normal. This could make FCT cables more vulnerable to subsequent fault events or lead to the cable being removed from service since the critical current has dropped below the required operating current. To this end this chapter concluded by deriving a protection requirement that links operating current requirements to maximum allowed temperature rise based on the capability of the cooling system. The subsequent chapters will use these new definitions of MRT and MRC as constraints to optimise the sizing and control of superconducting feeder cables in TeDP systems during fault ride-through scenarios.

Chapter 5

Sizing of Superconducting TeDP Cables Using a Particle Swarm Optimisation Approach

5.1 The Superconducting Cable Sizing Problem

The electrical protection system influences the weight of a TeDP network directly through the mass of breakers, relays, fuses, and associated measurement and control equipment. The contribution that protection components have towards the total electrical power system weight for proposed TeDP architectures such as NASA's N-3X is considerable, as highlighted in [29], which demonstrates that up to 20 % of overall system mass is due to protection equipment. However, protection requirements also indirectly increase the mass of the network through ride-through requirements in the form of fault level and interruption time (protection speed) impacting fault energy dissipation within non-faulted components, with the former being dependent on the architecture and system variables, and the latter on the capabilities of the protection system to detect and remove the fault.

Protection requirements for future superconducting systems are not well defined in the literature. However, it is not unreasonable to assume that superconducting cables will need to be able to provide the same level of ride-through capability as modern con-

ventional components, ensuring that electrical faults do not lead to significant isolation of the electrical network upstream of the fault location. For superconducting systems, these requirements are made more difficult by the need to maintain the superconducting state, which requires that the superconducting component is always operated within the boundaries of the critical surface [44]

As seen in the previous Chapter, electrical faults can lead to large amounts of power being dissipated within superconductors as heat, raising the component's temperature, which has the effect of temporarily reducing critical current until temperature is brought back to its pre-fault setting. This affects all components within the fault path, not only the faulted component. As such, following a fault, otherwise healthy components may have to be removed from the network due to no longer being able to provide the required load current without thermal runaway, as the increased temperature has reduced its maximum loading capacity (MRC) due to them being in the fault path.

Within conventional cables the typically larger volumes and greater heat capacity of components provide protection systems with suitable time margins within which to act following a fault. For superconducting cables to provide safety margins that allow for ride-through capability, they must be sized appropriately with respect to four variables: the size of the superconducting layer which affects the maximum value of the critical current; the size of the conventional cable former that provides an alternate path for current to flow through during over-current conditions, the power rating of the cooling system to remove heat from the cable, and the speed at which the protection system can operate to interrupt the fault current.

Considering only the internal factors of the cable design, the ride-through capability of a superconducting cable is dependent on the size of the conventional (non-superconducting conductor, e.g. copper) and superconducting materials used in the construction of the cable. Having a larger amount of conventional material reduces the resistance of the shunt former while increasing heat capacity [105]. This reduces temperature rise during a fault at the expense of increasing capital cost and weight. Similarly, increasing the amount of superconducting material increases the critical current of the cable which is the maximum current the cable can carry before superconductivity is lost

and Ohmic heating occurs. Increasing the base critical current level of the cable allows for a greater temperature rise before critical current reduces below normal operating current (load current > MRC). Hence, this approach increases ride-through capacity at the expense of greater capital cost due to the use of more superconducting material. However, due to the high current densities of superconducting materials, the impact on final component weight is negligible.

Under-sizing superconducting components could lead to a damaging temperature rise during faults alongside limiting the power delivered to key network loads following a fault ride-through [123]. Conversely, over-sizing superconducting components causes an increase in weight and volume as well as capital cost. This is significantly detrimental to a superconducting distribution network for TeDP as it reduces the overall efficiency of the system: greater fuel burn per flight and greater number of flights required to recoup capital expenditure. This presents a multi-objective optimisation problem between minimising cable costs while maximizing system fault tolerance which this chapter seeks to address

These factors create a trade-off, which requires optimisation, between increasing the amount of superconducting material, leading to greater capital expense, and increasing the amount of conventional material, significantly increasing running costs, in order to achieve the appropriate ride-through capability for the application. Further, mass penalties in aviation are typically proportional to fuel price, which can vary significantly over time. However, a framework for optimising superconducting cable parameters with respect to capital cost, weight, and system protection requirements within a DC mini grid for future aircraft electrical networks has thus far not been presented in the literature. To this end, this chapter addresses the superconducting cable sizing problem by presenting an optimisation approach to size cables with respect to MRT and MRC constraints outlined in the previous chapter. This is to allow for a minimisation of cable cost, while ensuring ride-through capability with respect to network requirements.

5.2 Particle Swarm Optimisation Implementation

5.2.1 Methodology

The superconducting cable sizing problem for TeDP requires that the cable configuration, in terms of superconducting and conventional material area, minimises the lifetime cost of the cable. Costing must include consideration of both initial upfront and operating expenses. Upfront cost considers the cost of the materials used in the cable's construction while operating expenses include the impact on aircraft fuel consumption due to cable mass. The selected cable must also be able to withstand fault ride-through conditions and return to normal operation once a fault is cleared. Solving this cable sizing problem is dependent on a number of factors:

1. Full load current requirement.

2. Material constants: superconducting surface parameters, heat capacity, density, resistivity etc.

3. Fault severity.

4. Protection system operating speed.

5. Environmental conditions: operating temperature, cooling power.

6. Cost of materials, manufacturing, and fuel.

These factors need to be accounted for in the optimisation process to ensure that the cable is able to provide fault ride-through capability while ensuring cost-effectiveness. Due to the wide variety of optimisation variables and the complex constraints that must be accounted for, a meta heuristic method such as particle swarm optimisation (PSO) is a good candidate for finding solutions due to its low computational effort, simple implementation, ability to converge quickly and with a high probability of finding the global best solution [124]. This allows for more computational effort to be used in evaluating the constraints, which requires the simulation of a complex engineering system.
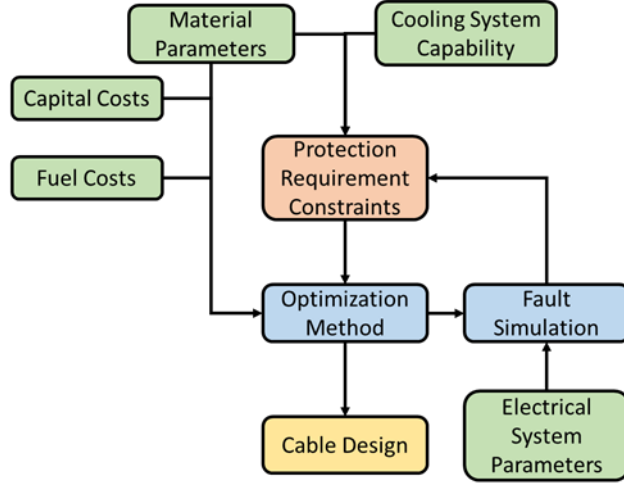
Figure 5.1: PSO Velocity Update Illustration

Figure 5.1 shows the methodology proposed by this chapter for the determination of
optimal cable design. As shown here, environmental, electrical, protection, and material
parameters are used within a fault simulation to determine whether the cable design
found at any given point during the process breaks the constraints of the protection
requirements, while the capital and operating costs (fuel burn due to cable weight)
are used to evaluate the fitness of the solution selected. If at any time during the
process, a selected cable design breaks the constraints, it is penalized through a penalty
function(Section 5.2.3). The fitness function for optimisation used here is described by

$$f = K_{sh}A_{sh} + W_{sh}A_{sh} + K_{su}I_c + W_{su}I_c \tag{5.1}$$

where K_{sh} ($/m^2) is the capital cost coefficient of the conventional shunt materials
and K_{su} ($/m^2) is the capital cost coefficient of the superconducting materials, defined
in (5.2) and (5.3), A_{sh} is the cross-sectional area of the conventional material, W_{sh}
($/kg) is the weight coefficient of the conventional material and W_{su} ($/kg) is the
superconducting weight coefficient, defined in (5.4) and (5.5), and I_c (A) is the critical
current.

$$K_{sh} = \sigma_{cu}l_e M_{shcap} \tag{5.2}$$

$$K_{su} = \sigma_{su} l_e M_{sucap} \tag{5.3}$$

$$W_{sh} = \sigma_{sh} l_e O \tag{5.4}$$

$$W_{su} = \sigma_{su} l_e O \tag{5.5}$$

Where σ (kg/m^3) is the density of the material, l_e (m) is the length of the cable, M ($/kg) is the capital cost per unit kg of the material and O ($/kg) is the cost of fuel per unit kg of material.

5.2.2 Particle Swarm Optimisation

First proposed in 1995 [124], particle swarm optimisation (PSO) is an evolutionary strategy inspired by the social behaviour of birds and other animals in their search for food. PSO consists of a set number, swarm, of particles moving through a search space in which every location is a potential solution to the objective function that requires optimisation [124]. Each particle uses knowledge of its own best solution and that of the swarm as a whole in order to navigate this solution space before converging on the best answer found by the swarm. This allows for an efficient search process much quicker than brute force methods [124].

In order to find the global minimum or maximum within this search space each particle tracks the location of its personal best known solution, P_{best}, and the best known solution that any particle within the swarm has managed to find, G_{best}. Upon every iteration of this technique the objective function is evaluated for each particle, i, and their current positions, X, in each dimension, j, is updated according to their current location and the answer to the velocity vector equation:

$$V(i, j) = \phi V(i, j) + R_1 C_1 (P_{Best} - X(i, j)) + R_2 C_2 (G_{Best} - X(i, j)) \tag{5.6}$$

The correction coefficients C_1 and C_2 describe the cognitive and social capacity of the particles respectively, essentially how much the particle wants to move in the
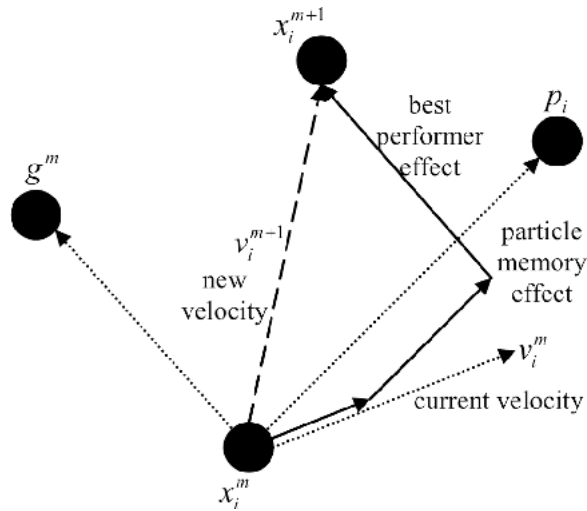
Figure 5.2: PSO Velocity Update Illustration [125]

area of its personal best solution and how much the particle wants to move toward the
best known location within the swarm. It is this communication between individual
particles and the overall swarm that allows for convergence to occur. R_1 and R_2 are
random numbers between 0 and 1 that add a random element into the movement of the
particles. ϕ is the inertia of the particle, the amount the particle wants to move in the
direction its currently headed. Positions are updated on each iteration of the technique
according to (5.7). Figure 5.2 gives a graphical representation of this process.

$$X(i,j) = X(i,j) + V(i,j) \tag{5.7}$$

Figures 5.3 through 5.6 show an example of particles movement through the search
space before achieving convergence on the best solution found by the swarm. It can be
seen in Figure 5.3 that the particles start out with a diverse range of values and the
search area becomes narrower as the algorithm progresses, Figure 5.4. Because of the
stochastic nature of the technique, PSO cannot guarantee that the best solution found
by the particles is the global optima. This issue can be mitigated however by running
the algorithm multiple times to improve the probability that the global optimum is
found.

Figure 5.7 shows a flow diagram for the particle swarm optimisation process as it
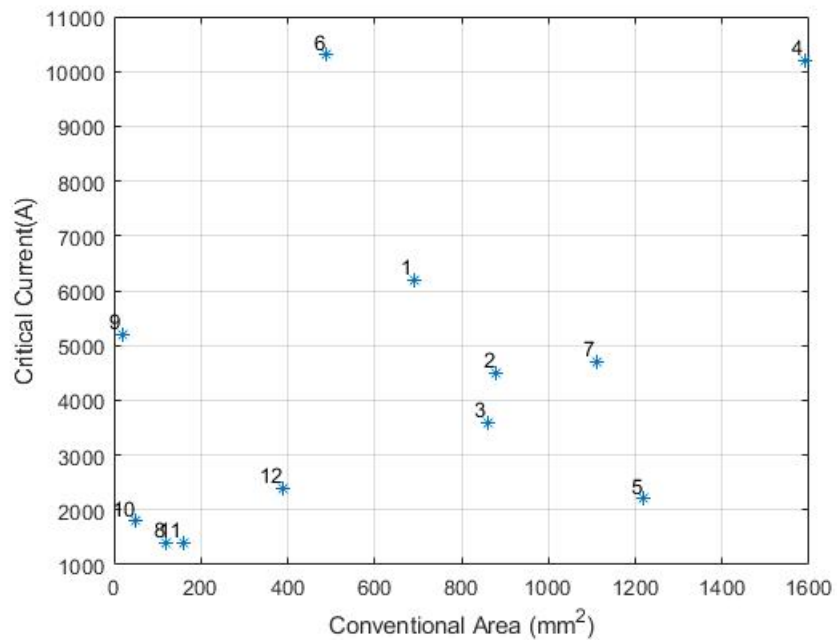
Figure 5.3: PSO Algorithm: particle positions in search space at initiation
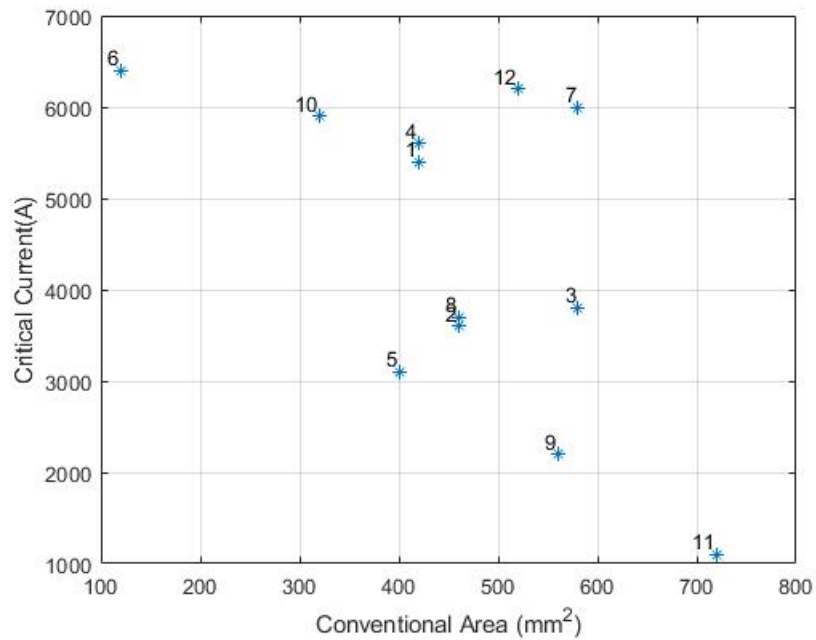
Figure 5.4: PSO Algorithm: particles conduct a wide search of the solution space.
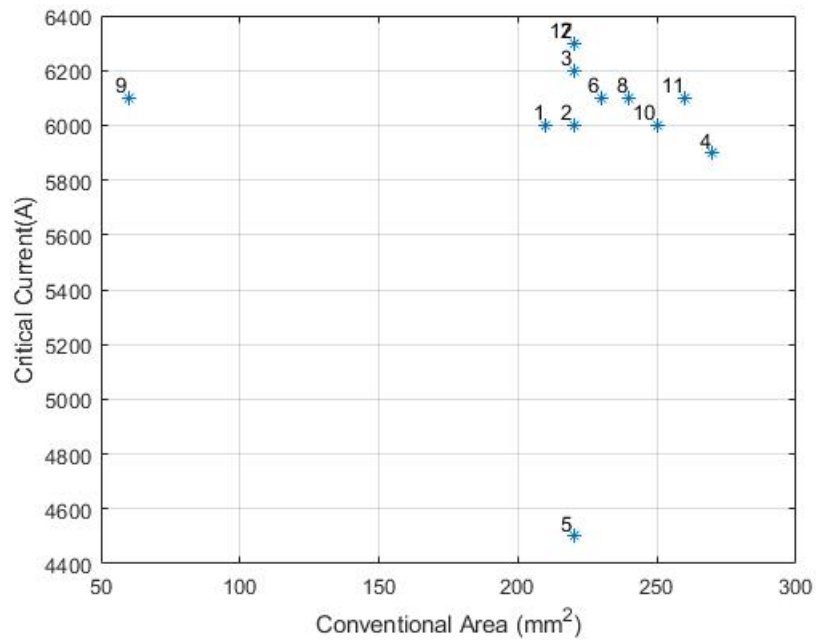
Figure 5.5: PSO Algorithm: particles start to converge in area of good solutions.
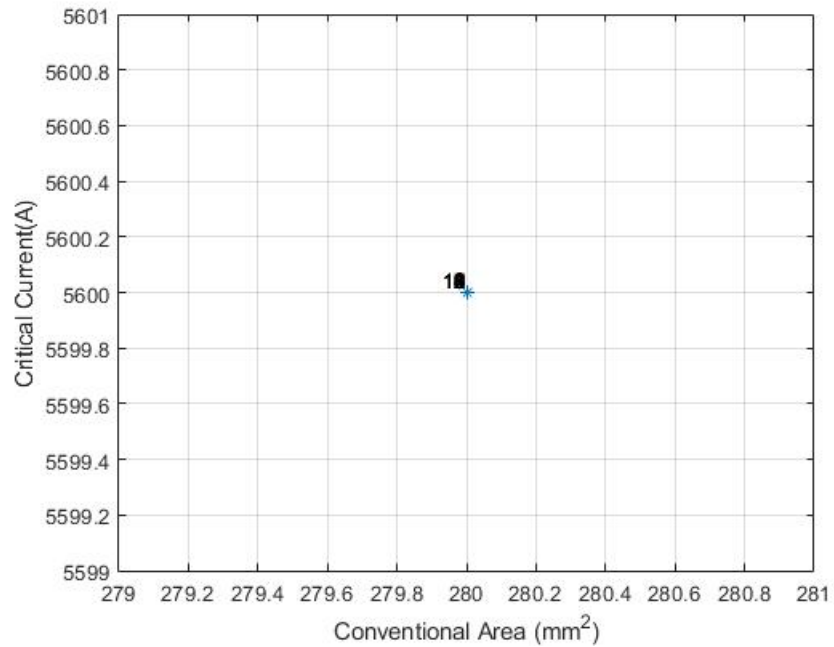
Figure 5.6: PSO Algorithm: particles converged on best solution found.

relates to this problem. It describes that at each iteration of the optimisation, a fault
simulation is carried out for each cable configuration. This is stored in the particle's
location data: the size of the superconducting layer; the size of the cable shunt area.
The particles fitness is then updated according to (5.1) before any penalties are applied
using the constraints procedure. Particle velocities are updated according to (5.6) and
the process begins again until the particles converge on the best solution found by the
swarm.

5.2.3   Constraints Handling

To prevent the PSO process from producing unviable results a constraints handling
procedure is required. This first requires definition of the constraints themselves. These
were defined as follows:

1. At nominal operating temperature, the cable must be able to provide the maxi-
   mum operating current without quench occurring.

2. Following the fault the cable must be able to supply a percentage, k, of the full
   load without quench occurring.

The first constraint is that the critical current of the cable must be large enough
so that the cable does not quench in normal operation. The second constraint ensures
that the cable has ride-through capability so that in the event that a fault happens
downstream on the network, it is able to provide some portion of the full load current
without thermal runaway. This will normally be the maximum operating current but
could be reduced if the system has a significant number of redundant paths and energy
storage to allow for reduced power flow on the affected feeder while the cooling system
removes excess heat. This would have the benefit of reducing the volume, and weight,
of each cable.

Determining whether the particle breaks the second constraint is achieved by deter-
mining the maximum temperature the cable reaches during the fault and checking if it is
greater than the maximum recovery temperature (MRT) for the required load current.
The MRT is the maximum temperature that the component can reach while still being
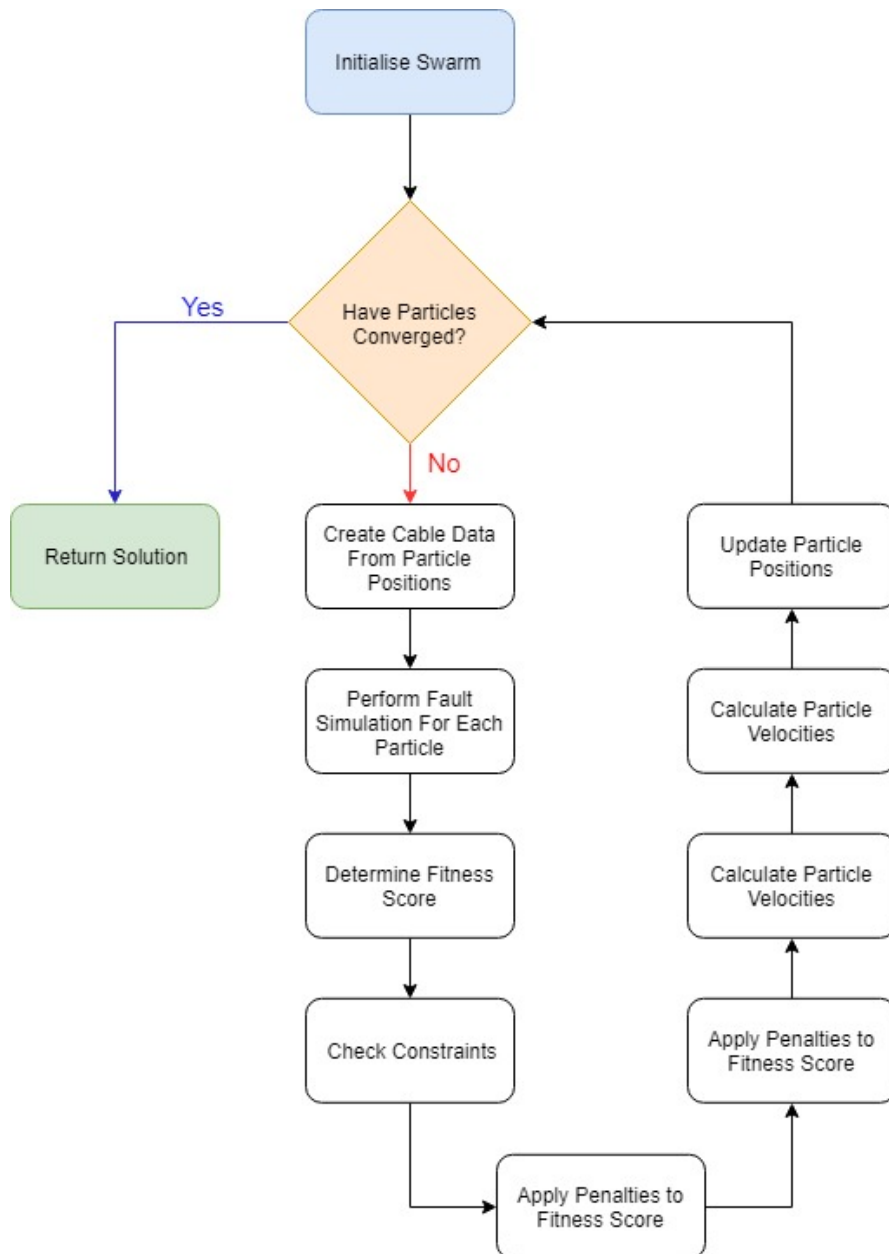
Figure 5.7: Flow diagram of PSO algorithm implementation in Matlab.
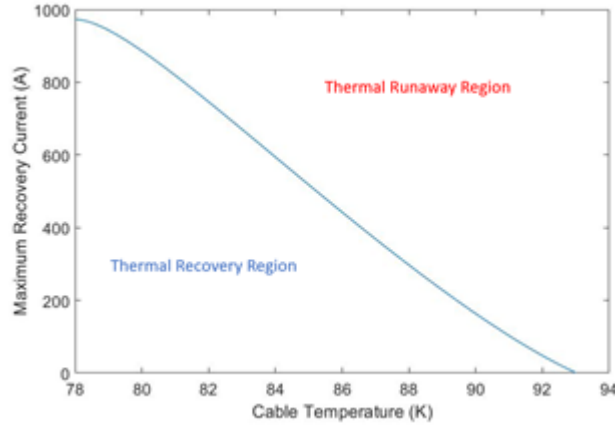
Figure 5.8: Maximum Recovery Current against Cable Temperature with marked Thermal Recovery and Runaway Regions. [123]

able to carry a set amount of current, the maximum recovery current (MRC), without thermal runaway occurring, Chapter 4.3. As the temperature of a superconducting cable increases, the MRC decreases due to the inverse nature of the critical current to critical temperature and the limitations of the cooling system to remove excess heat. Figure 5.8 shows an example of the relationship between cable temperature and MRC for a superconducting cable with I_c of 1000 A at 77 K with regions marked to indicate the thermal recovery and runaway operating zones [123].

Due to the nature of the PSO process, some particles will be in the infeasible region of the solution space. This is the part of the search area in which solutions violate constraints. Due to the invalidity of these solutions, it is undesirable for convergence to take place within this area. To prevent this a number of strategies have been developed for PSO, from which, the authors in [126] provide an overview of many of the most commonly adopted ones. The implementation presented in this chapter uses a dynamic penalty function. This punishes particles for entering the infeasible region. The penalty functions are given in (5.8) and (5.9).

$$\gamma_{i_1} = \tau_1 (I_{c_{min}} - I_{c_i}) \frac{n}{M} \tag{5.8}$$

$$\gamma_{i_2} = \tau_2(I_{MRC_{req}} - I_{MRC_i})\frac{n}{M} \tag{5.9}$$

Where γ is the penalty given for each constraint, τ is the penalty multiplier, $I_{c_{min}}$ is the minimum critical current under normal conditions, I_{c_i} is the critical current in normal conditions for particle i, $I_{MRC_{req}}$ is the maximum recovery current required by system, I_{MRC_i} is the maximum recovery current of particle i after the fault simulation, n is the iteration number, and M is the maximum number of iterations.

The penalty reduces the fitness score of a particle and thus discourages particles from searching that area for a solution. The penalty function penalizes the particle relative to both the iteration number and the amount by which it exceeds the constraint. By implementing the penalty function this way the particles can more easily explore areas near the infeasible region early in the algorithm. This is beneficial as many of the best solutions can often be located on the boundary of the feasible region. As the iteration number increases, the function ensures that particles are discouraged from staying in the infeasible solution space.

5.2.4   Fault Circuit Modelling

At each iteration of the methodology a fault simulation is carried out for every particle, with a superconducting cable being created using the size of I_c and former area stored within the particle's location within the search space. The electrical circuit used to model the rail-to-rail DC fault for each step of the algorithm is shown in Figure 5.9. It is assumed that electrical power is generated on the TeDP aircraft from a generator, driven by a gas engine. This power is converted to DC by a rectifier, interfacing to a DC distribution system. The superconducting cable is modelled with superconducting material in parallel with a metallic former. Upstream, a constant DC voltage source behind an impedance represents a generator-fed rectifier. In the event of a rail-to-rail fault, the DC link capacitor, C_f, will discharge, significantly influencing the peak fault current size and shape. Sustained, lower magnitude fault current is provided by the generator interfaced through the rectifier to the DC section of the system.

The impedance of the generator, Z_{gen} (Ω) is determined by the apparent power of
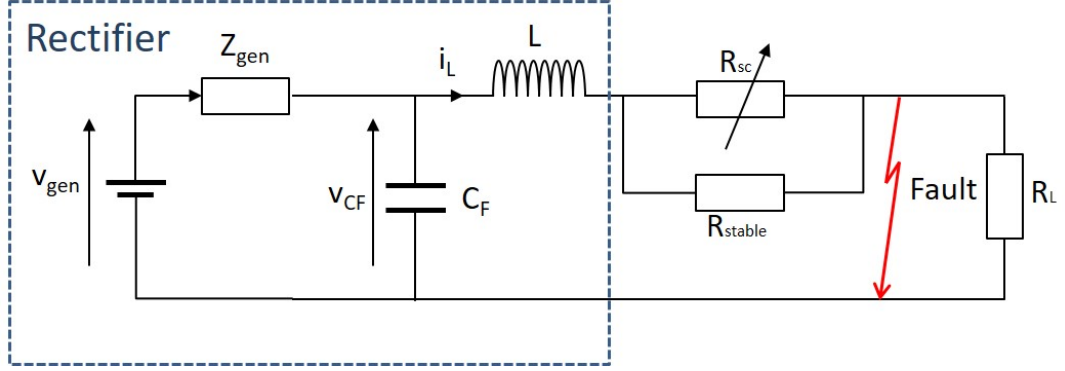
Figure 5.9: DC-link fault circuit for use in PSO simulations.

the generator, S_{gen} in VA, and the operating voltage, $V_gen,(V)$ as shown in (5.10)

$$Z_{gen} = \frac{S_{gen}}{V_{gen}} \tag{5.10}$$

It is assumed that the inductive component of the impedance of the generator
is significantly greater than the resistive portion. Hence the resistive element of the
impedance of the generator is neglected. The inductance is calculated by :

$$L_{gen} = \frac{Z_{gen}}{2\pi f_{gen}} \tag{5.11}$$

The filter capacitor, C_{gen} is sized in accordance with (5.12) where f_{sw} is the switch-
ing frequency in Hz [127].

$$C_{gen} = \frac{S_{gen}}{V_{gen}^2} \frac{6}{\frac{2\pi}{\frac{6}{20}} f_{sw}} 6 \tag{5.12}$$

The impedance of the superconducting cable at each time step in the fault simula-
tion is determined by the current sharing between the superconducting and conventional
material. This is in turn calculated by the current-sharing algorithm, explained earlier
in Section 3.2. For this case it is assumed the cable has a uniform critical current. The
state equations for the fault are extracted from the circuit in Figure 5.7 and are solved
for each time step using MATLAB's ode45 function [128]. These are given by (5.13)
through (5.15):

$$I_{L_{gen}} = L_{gen}\frac{di_{gen}}{dt} \tag{5.13}$$

$$V_c = C\frac{di_c}{dt} \tag{5.14}$$

$$V_{L_f} = Lf\frac{di_f}{dt} \tag{5.15}$$

The temperature of the component is then calculated as the time integral of the power dissipated during the fault, divided by the components heat capacity. The heat capacity, c_{pi}(K/J), and resistance of shunt built into the cable, R_i, are determined by the size of the particles shunt surface area, A_i (m^2), and the fundamental properties of the material:

$$R_i = \frac{\rho L}{A_i} \tag{5.16}$$

$$c_{pi} = A_i L c_{vi} \tag{5.17}$$

Where L (m) is the length of the cable, $\rho(\Omega m)$ is the resistivity of the material, c_{vi} (J/m^3) is the volumetric heat capacity. This continues until the stopping point of the simulation is reached. This is in turn determined by the circuit breaker operating time. The temperature reached during the simulation is then passed back to the main PSO loop to determine if the particle's current location in the search space violates constraints.

5.3 Sensitivity Analysis with PSO

5.3.1 Optimisation Set-up and Parameters

Particles are initialised randomly within the space and their positions, fitness and velocity continually updated until convergence occurs. The optimisation and simulation parameters are shown on Table 5.1. For each case selected, which considers different

Parameter	Value	Parameter	Value
Number of Particles	12	Power Level	10 MW
Maximum Iterations	100	Fault Impedance	1e-2 Ω
Number of Swarms	3	Former Resistivity	2e-9 Ω.m
Fault Simulation Time Step	0.001s	Cable Length	100 m
Post Fault Current Requirement	100 %	Frequency	50 Hz
Superconducting Material	YBCO	Former Cost Coeff.	4.05
Coolant Temperature	65 K	Superconductor Cost Coeff	400.5
Heat Transfer Coefficient	0.2 W/mK	Weight Factor	50
Critical Temperature	93 K	Heat Capacity	185
Density	8940	Cable Inductance	1e-5 H

Table 5.1: Values used in Particle Swarm Optimisation Process

voltage levels used for the network and circuit breaker operating times, the algorithm runs the PSO method three times. This is to reduce the chance that a sub-optimal result is returned due to particles gravitating towards local minima in the search space. The output of a swarm is two cable parameters: conventional shunt material area and a superconducting critical current.

From the base case described in Table 5.1, which considers a 10 MW subsection of a TeDP system, the voltage is varied between 1 kV and 10 kV in steps of 250 V. Although the frequency is set at 50 Hz, in accordance with UK grid, aircraft normally operate at higher frequencies (400 Hz) and TeDP may utilise much greater frequencies than this for generation. The particles are allowed to select values for the shunt former in steps of 10 mm^2 while they can select the I_c in intervals of 100 A. This ensures only discrete values are selected and helps prevent flat basin situations wherein multiple regions of the search space have very similar fitness, causing convergence speed to reduce. It is assumed that the selected cable will need to be able to withstand full load current following the fault without thermal runaway taking place.

The cost of copper is assumed to be £4.05/kg, the market price for the metal at time of writing [129], ignoring the cost of the manufacturing that goes into the superconducting cable. Similarly the cost of the YBCO tape is assumed to be approximately two orders of magnitude greater than the cost of copper. The weight factors, (5.4) & (5.5), multiplies the cost of materials based on mass, in an attempt to simulate the cost of fuel, which can vary widely depending on a large range social, economic, and
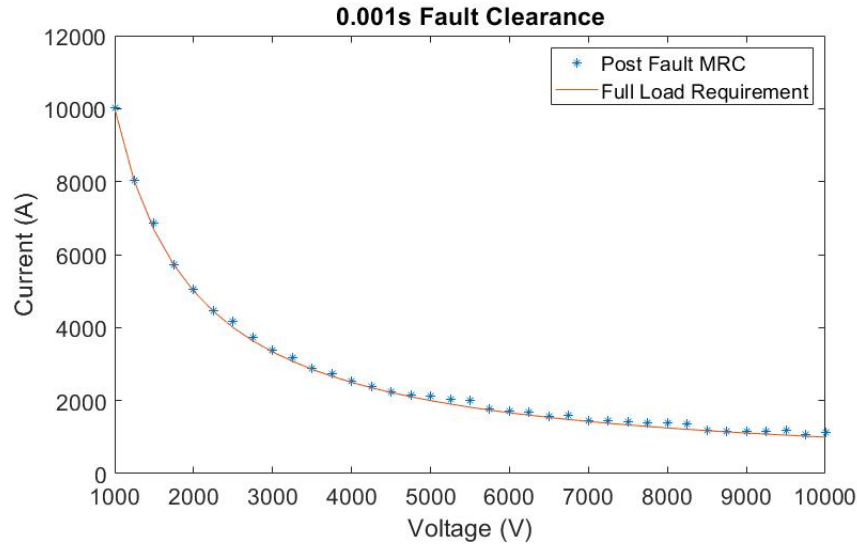
Figure 5.10: Post fault MRC and Full load requirement against voltage shows that particles have found solutions on the boundary of the feasible search space.

political factors. This is set at 50 as Airbus estimates that for every kg of weight on an aircraft, the aircraft requires an extra 50 kg of fuel over the course of a year [16].

5.3.2 Convergence on MRC Boundary Line

Figure 5.10 shows the MRC of the best cable found by the algorithm at the post-fault operating temperature for a fault that is cleared in 1 ms across the full voltage range considered in the study. Also shown on this figure, in the solid red line, is the full load current that each cable is required to transmit for the corresponding voltage level.

It can be seen from Figure 5.10 that the cable configurations found by the PSO tool are capable of withstanding the fault and are able to provide full load current post fault as required, satisfying the constraints that were set. The post-fault MRC of each configuration can be seen to be along the border of the full load current requirement. This is a strong indicator that the algorithm is able to find global optimal solutions. This can be deduced logically as any increase in CSA or critical current will push the post fault MRC up due to the increased heat capacity. This increases the cost of the cable without providing additional utility, required current capacity will never be greater than full load. Similarly any decrease in the CSA or critical current will
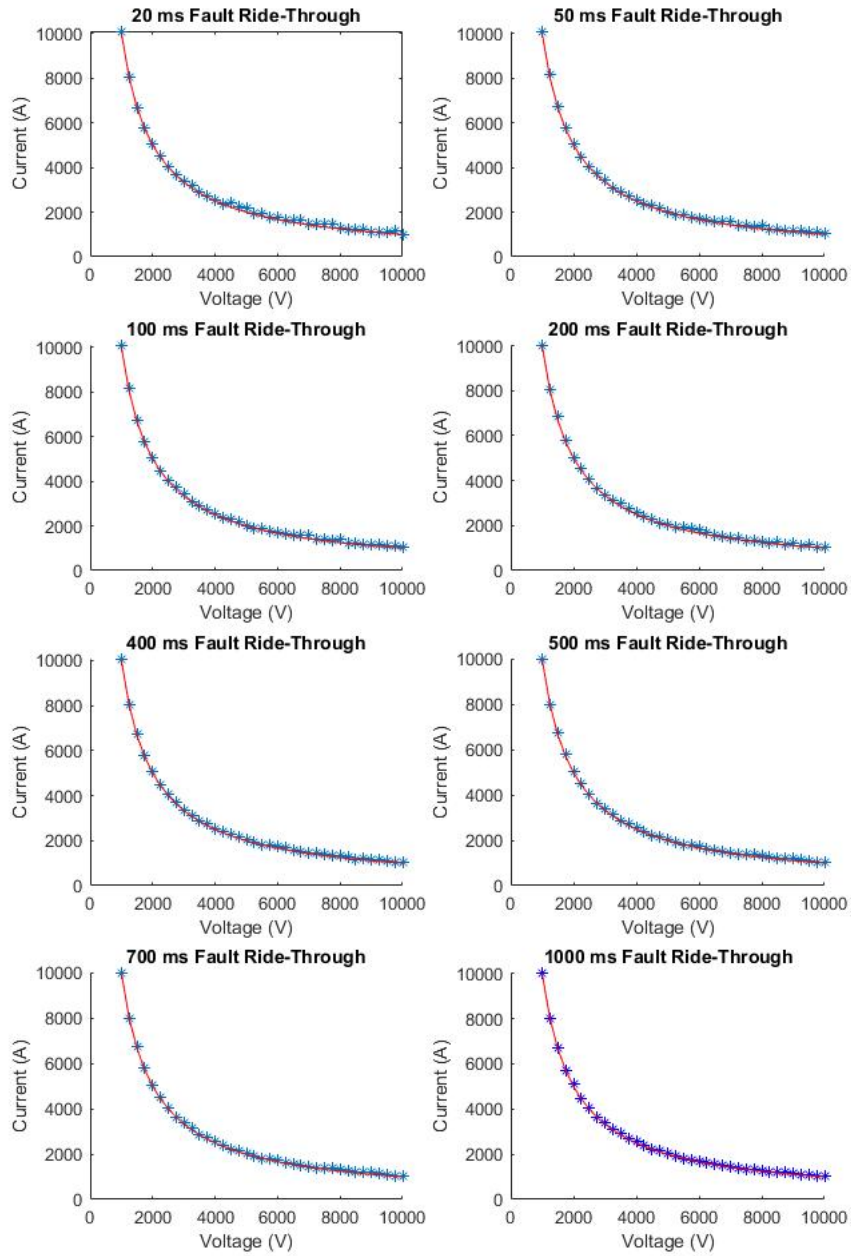
Figure 5.11: PSO algorithm finds solutions on the boundary of the feasible search space at every ride-through requirement.

cause the MRC to drop below the red line, breaking the post fault current carrying requirement constraint in Table 5.1 and rendering the solution invalid. Figure 5.11 shows that for a range of fault times considered, the PSO algorithm is able to find solutions along the boundary of operational constraints, showing that the optimisation technique is robust to changes in the underlying system conditions.

5.3.3 Influence of System Variables on Best Cable Design

Figure 5.12 shows the influence of voltage and fault clearance time on the overall cost ($) of the best cable configuration the algorithm has found that is able to satisfy the constraints. It can be seen from this figure that increasing voltage can reduce the cost of the cables required, with the effect being more pronounced at lower voltages. This is due to steady state current carrying requirements reducing in line with increasing network voltage, reducing the critical current and CSA requirements of the cable and therefore cost. However, as the clearance time increases, the cost of the superconducting cable selected by the optimisation method increases for each network voltage due to the greater amount of energy that must be absorbed by the cables.

Figures 5.13 and 5.14 indicates that critical current sizing and shunt size decreases as the voltage increases. Reduction in critical current requirement is likely due to a reduced operating current for the same power level. Longer fault durations require greater base critical current and shunt size. This ensures that the superconductor's MRC does not drop below the required load due to the higher temperatures reached by the component during these fault durations as shown in Figure 5.15. Greater temperature rise occurs at higher voltages as the optimisation algorithm determines that a larger critical current base, according to the parameters of the case study in Table 5.1, is a less expensive solution than preventing greater temperature rise through an increase in shunt area.

From the best fit lines in Figure 5.15, it can be seen that peak temperature generally increases with voltage level, and this is more pronounced at faster interruption times. An explanation for this effect is the greater impact of the capacitive discharge on temperature rise at higher voltages where there is more energy stored on the capacitor,

127
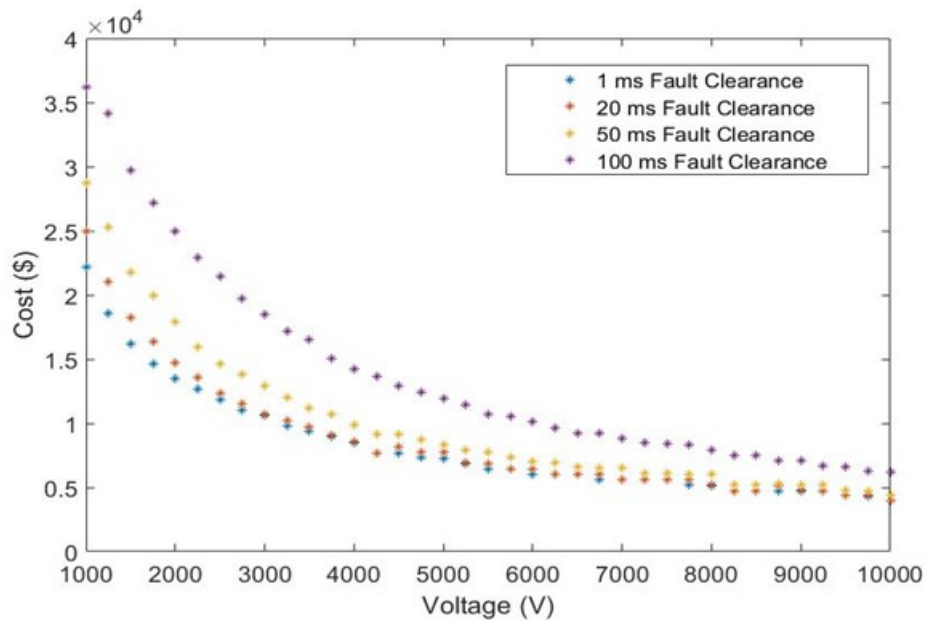
Figure 5.12: Cost of optimised superconducting cables at different voltage levels and
ride-through time requirements.
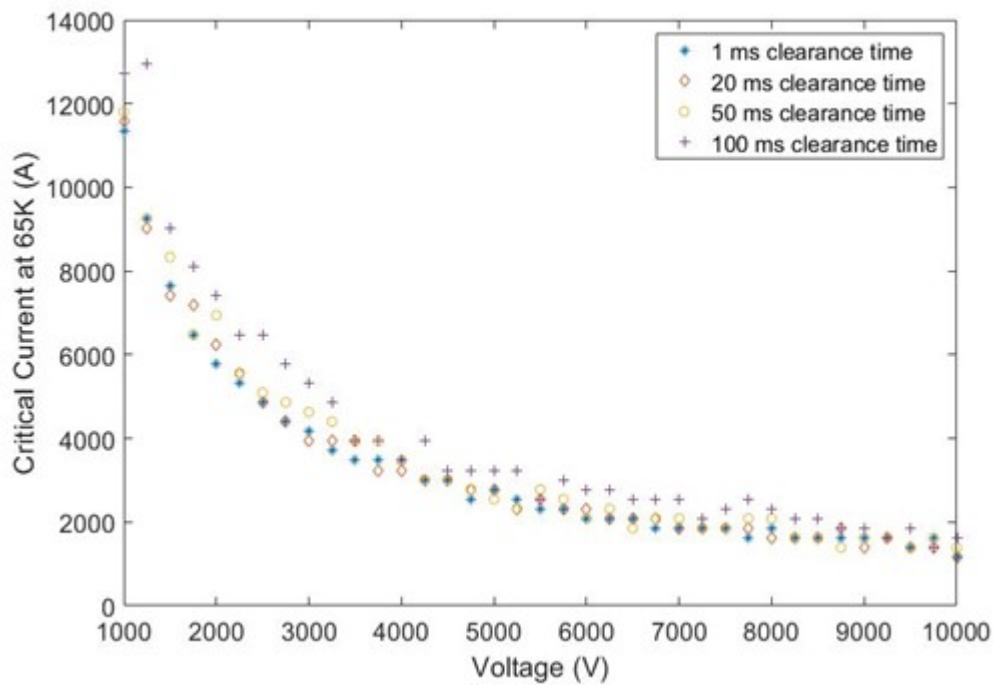
Figure 5.13: Critical current selected by the PSO algorithm for each voltage level and
ride-through time requirement.
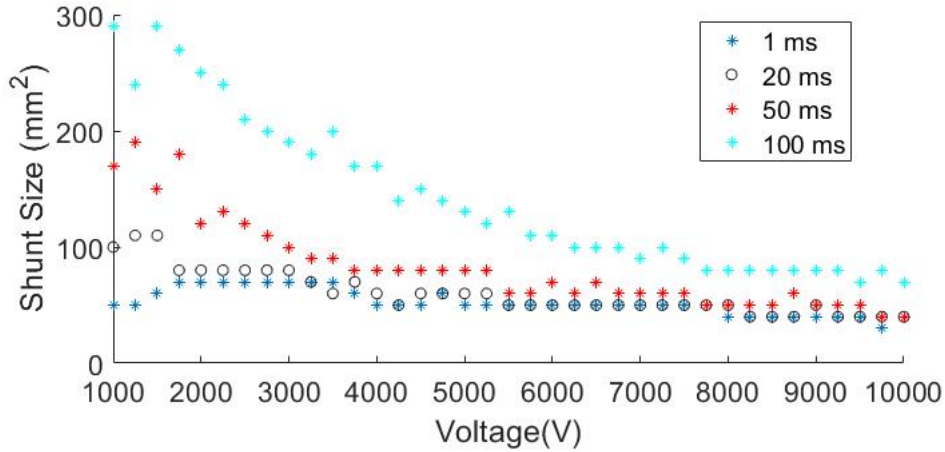
Figure 5.14: Conventional shunt CSA selected by the PSO algorithm for each voltage level and ride-through time requirement.

and fast interruption times where there is less contribution from steady state fault current. As shown on Figure 5.15, longer interruption times shift the peak post-fault temperature of the cable selected up, with the optimisation algorithm converging on solutions that use more superconducting material to offset the effect temperature rise has on depressing post fault critical current, Figure 5.13.

5.3.4 Sensitivity to Operating Temperature

The influence of steady state operating temperature on the superconducting cable affects the results of the PSO algorithm in multiple ways as shown by Figures 5.16, 5.17 and 5.18. The underlying impact that operating temperature has on the circuit is the critical current density of the superconducting tape (higher at lower temperatures), and the size of the energy gap between the operating temperature and the critical temperature, where superconductivity is no longer possible (also larger at a lower operating temperature). As such, increasing the normal operating temperature of the superconducting cable leads to more superconducting material being required to maintain superconductivity at the same current level.

As shown by Figures 5.16, 5.17 and 5.18, temperature is varied from the base case of 65 K to 75 K. The fault ride through requirement is set at 100 ms for all of these cases. Figure 11 shows the cost of the cable configurations found by the PSO algorithm and
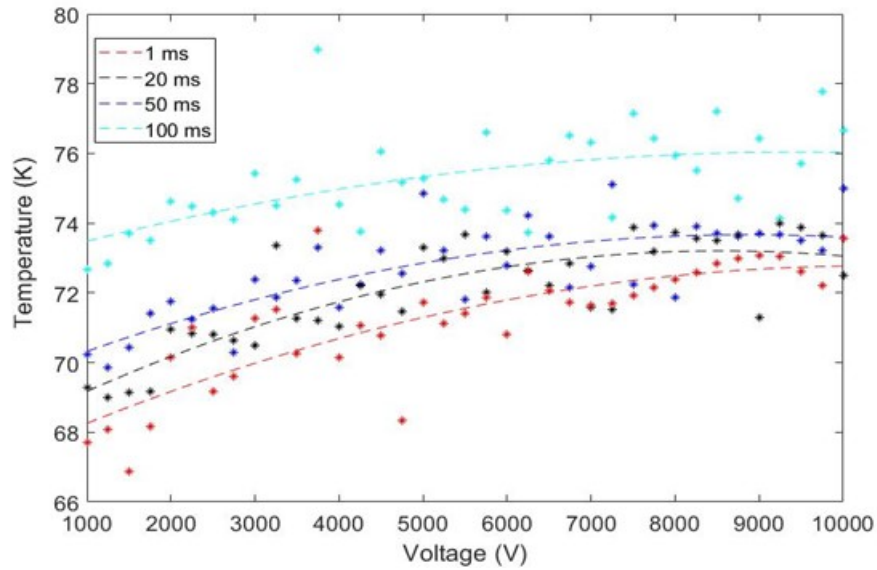
Figure 5.15: Temperature reached by optimal cable configuration selected by algorithm
for each voltage level and ride-through time requirement

it can be seen that as the operating temperature increases, the cables' cost increases
as well. This cost however does not consider any additional cooling costs required to
keep the cables at lower temperatures. Shown on the right axis of Figure 5.16 is the
shunt area size requirement which can be seen to be rising broadly in proportion to the
cost of the cable configuration, indicating its more beneficial on a lifetime cost basis at
higher temperatures for the cable to be able to absorb greater fault energy rather than
increase the amount of superconducting tape.

In contrast, the amount of superconducting tape in the selected cable configuration
decreases, in general, as the operating temperature increases and this is exemplified on
Figure 5.17 which shows the critical current for each operating temperature, normal-
ized to 77 K. This indicates that as the temperature decreases it is more favorable to
reduce the amount of conventional material, and therefore the weight of the component,
and take advantage of the greater energy gap due to the larger difference between the
operating and critical temperatures. Of note in Figures 5.16 and 5.17 is the significant
outlier in this trend at 67 K. This data point is a consequence of the PSO technique,
in which the solution has found a near optimal solution that utilizes a larger critical
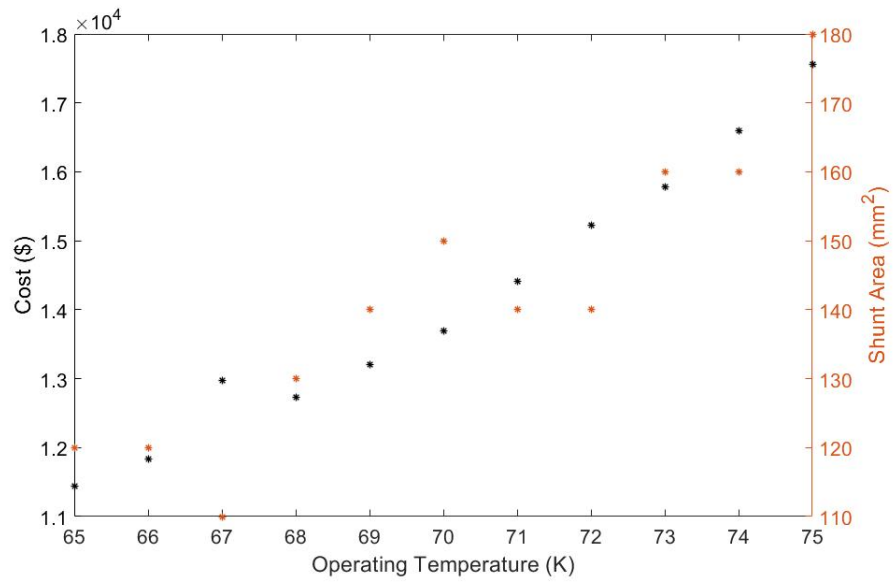
Figure 5.16: Variation in Cost and CSA of Conventional Shunt with Respect to Operating Temperature.
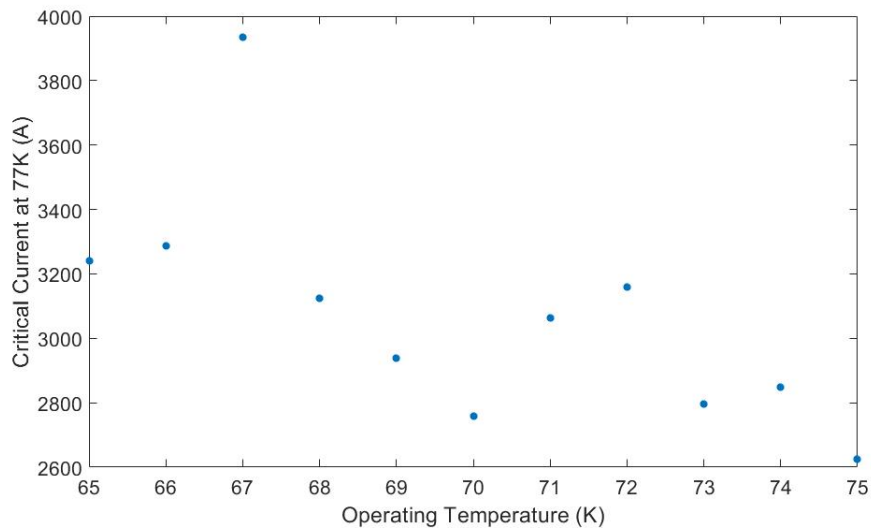
Figure 5.17: Relationship between Critical Current and Operating Temperature for optimised Cable Configuration
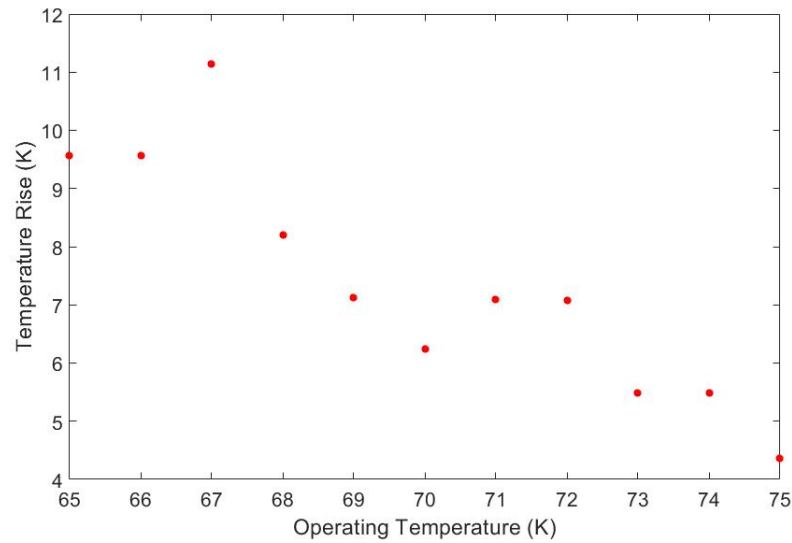
Figure 5.18: Temperature Rise in Cable by Selected PSO Solution for Different Operating Temperatures.

current and small shunt area that leads to an overall cost that is clearly off trend in the data. This happens when particles get stuck in local optima in the search space. The utilisation of this energy gap is exemplified in Figure 5.18 which shows the temperature rise following ride through for each operating temperature. As shown in this figure, a greater temperature rise is evident at lower operating temperatures, and this is primarily due to the lower heat capacity of the cable configuration selected. As well as the greater energy gap, the critical current density is greater at lower temperatures meaning that each additional Ampere of critical current is effectively cheaper, although this does not consider the impact of additional cooling power on overall cost.

5.4 Chapter Summary

TeDP presents an opportunity to reduce fuel burn through novel propulsion system architectures and the application of superconducting materials to electrical components. To maximise this, components must be optimised with respect to capital costs and operating costs incurred by the upfront price of new technologies and the expected implications for fuel burn of the component mass.

Chapter 5. Sizing of Superconducting TeDP Cables Using a Particle Swarm
Optimisation Approach

This chapter has presented and applied a novel optimisation methodology for superconducting cables to minimise lifetime cost which allows for a wide variety of system thermal and electrical parameters to be considered while ensuring protection requirements, specifically ride-through capacity and interruption speed, are adhered to. To do this a new algorithm was presented that considered the intimate relationship between temperature and critical current of superconducting components. As such, the algorithm implemented in this chapter used the MRC and MRT operation limits previously defined in Chapter 4 as a basis for protection ride-through requirements.

From observation and analysis, it is found that the algorithm is able to successfully identify optimal solutions within the search space using a PSO based optimisation method, and that system variables have a significant impact on the final cable design selected by the method. Faster operating times are found to significantly reduce the cost of the cables at all voltage levels considered in sensitivity studies, making fast acting solid state circuit breaker technology a key enabler for reducing the cost of superconducting cables for TeDP aircraft. Additionally, lower cable operating temperatures allow for large reductions in cable material usage, although this has to be balanced against greater cooling requirements, the cost of which is not captured in this chapter but may be an optimisation variable of interest in future work.

Whereas this chapter applied the method to a cable within a system containing a single generation source, load, and fault location, Future implementations of this method will also aim to apply it to more complex network architectures. This could consider systems that contain multiple protection system operating points, such as in zonal protection systems, as well as multiple generation sources that may allow for greater recovery margins and reduced operation modes in cables that have had to withstand temperature rise due to an electrical fault, such as the system presented in Chapter 6. As well, comparing the computation time of using PSO as the optimisation technique as opposed to other potentially suitable techniques will allow determination of the most appropriate optimisation methods for this type of sizing problem.

Chapter 6

Voltage Based Current Compensation Converter Control

DC TeDP architectures such as the one shown on Figure 6.1 have a significant amount of power electronic interfaces. One area that is lacking in fundamental research is exploring how new control strategies can take advantage of these network resources to improve component availability following abnormal conditions such as electrical faults and cooling system failures that lead to temperature rise of superconducting components.

As described in earlier chapters, superconducting components are inherently sensitive to temperature change, with even a small increase in temperature significantly depressing the critical current of a superconductor. If the temperature rise is significant enough, the MRC can be reduced below full load current. To ensure thermal stability it is required that operating current be reduced below MRC in the affected component to prevent potential damage and reduce recovery times.

The authors of [130]show the use of a reduced power operation mode based on the current capacity of conventional materials in the component above T_C. This allows for much lower power to be delivered using only the conventional current carrying capacity of the non superconducting materials within the components design. However, unless the component has exceeded T_C, this ignores the potentially significant power capacity still available to carry current, albeit at a reduced level [130] within the superconducting
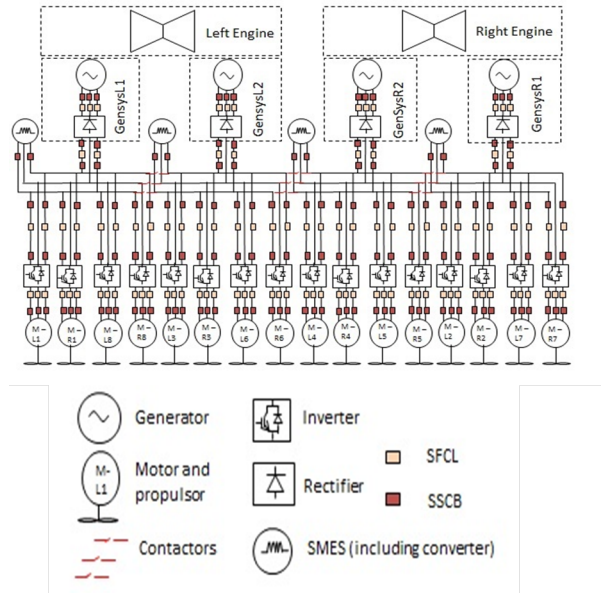
Figure 6.1: Illustration of proposed sTeDP Architecture [28]

parts of the component.

This additional capacity could be used to transmit reduced current to BLI fans to minimise drag penalties as well as reduce the amount of power that energy storage or backup generators may have to supply through redundant feeders. This has the potential benefit of reducing energy storage depletion and maximising stability margins in healthy feeders. Being able to tap into this additional current capacity could also be critical in an emergency scenario. As well, by allowing cables to provide reduced power following a fault as opposed to the maximum, cables can be designed to be smaller, saving weight and fuel, as demonstrated in Chapter 5.

The authors of [131] show how capability curves can be produced for superconducting components. These curves attempt to define the relationship between fault ride-through energy dissipation and the superconducting component's thermal stability [131]. This allows for a relationship to be built between the component experiencing over-current and the amount of time that particular current level can be withstood before normal steady state current will lead to thermal runaway. The inability to meet required steady state currents could be an isolation criterion for a conventional, terrestrial system. TeDP however, with arrays of multiple fans that have large operating

135

reserve during cruise can provide for high levels of redundancy and control options [132]. One of these is using converter interfaces to limit and manage current in branches which have undergone temperature rise.

Limiting current in a particular branch through the use of power electronics can be achieved through appropriate converter control [133]. This can give system planners a great deal of design freedom that can be used to help prevent abnormal conditions from affecting flight. The ability to limit current using converters will be dependent on the architecture of the distribution system as well as the capability of the power electronic module. In particular, the load types used in the system could play an important role in ensuring system stability [134]. For instance the influence of constant power and constant impedance loads will be investigated in this chapter to determine their influence on network stability and thermal runaway during implementation of a current limitation control method.

In this area there is a significant amount of existing literature on DC micro-grids which is directly applicable to a TeDP system with respect to control and system stability. For instance the authors of [135] examine the impact of parallel sources on the stability and reliability of a more-electric aircraft (MEA) DC aircraft bus with CP loads, concluding that energy storage is essential to improve these attributes. Coordinating load sharing between multiple sources in a DC-microgrid can be done through droop control [136]. While this type of control has been applied to MEA concepts such as in [135] and [137], the application of load sharing techniques is not well explored with respect to superconducting systems and the additional constraints introduced by the use of these materials. For instance, no literature explores the application of these techniques resulting from a superconducting cable requiring current limitation due to operating at higher than normal temperatures.

As well as load sharing strategies to reduce the current carried by a superconducting cable, power management and load shedding strategies can be adopted to reduce the power consumed by specific loads and reconfigure the network to deliver power through alternative paths as proposed by [138]. Within conventional MEA, load management strategies are reviewed by [139] where specific strategies suggested involve exploiting

loads with large time constants such as galley ovens, and exploiting the cyclical nature of certain loads such as wing ice protection [140]. However owing to the power levels of electrical propulsion for large commercial transport, such methods may not remove enough demand on the electrical power system to reduce current below MRC and a combination of network reconfiguration and curtailment of propulsion loads may be required.

To limit current effectively while ensuring appropriate safety margins are kept, the temperature of the superconducting component must be known. Thermal measurements can be used for this however the response time of the measurements can vary significantly depending on the sensor used and the application itself [141]. These response times may be too large to limit current before thermal runaway takes place. An alternative approach is to estimate the temperature of the component through electrical measurements. This chapter presents a method that uses the IV-characteristic of the superconducting transition to determine the temperature of the component in real time and adjust current to a suitable level.

To this end, this chapter will describe a converter control algorithm, implemented on the DC rectifiers connecting the generators to the distribution system, that is designed to maximise power distribution within a superconducting distribution network during periods of temperature greater than T_0 and below T_C. This is done in line with the MRT and MRC as described in chapter 4, to maximise power delivery while preventing thermal runaway.

This chapter is structured as follows. Section 6.1 discusses the aims and implementation of this scheme to a controlled three phase rectifier. Section 6.2 describes the system architecture that the control scheme is applied to. Section 6.3 describes the results obtained from modelling and simulations of the control scheme as applied to the architecture described in Section 6.2. Section 6.4 discusses the limitations of this control scheme and Section 6.5 concludes this chapter, providing a summary of the key findings.

6.1 Aims of Converter Control Scheme

The control scheme proposed in this section aims to maximise the amount of power that can be transmitted on a converter interfaced, superconducting, distribution line that is forced to operate at greater than nominal temperature but below T_C. To do this, the temperature of the cable needs to be determined to ensure that operating current is curtailed to a level below MRC as this prevents losses from overwhelming the cooling system. This is achieved using a model based controller that uses knowledge of the components voltage response at different operating currents and temperatures. This way, temperature is estimated using the components electrical response. As such, the method is named voltage-based current compensation converter control (V4C).

The voltage drop along a superconducting cable due to an input current is strongly temperature dependent as seen in (3.8), (3.9), and (3.10). By determining the current flow in superconducting material for a given shunt impedance, a surface that represents the relationship between voltage drop along the cable, operating current, and temperature is created as shown by the 3D surface plot in Figure 6.2. The relationships between input current I, voltage drop V, and cable temperature T, allows for an estimate of the latter based on voltage and current measurements. Assuming the cooling system is active, the maximum current limit, the MRC, is then calculated by (4.16).

With a safe operating current below the MRC selected, a power electronics module with suitable current control can then regulate the amount of current transmitted in the distribution line to this value. As the current is below the MRC, this allows temperatures to return to nominal operating conditions while ensuring partial load fulfilment during the period of higher temperature. In addition, if the temperature rise is a result of cooling system failure, current reduction could increase the amount of time that supply is available by minimising further heating caused by flux flow losses.

In practice a look-up table could be used to quickly ascertain this temperature based on the components voltage response at a given current input temperature. This provides a fast and simple procedure for estimating the temperature based on electrical magnitudes which can then be used to to limit current in a converter control scheme as
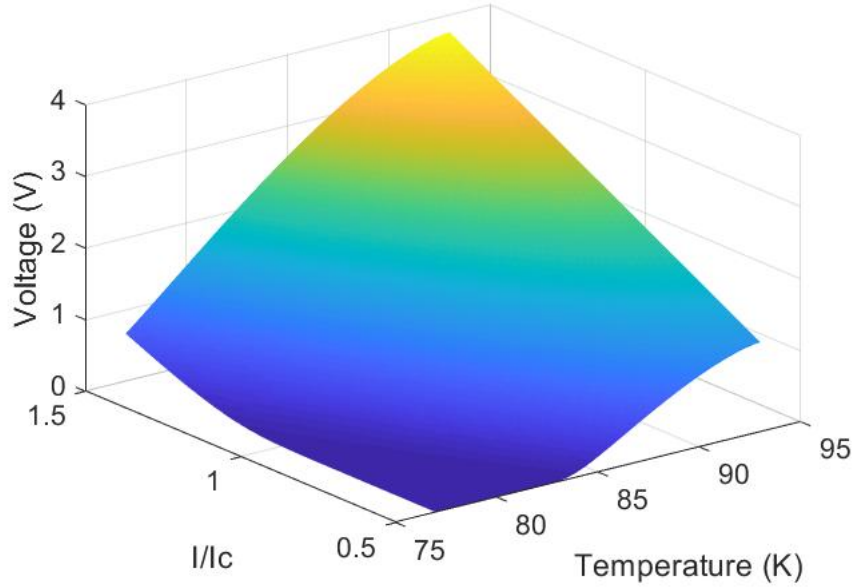
Figure 6.2: Surface of Voltage Drop With Respect to Temperature and Current of a Superconducting Distribution Cable

will be shown in the following sections of this chapter. Alternatively, the temperature can also be obtained using (6.1), which is derived by substituting 3.9 into 3.8 and rearranging for T.

$$T = T_c - \left(\left(\frac{\left(\left(\frac{E_c^{1/n} L^{1/n}}{V_{sc}(t)^{1/n}} \right) I_{sc}(t) \right)^{1/n}}{I_{cref}^{1/n}} \right) (T_c - T_{ref}) \right) \tag{6.1}$$

Where T is the temperature of the component, T_C is the critical temperature, and T_{ref} is the reference temperature of the critical current, all in units of K. E_C is the quench constant of 1e^6 V/cm. I_{sc} is the instantaneous current transported by the superconductor, I_{cref} is the reference critical current at the T_{ref}, in A. V_{sc} is the voltage drop measured across the superconductor. n is transition index.

6.1.1 Control Scheme Implementation

The current limitation algorithm is implemented through the use of a feed-forward controller within a power electronic control system. The feed-forward controller is designed

139

to saturate the current request of a *dq*-controlled voltage source rectifier or inverter in order to prevent thermal runaway during above nominal temperature conditions. A *dq* control system was chosen for this study as it simplifies the control of voltage and current by reducing the number of controlled variables to two DC values, instead of having to regulate each phase current.

The control scheme operates in accordance with two priorities. During normal operating conditions the system behaves as a normal voltage source controlled rectifier and the primary objective of the control system is to maintain the voltage across a DC-link capacitor at its reference value. The second priority of the control loop ensures that the operating current does not exceed MRC. This is achieved using a feed forward control that looks at the voltage drop along, and current carried, by the cable and determines the present operating temperature using the approach described in the previous section. Once cable temperature is determined, the MRC is calculated and action is taken to limit the current to a value below this. The following subsections describe the distribution network model and the control scheme set-up.

Overall Circuit Model

To present this concept the network shown on Figure 6.3 is considered for modelling and simulation. This model contains a single generator and motor channel taken from the overall TeDP network (Figure 6.1) with an energy storage source connected to the common bus through a DC/DC converter. This electrical architecture consists of a three-phase generator that is supplying electrical power to the distribution system, which includes a single propulsion motor load. The two electrical machines interface to a DC distribution network via power electronic converters. The distribution network consists of a superconducting cable and a DC filter capacitor that reduces voltage ripple at the output of the active, six-switch rectifier which interfaces the generator to the network. A low impedance fault is located downstream of the superconducting cable as indicated on Figure 6.3 which will be used to demonstrate a heat generating event that requires cable current limitation to prevent thermal runaway following fault clearance. This architecture does not include an superconducting fault current limiter (SFCL),
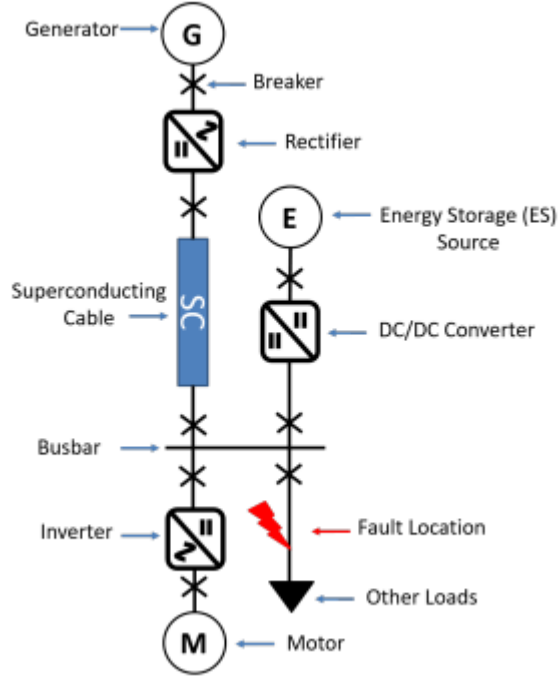
Figure 6.3: System For Modelling

this is to ensure that the cable's temperature rises during the fault. All modelling was carried out within Mathworks' MATLAB Simulink software package. Key model parameters are provided in Table 6.1, which is itself contained in Section 6.2.

DQ VSC Rectifier Control

This section describes the control of the power electronic interfaces of the system shown in Figure 6.3. The approach taken to modelling of the system's three-phase generator and rectifier is done in accordance with [142]. However, component non-idealities and parasitics have been ignored as their impact on the system response for the studies in this section are negligible. The filter capacitor, C_f, is sized in accordance with [127] using:

$$C_f = \frac{S_{nom}}{V_{dc}(\frac{6}{0.0524 f_s})} \tag{6.2}$$

Where S_{nom} is the rated apparent power of the rectifier (1 MW), V_{dc} is the rated
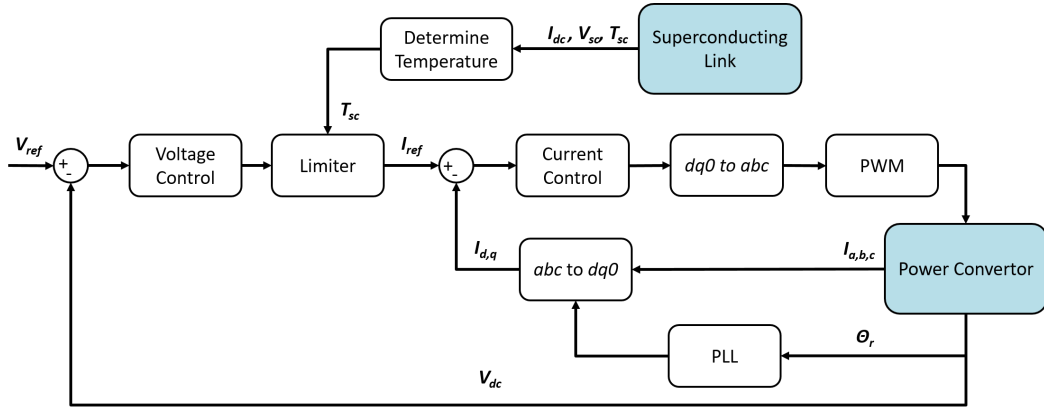
Figure 6.4: V4C Control Implemented as Feed-Forward Loop within a dq-Controlled Rectifier

output voltage (1 kV), and f_s is the switching frequency in Hz. The generator that feeds into the rectifier is modelled in Simulink as a constant three-phase voltage source. The rated output power of the generator is set as 1 MW with a rated voltage, V_{nom}, of 614.87 V AC, operating at nominal frequency, f_{nom}, is 50 Hz. The rated current of the generator, I_{nom}, is approximately 2 kA AC and the impedance of the generator, Z_{nom} in units of Ω, is calculated using:

$$Z_{nom} = \frac{V_{nom}}{I_{nom}} \tag{6.3}$$

It is assumed that the inductive portion of impedance is so large relative to the resistance that the inductance, L_{nom} (H), of the generator circuit can be calculated according to:

$$L_{nom} = \frac{Z_{nom}}{2\pi f_{nom}} \tag{6.4}$$

The control of the rectifier is described in Figure 6.4. As shown in this Figure, the rectifier uses a direct-quadrature (dq) control scheme designed to regulate the output DC voltage and current to a given reference value. A phase locked loop (PLL) is used to determine the rotor position, ωt, of the generator for use in the $dq0$ transform (6.5). This transform equation is applied to the three phase currents of the generator and
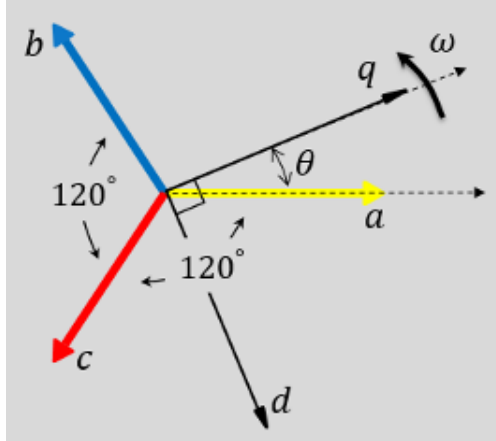
Figure 6.5: Illustration of dq Transform of abc Signals to Rotating Reference frame [143]

allows for the currents to be expressed in the rotating, dq reference frame as opposed to the abc reference frame as shown by Figure 6.5.

$$
\begin{bmatrix} i_d \\ i_q \\ i_0 \end{bmatrix} = \frac{2}{3} \begin{bmatrix} \cos(\omega t) & \cos(\omega t - \frac{2\pi}{3}) & \cos(\omega t \frac{2\pi}{3}) \\ -\sin(\omega t) & -\sin(\omega t - \frac{2\pi}{3}) & -\sin(\omega t + \frac{2\pi}{3}) \\ \frac{1}{2} & \frac{1}{2} & \frac{1}{2} \end{bmatrix} \begin{bmatrix} i_a \\ i_b \\ i_c \end{bmatrix} \tag{6.5}
$$

The voltage reference is nominally maintained at 1 pu, which corresponds to the rated voltage of the DC-link. This value is compared to the actual voltage across the DC-link capacitor and the error signal is amplified using a PI controller as shown on Figure 6.6 which presents the Simulink modelling diagram of the voltage controller. To prevent integral wind-up, a condition which can cause the integral controller to tend to infinity when the system is unable to remove the error, the integral controller is saturated to 120% I_{nom}, the nominal current of the DC-link. The output of the voltage control loop provides the reference current signal, I_d^*, for the current controller. The proportional and integral gains for the voltage controller, k_{pv} and K_{iv}, are set in accordance with (6.6) and (6.7) respectively [144].

$$
K_p = \frac{C_f}{aT_{eu}} \tag{6.6}
$$

Where a is a constant, 2.4, and T_{eu} is $4T_s$. T_s is the sampling frequency of the
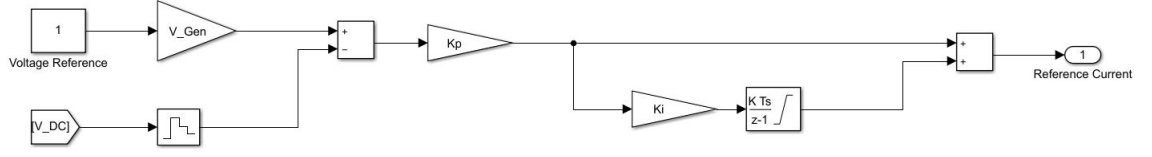
Figure 6.6: Outer voltage control loop with PI controller.

control system.

$$K_i = \frac{1}{a^2 T_{eu}} \tag{6.7}$$

The current controllers are designed to control the direct and quadrature currents which respectively correspond to the real and reactive power output of the rectifier. Hence the quadrature component (I_q) is controlled to be zero. The direct current, (I_d), changes with respect to reference requests from the voltage control loop. It is assumed that the three phase system is balanced and that the zero component is a constant at 0. To implement the current controller a PI controller is used. The proportional and integral gains, K_{pi} and K_{ii} are set in accordance with (6.8) and (6.9) [144] respectively and integral saturation is included to prevent wind-up. The dq transform of circuit equations leads to the cross-coupling of the d and q axis currents which can negatively affect dynamic performance. To prevent this a feed-forward decoupling control is implemented in accordance with [145]. This control system is shown on Figure 6.7 which contains the Simulink model for the current controller.

$$K_{pi} = \frac{L_d}{2(1.5T_s)} \tag{6.8}$$

$$K_{ii} = \frac{1}{\left(\frac{L_d}{R_{nom}}\right)} \tag{6.9}$$

Where R_{nom} is the resistance of the generator, L_d is the direct inductance of the generator.
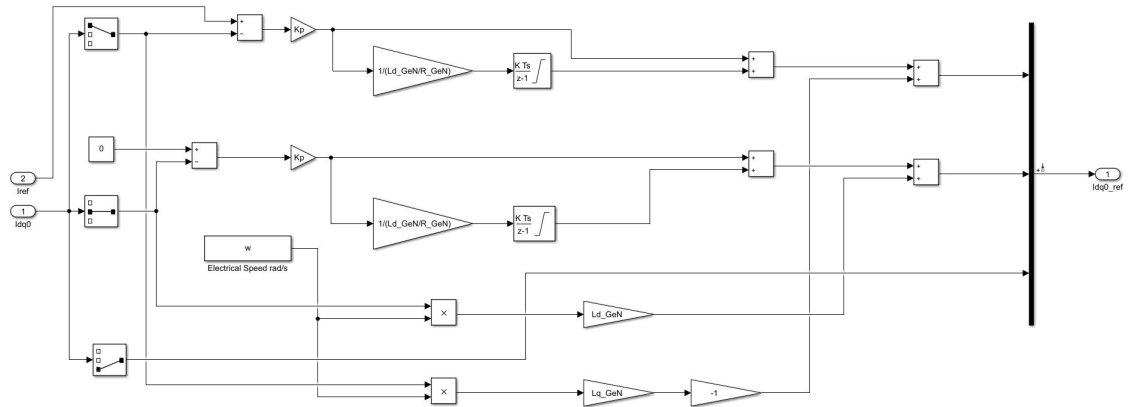
Figure 6.7: Implementation of inner current control loop with decoupling dq currents
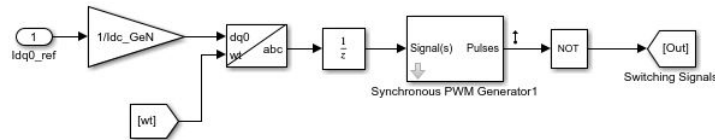
Figure 6.8: Implementation of SPWM in Simulink

SPWM

An inverse $dq0$ transform (6.10) is applied to the current controller outputs and passed to a modulator which implements sinusoidal pulse width modulation (SPWM) for controlling the rectifier switches. This is implemented in Simulink using the the SPWM block as shown in Figure 6.8 which shows the modelling diagram within the Simulink Workspace. This block takes in modulation index request for each phase and the current rotor position to determine the firing of the rectifier switches to achieve the desired current output.

$$\begin{bmatrix} i_a \\ i_b \\ i_c \end{bmatrix} = \frac{2}{3} \begin{bmatrix} \sin(\omega t) & \cos(\omega t) & 1 \\ \sin(\omega t - \frac{2\pi}{3}) & \cos(\omega t - \frac{2\pi}{3}) & 1 \\ \sin(\omega t + \frac{2\pi}{3}) & \cos(\omega t + \frac{2\pi}{3}) & 1 \end{bmatrix} \begin{bmatrix} i_d \\ i_q \\ i_0 \end{bmatrix} \tag{6.10}$$

145

Feed Forward Compensation Control

The feed forward compensation control implemented is a model based control method. This method requires the measured resistive voltage drop across the superconducting cable and the current output of the 3 phase rectifier. The temperature of the superconducting cable is then estimated in accordance with (6.1). Following temperature determination, the MRC is calculated (4.17). The current request from the voltage control loop is then saturated to a value lower than this in accordance with (6.11).

$$I_{max} = kI_{MRC}(T) \tag{6.11}$$

Where k is less than or equal to 1 and can be adjusted to provide a suitable current margin for the cable and allow for cooling system to remove energy and reduce temperature. To prevent integral wind-up occurring within the voltage control loop, the saturation limits of the integral component of the PI controller are set to be the maximum normal operating point of the superconducting cable. This ensures that when temperatures return to their normal operating conditions, that the voltage control loop is able to quickly resume control.

6.2 Baseline System Architecture Modelling

6.2.1 Superconducting DC cable Model

The superconducting DC cable used in this model consists of a thermal-electric cable model that includes a conduction layer made up of YBCO and a conventional shunt, in this case copper. The conduction layer is wound around a layer of insulation separating it from the former. Another layer of insulation separates the conduction layer from the shield. The shield is assumed to be identical in its electrical characteristics to the conduction layer. The cable design is demonstrated in Figure 6.9 which shows the different layers within the cable. Modelling of the cable is done in accordance with the current-iterative algorithm demonstrated in Chapter 3, taking into account current sharing between the superconducting layer, the conventional Stabiliser, and

146
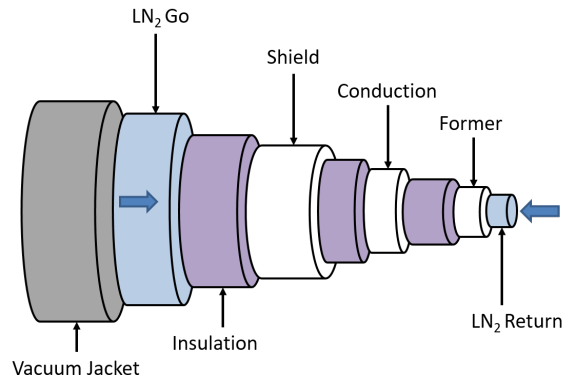
Figure 6.9: Illustration of Cable's Physical Description
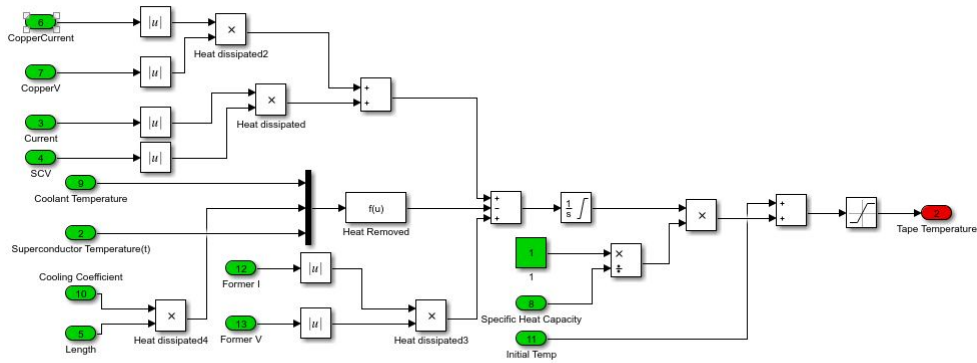
Figure 6.10: Implementation of Cable temperature model in Simulink

cable former. This diagram does not show the cable return path which is present in another cryostat.

The temperature of the cable is calculated in accordance with (6.12) where c_v represents the volumetric heat capacity of the cable in J/m^3, while the initial temperature is given by T_0. The implementation of the thermal model in Simulink is shown in Figure 6.10.

$$T(t) = T_0 + \frac{1}{c_v} \int_0^t Q_{in}(t) - Q_{out}(t) \;\; dt \tag{6.12}$$

147

6.2.2   Back-up Energy Modelling and Control

Droop Control Scheme

The backup energy source can be any storage source such as a battery, SMES, or a normally open point that feeds power from secondary electrical generators following network reconfiguration. Within the model it is represented as a controlled current source input with operating current being determined through DC droop control [146]. This allows for effective power sharing between multiple generation source without the need for communication. The energy source only discharges once voltage drops below 0.94 pu to prevent discharge during normal voltage variations, in accordance with terrestrial standards for voltage limits in the UK. The droop characteristic is based on:

$$P_{es}^* = (V_{ref} - V_{dc})k_{es} \tag{6.13}$$

Where P_{es}^* is the generated power reference in W, V_{ref} is the reference voltage, V_{dc} is the measured voltage, and k_{es} is the droop gain. This is implemented into a control scheme in Simulink which produces a power request for the backup energy storage. The power request is compared to the nominal, rated power, of the energy storage device and the amount of current required is calculated based on the power request and the present DC-link voltage as shown in Figure 6.11. This current is then fed to the distribution network using a controlled current source.

The speed at which the back-up power source can respond to a power request is limited by bandwidth of its controller. This bandwidth is set as an order of magnitude slower than the bandwidth of the 3-phase rectifier using a low-pass filter with a bandwidth of 1 kHz at the control signal input. This ensures the ES will only transfer energy into the system in response to voltage deviations when the superconducting link is unable to meet the demand during abnormally high-temperature conditions. Additionally the maximum power output of the back-up energy source is arbitrarily assumed to be 30% of the full load requirements of the motor.
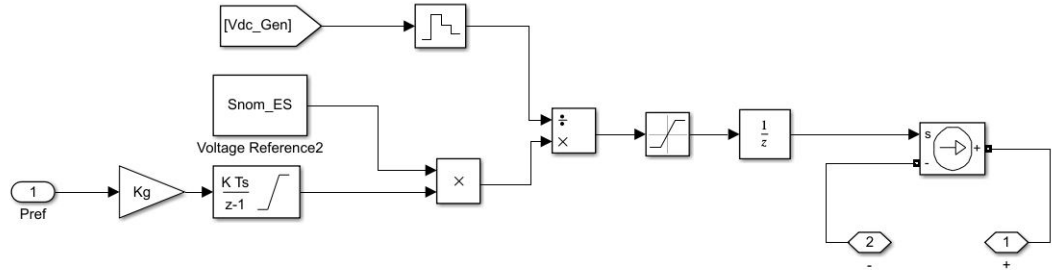
Figure 6.11: The power request from the droop control scheme uses a controlled current source to interface with the electrical system in Simulink.

6.3   Results of Control Scheme Implementation

To investigate the effectiveness of the proposed control method, with respect to different load types and system architectures, multiple scenarios are considered. Two network architectures are investigated: a system containing a backup power source, Figure 6.3, and a network in which the backup energy source is not present. How the presence of additional power supplies can affect the ability to implement the proposed control scheme, and the impact on the stability of the network following current reduction, is discussed.

The types of load considered for these two network architectures are constant power (CP), where the motor's power controller will attempt to maintain a constant power to the load by varying the impedance seen by the network, and constant impedance (CI), in which the motor will draw current in proportion to network voltage conditions. These two load types are chosen due to their differing response to the system voltage conditions. Due to the nature of these load types it is expected that any control algorithm that limits current could have a subsequent impact on system voltage stability. This needs to be investigated to determine the limits of the V4C method in networks with these load types. As well as these scenarios, the implementation of the V4C controller within the motor's inverter control scheme is also investigated. This scenario presents the case in which a power management system is able to implement

149

Table 6.1: Simulation Parameters

Parameter	Unit(s)	Value
Cable Operating temperature	K	77
Critical Temperature	K	93
Critical Current	A	1200
Rated DC Voltage	V	1000
Cable Length	m	100
Conventional Resistance	Ω	0.0025
Rated AC Voltage	V	684
AC Frequency	Hz	50
DC Link Capacitance	mF	3.45
Load R	Ω	1
Load L	mH	1
Cooling coefficient	W/mK	0.2
Rated Power	MW	1

load shedding to preserve the thermal stability of the superconducting network.

The component values for the Matlab network simulation are shown in Table 6.1. The superconducting cable is modelled in accordance with Chapter 3 for the parameters specified in Table 6.1. This model is used to populate a lookup table which describes the voltage response of a superconducting cable over wide range of current and temperatures values. This is used to determine the operating temperature throughout the course of the simulation. For these simulations a fault current of 10kA DC is used in order to cause significant temperature rise in the superconducting cable. The fault is removed from the system after 150ms to simulate the opening of mechanical circuit breakers. The fault current is implemented using a controlled current source within the Simulink software package.

The temperature rise due to the fault causes the critical current of the material to decrease. This leads to a voltage being generated across the superconducting cable and Ohmic losses occurring even after current returns to normal operating levels. In this condition, the feed-forward control loop will estimate the new operating temperature in accordance with Figure 6.2 and a new safe maximum current is chosen to prevent thermal runaway of the cable. To implement this control action, the current request,
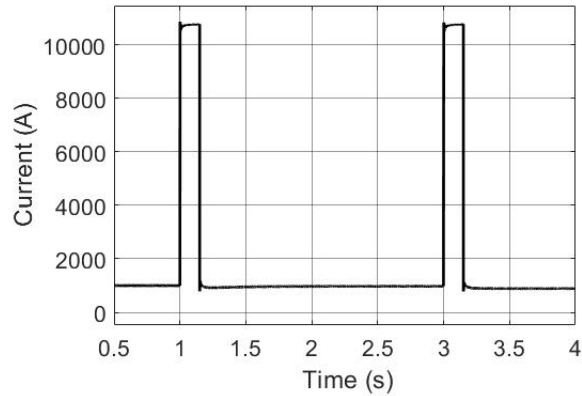
Figure 6.12: $10kA$ Fault Current Implemented on Network Using Controlled-Current Source Downstream of Distribution Cable and Subsequently Cleared After $150ms$.

I_d^*, created by the voltage controller, is saturated to ensure this maximum current level is not exceeded.

Two faults are applied during the course of the simulation, occurring at 1 and 3 seconds into the simulation as shown on Figure 6.12. This emulates the situation in which multiple faults occur within the system in succession, although these fault profiles are no representative on an actual occurrence which would include the capacitive discharge and significant voltage and current transients. The results demonstrate that the V4C controller will not take action during the first fault, because current limitation is not required to preserve thermal stability but will act after a subsequent fault that leads to temperature rise above the MRT, at which point the superconductor can no longer supply the requested current without thermal runaway taking place.

Figures 6.13 and 6.14 show the filter capacitor voltage and DC current profiles for scenarios in which a CI load is being fed by the system. These figures show the impact of current limitation taking place at the rectifier for architectures with and without ES. Figures 6.15 and 6.16 show the filter capacitor voltage and DC current profile for scenarios in which the CI load has been replaced with a CP load. Figures 6.17 and 6.18 show the filter capacitor voltage and DC current profile for the scenario in which V4C control is implemented within the inverter control loop in order to show how the placement of the controller can affect network stability.

Figure 6.19 shows the temperature of the superconducting cable for each scenario.

Figure 6.19 has been extended over a period of 10s to show whether thermal runaway or thermal recovery takes place after each fault scenario is implemented with the V4C controller in use.

6.3.1 Constant Impedance Loads

In the case of CI loads, reducing upstream current output requires a reduction in system voltage unless the network is able to provide power from an alternative source. This is due to the energy imbalance between the power requested by the load and power delivered by the generator. This can be seen in Figures 6.13 and 6.14 which show that an alternative power source will be required to ensure network voltage does not drop below required limits while providing a full range of current limitation. Without this alternative source, the maximum current limitation will be determined by the under-voltage limit of the network. Hence, the minimum current the converter can supply, determined by network minimum voltage limits, may not be sufficient to reduce current below MRC. This can be seen on the black dashed line in Figure 6.15, where the temperature rise continues following current reduction as the rectifier is incapable of reducing current enough to prevent thermal runaway, as shown on Figure 6.14. With the ES to support network voltage however, the superconducting feeder is able to supply a portion of the current, Figure 6.14, while temperatures stabilize, Figure 6.15. In this case the maximum amount of current limitation that can be applied is dependent on the maximum amount of power that the ES can supply. In this case the maximum amount of power the ES can supply is set at 30% of full load. If current must be limited to the extent at which the energy source must supply greater than this amount, then network voltage will begin to decrease which can lead to under-voltage protection tripping.

6.3.2 Constant Power Loads

Within a DC TeDP distribution network the motor loads will be interfaced through inverters. If these inverters tightly regulate their loads, they can appear as CP loads which have a negative impedance characteristic. This means that any attempt to reduce current will cause the DC network voltage to decrease, Figure 6.16, and consequently
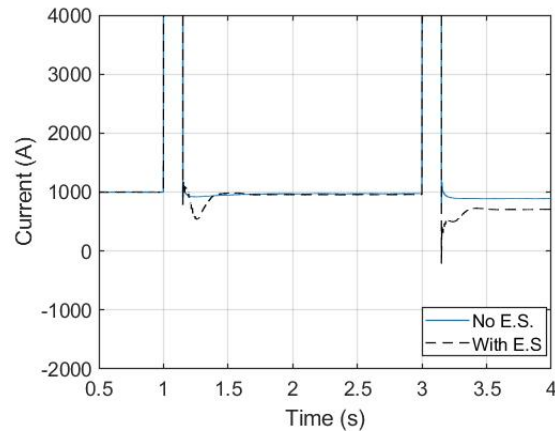
Figure 6.13: Current Profile for V4C Control Implemented on a dq-Controlled Rectifier with a Constant Impedance Load with and without a Back-up Energy Source
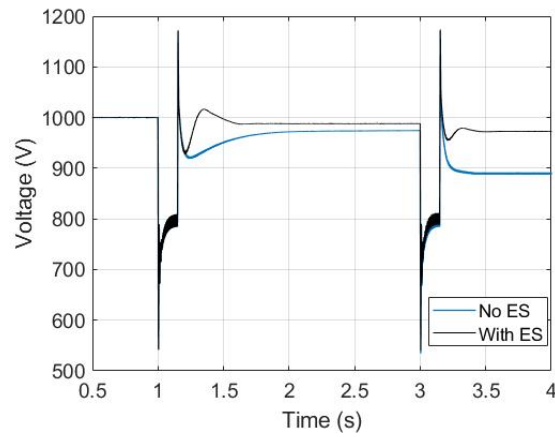
Figure 6.14: DC-Link Voltage for V4C Control Implemented on a dq-Controlled Rectifier with a Constant Impedance Load with and without a Back-up Energy Source
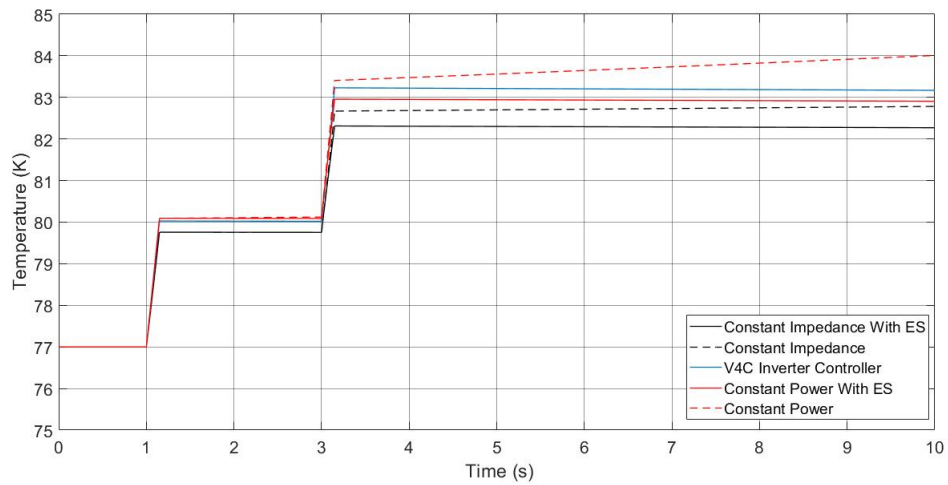
Figure 6.15: Comparing Temperature Recovery of Superconducting Cable in Different System Architectures Utilizing V4C

cause the inverter to draw more current, Figure 6.17, to maintain CP. This causes a further depression of system voltage, potentially leading to quicker thermal runaway due to the larger current drawn. This can be seen in Figure 6.15, dashed red line, in which thermal runaway takes place quicker than other scenarios due to the greater current request from CP load, Figure 6.16.

This potentially damaging issue can be resolved if the network contains a sufficient energy storage source, downstream of the affected feeder, that is able to provide the power required to prevent significant voltage deviations. This allows the feeder to supply partial power while temperatures return to normal. Alternatively, the network can be reconfigured to provide power from a different generator feeder. This scenario is shown in the blue lines in Figures 6.16 and 6.17, where the application of a droop controlled energy storage source is able to ensure that the DC network voltage is maintained. This allows full power to be delivered to the motor while ensuring the network's thermal and voltage stability is maintained.

6.3.3 Control Algorithm Embedded within Motor Controller

An alternative solution is the placement of the feed-forward limiting block within the inverter connected to the propulsion motors such that the component reduces its current
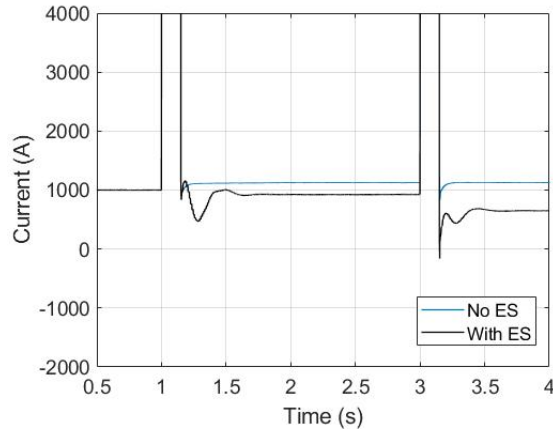
Figure 6.16: Current Profile for V4C Control Implemented on a dq-Controlled Rectifier with a Constant Power Load with and without a Back-up Energy Source
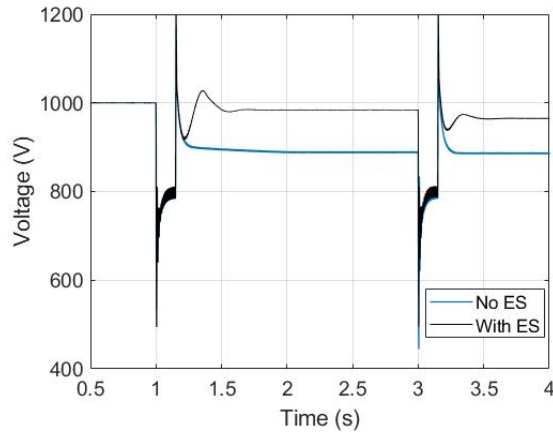
Figure 6.17: DC-Link Voltage for V4C Control Implemented on a dq-Controlled Rectifier with a Constant Power Load with and without a Back-up Energy Source
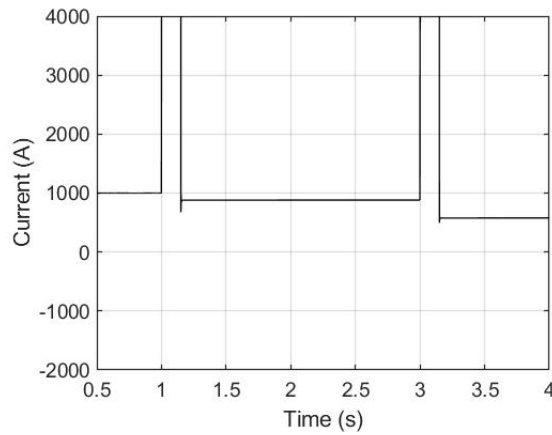
Figure 6.18: Current Profile for V4C Control Implemented on a Motor Inverter
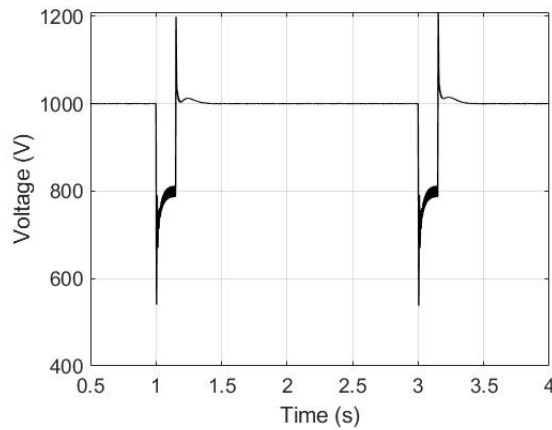
Figure 6.19: DC-Link Voltage for V4C Control Implemented on a Motor Inverter

request when it detects abnormal temperatures either upstream or within the motor, Figure 6.18. This allows for the power drawn by the motor to be reduced to ensure voltage stability within the network, Figure 6.19, while also preserving the distribution networks thermal stability, Figure 6.15. While allowing for these benefits, it would require coordination to ensure aircraft dynamics are not negatively affected by reduced thrust output of the motor. This could be exacerbated in architectures, such as the N3-X TeDP network shown in Figure 6.1, which contain large numbers of motors being fed by a single channel and would require greater coordination to ensure appropriate limitation of current and equal distribution of thrust across multiple fans.
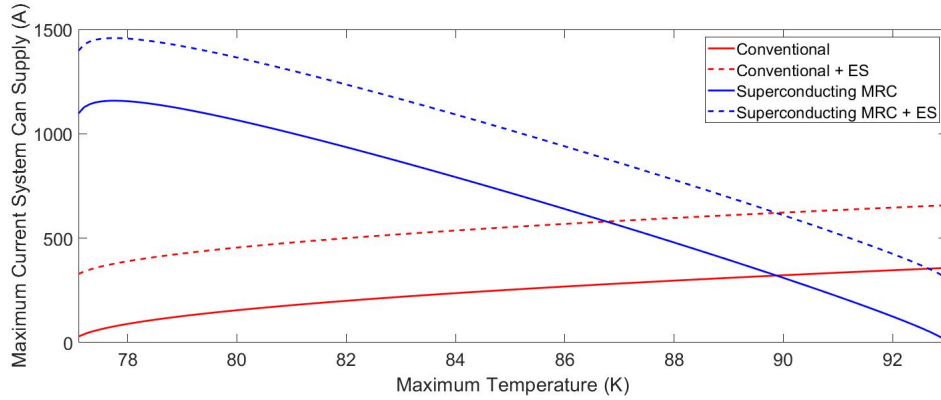
Figure 6.20: Comparison of Maximum Current the System can Supply the Motor Following a Fault Using V4C and Limiting Current to The Conventional Materials Carrying Capacity, With and Without Energy Storage,

6.3.4   Comparison Versus Conventional Conduction Only

This subsection compares the impact of a V4C approach versus a situation in which current is limited based on the maximum that can be transmitted through the conventional materials present in the superconducting cable without exceeding the cooling system's capacity. Based on the parameters shown in Table 6.1, and assuming that the temperature of the liquid nitrogen reservoir remains constant, without V4C the current would have to be limited to approximately 320 A to prevent the temperature of the cable from going into thermal runaway. This is lower than the amount of current capable of being provided by the cable using a V4C approach using MRC as a limiting factor for temperatures below T_C. Figure 6.20 visualises the comparison between the cable MRC and the maximum current level that can be transmitted based only on the conventional materials and the cooling system capacity. It can be seen that by using V4C a significantly larger amount of power can be transmitted through the cables without causing thermal runaway until T_c is reached. The limitation of current transmission through conventional materials can be increased by using larger cross-sectional areas of conventional material in the cable's design, but this will increase weight, which is a key design variable in aircraft systems. This greater current restriction also increases the amount of power that needs to be supplied by additional sources such as ES, further driving up system mass.

6.4 Control Scheme Limitations

In order for the control scheme to function correctly key requirements must be met. Firstly, the model based controller used to provide the current limiting signal must be an accurate representation of the superconducting component. If it is not then the current curtailment may not be significant enough to ensure that thermal runaway does not take place. Alternatively, the current curtailment could be too vigorous and negate any potential benefits that using this method of control can have.

To develop model based controllers that are able to accurately predict the components voltage response to a current input over a range of operating temperatures, testing would need to be undertaken by manufacturers using specialized equipment to control the environment that the component is operating in. This could lead to increased costs to develop the controller and make other approaches to improving system availability more economical.

Another consideration is the inhomogeneity of superconducting critical current throughout the component. As seen in Chapter 4, this can cause large variations in critical current throughout the length of a superconducting tape. This leads to the potential for localised thermal runaway when implementing this control approach as MRC is not equal throughout the component. The degree to which this could be a limiting factor depends on both the amount of inhomogeneity in the component, which is reducing as manufacturing improves, and the whether thermal energy can be quickly transferred to the surrounding area, reducing the potential for a hotspot. This could make the control approach less practical for superconducting components with resistive Stabilisers (FCL Cable Design) as these have poor thermal conduction properties.

Another key requirement for this control method is that it must be able to curtail current fast enough to prevent thermal runaway from occurring. The length of time in which the control needs to act will depend on the thermal capacity of the component and the amount of energy in the fault. As seen in Chapter 4, the thermal capacity for a cable is dependent primarily on the size of the Stabiliser and former, as well as the material used in its construction.

6.5   Chapter Summary

To maximise the benefits of superconducting technology in TeDP applications, new control methods are required to ensure that the unique thermal requirements of superconducting components can be accommodated without negatively impacting flight. This chapter demonstrated a novel control method aimed at using electrical signals to determine the temperature of a superconducting component, and subsequently regulate the output current of a VSC, ensuring thermal runaway does not take place in the event of higher than normal operating temperatures.

This method is designed to maximise the capacity of the superconducting network operating in temperatures between the nominal and critical temperature of the component, maximising the amount of power that can be delivered through superconducting materials. This allows for a cable that has undergone transient heating to provide a reduced supply while operating at higher than expected temperatures. This could have the benefit of reducing the number of components isolated following a temperature rise event, thus reducing the amount of power that must be supplied by alternative sources. Additionally, this method would ensure that a reduced supply to critical components such as BLI fans can be met.

The results shown in this chapter demonstrate that the extent to which current can be limited within the superconducting network depends ultimately on the architecture of the network and the location where current limitation is implemented. Implementing current limitation upstream of the affected branch can have a significant negative effect on the stability of the system. As well, the extent of limitation capability depends on the type of loads on the network, and the architecture of the network itself. Specifically, to maintain voltage stability while providing current limitation, a backup power source will be needed to meet the demands of downstream loads and preserve the energy balance within the network. This could increase energy storage requirements or an architecture that is highly re-configurable will be needed.

Future work would include the implementation of this method within a test system to provide experimental validation of the control algorithm. This would allow determi-

nation of the required sensitivity of the electrical measurements, the speed of operation, and safety margins required to ensure suitable DC-link current limitation.

Chapter 7

Conclusion and Future Work

7.1 Thesis Summary

Commercial aviation faces challenges in the coming decades due to a combination of demand growth and increasing regulatory pressures to reduce greenhouse gas emissions. A potential solution for meeting regulatory targets while accommodating demand growth is through the use of turbo-electric distributed propulsion. This concept design would allow: greater utilization of airports by reducing runway field length requirements and aircraft noise; reduction in fuel use by increasing the effective by pass ratio of the aircraft and taking advantage of aerodynamic effects such as BLI.

However, the electrification of the propulsion system is a significant technological step change, requiring an on-board electrical power system which is rated to an order of magnitude higher than than is required by state of the art more-electric aircraft of comparable size and range (e.g. 248 pax, 13530 km for a B787-8 Dreamliner). The protection of such a compact, high-power, safety-critical, system is a complex problem that needs to addressed to bring electrical propulsion aircraft to market. To this end, this work contributed to the following research questions raised in Chapter 1:

1. What is the likely fault response of a compact superconducting DC network and how will the network and superconducting cable parameters affect this?

2. What operating margins are required to protect superconducting cables from high currents experienced fault ride-through and can this be optimised?

Chapter 7. Conclusion and Future Work

3. What options do system designers have to improve power availability after a fault that leads to temperature rise within a superconducting feeder cable?

Each chapter made contributions to these questions as summarized now. Chapter 2 explored the background of superconductivity and its application as an enabling technology for TeDP. It introduced the primary concepts for TeDP before discussing superconducting cable designs and the main failure modes of superconducting components identified in the literature thus far.

Chapter 3 approached question one in two ways: first the development and analysis of a superconducting tape model, based on literature, for use in MATLAB's Simulink environment; and second, experiments involving the discharge of a capacitor through superconducting tapes to capture the superconducting tape response to the initial moments of a converter interfaced fault. The former defined the superconducting fault circuit within the context of the response being under, over, or critically damped and the influence circuit and component parameters had on the response. Although superconducting systems are fundamentally different nature, this behaviour still shares may similarities with conventional DC systems and shows the value in encouraging read across from these two domains. The experimental work at the end of Chapter 3 also demonstrated the very large currents experienced during a filter capacitor discharge due to the minuscule damping provided by superconducting tapes with highly conductive stabilising layers, as well as the damaging potential this can have on superconducting components with resistive stabilising layers.

Chapter 4 bridged the gap between question 1 and 2 by using a component level model to understand how different cable design philosophies can affect the failure modes of a superconducting TeDP cable under fault conditions. It was discussed that at conditions near the critical current FCL based cables can be much more prone to hotspot formation and localized thermal runaway. As well, it was demonstrated that given the relatively short lengths of cable run expected on a TeDP aircraft, FCL cables are unlikely to be suitable to limiting fault current to a significant degree without an unacceptably large temperature rise that is likely to lead to degradation, as seen in the experiments of Chapter 3. Chapter 4 concludes by defining operating limits for FCT

162

cables in terms of maximum temperature rise and current capability following a fault within a TeDP system.

Chapter 5 contributes to question 2 by taking the MRC and MRT operating limits, developed from theory at the end of Chapter 4, and applies them as constraints within an optimisation framework aimed at minimising the cost of the FCT superconducting cable over the lifetime of the aircraft. It does this by taking a range of system, component, and economic inputs and shows how PSO can be applied within this framework to find a cable critical current and stabilising layer size that minimises overall cost while still obeying the protection requirement constraints. Using this method it was shown that system variables can have a large impact on overall cable design and that the protection system operating speed and superconductor operating temperature are strongly correlated with overall component cost.

Chapter 6 provides a potential solution to question 3 in form of a control strategy within a DC superconducting TeDP network using power electronic interfaces. By determining the temperature of the cable using its known Current-Voltage response, it was shown that the current could be regulated to ensure thermal runaway did not take place during higher than normal operating temperature conditions. This can allow more power to flow in such a situation than would otherwise be possible through limitation of the current to the maximum carrying capacity of the conventional materials in the cable. The chapter discussed the limitations this would have on the stability of the network and how energy storage and or redundant paths would be required for full power provision during these conditions.

In conclusion, this thesis has built a framework for improving the fault ride through capability of superconducting cables in the context of future sTeDP aircraft. Chapter 3 conducted modeling, simulation, and experimentation of superconducting tapes, providing the necessary groundwork for the optimization method introduced in Chapter 5 and the control method presented in Chapter 6. Chapter 4 complemented these efforts by establishing the thermal protection requirements of MRT and MRC for the superconducting cables. Chapters 5 and 6, the core contributions of this thesis, introduced an optimization method capable of designing FCT cables capable of withstanding

fault ride-through, alongside a control method that enables the maximization of power transmission in degraded cables. These two methods offer advantages to future sTeDP aircraft designers by providing a wider array of options when selecting the electrical protection strategy.

7.2 Future Work

A number of areas have been identified for future work throughout this thesis and will be summarized here:

1. The Simulink modelling and analysis presented in Chapter 3 aims to find the impact that system variables have on whether the response of the circuit is critically damped. However, it would be really valuable to develop an methodology which can take the system variables and automatically determine the response (over, under or critically damped) of the system. This could be beneficial in determining the size of fault current limiting components required to dampen electrical faults.

2. There is a need to expand the experimental work presented in Chapter 3 to replicate the full fault response including not only the initial discharge of the DC capacitor but also the steady state response being fed from the generators. Additionally it would be ideal if the parameters, voltage, current and power are raised to values closer to that of the TeDP Targets. This would allow a greater variety in the types of cable and tapes that could be tested within the experiment. This would provide greater insight to the damaging effects of electrical faults on superconducting components and enable refinement of protection requirements.

3. The optimisation framework currently only considers the use of the particle swarm optimisation method. The advantages of using this technique are explained in Chapter 5. However, a comparison with other optimisation methods would be useful to determine whether particle swarm optimisation provides the fastest solution.

   The particle swarm optimisation method requires a fault simulation to be exe-

cuted for each particle, the time step has a significant impact on computation speed. One improvement that could be of value would be to implement a variable time step such that early in the process accuracy is traded off for computation speed, while the opposite occurs later in the process as particles begin to converge on an area of good solutions. The impact this may have on computation speed and particles ability to find valid optimal solutions would be of interest.

4. The control method in Chapter 6 relies on the current-voltage-temperature relationship within the superconducting cable to be well known. It is not known how an inaccuracy in measurement of this relationship could affect the capability of the method to prevent thermal runaway or the impact inhomogeneity of the critical current could have in this respect. Whether the method could be modified to use a standard PI response to a voltage feedback could also be investigated as this may be a simpler approach.

Bibliography

Bibliography

[1] Airbus. Flying by numbers, 2015.

[2] Transport Environment Contributors. Aviation emissions and the paris agreement europe and icao must ensure aviation makes a fair contribution to the paris agreement's goals. 2016.

[3] Laurent Box, laurent cavadini, Gregg fleming, and Lepinay Ivan. On board a sustainable future, 2016.

[4] NASA. Nasa aeronautics strategic implementation plan 2017 update, 2017.

[5] European Union. Reducing emissions from aviation.

[6] European Union. Resolution a41-22: Consolidated statement of continuing icao policies and practices related to environmental protection-carbon offsetting and reduction scheme for international aviation (corsia).

[7] Jo Dardenne. Corsia: worst option for the climate briefing on assessment of icao's offsetting scheme. 2021.

[8] R. I. Jones. The more electric aircraft—assessing the benefits. *http://dx.doi.org/10.1243/0954410023321028775*, 216:259–269, 5 2002.

[9] A Rodríguez-Díaz, B Adenso-Díaz, and P L González-Torre. A review of the impact of noise restrictions at airports.

[10] Heathrow. Night flights — heathrow.

[11] Sandra Laville. Cleanup cost of heathrow third runway doubles to £100bn, mps told — heathrow third runway — the guardian, 2021.

Bibliography

[12] Andrew Hahn. A conceptual design of a short takeoff and landing regional jet airliner. American Institute of Aeronautics and Astronautics, 1 2010.

[13] Jake Hardiman. The history of london city airport.

[14] Patrick W. Wheeler, Jon C. Clare, Andrew Trentin, and Serhiy Bozhko. An overview of the more electrical aircraft. *http://dx.doi.org/10.1177/0954410012468538*, 227:578–585, 12 2012.

[15] Ahmed Abdel-Hafez and Ramesh K. Agarwal. *Power Generation and Distribution System for a More Electric Aircraft - A Review.* IntechOpen, 2 2012.

[16] Airbus. Getting to grips with fuel economy, 2004.

[17] Oleksandr Zaporozhets, Volodymyr Isaienko, and Kateryna Synylo. Trends on current and forecasted aircraft hybrid electric architectures and their impact on environment. *Energy (Oxford, England)*, 211:118814, 11 2020.

[18] Mike Sinnett. 787 no-bleed systems: Saving fuel and enhancing operational efficiencies. *Boeing.*

[19] Boeing. Boeing 787 from the ground up. *Boeing.*

[20] A. Belarbi, M. Dawood, and B. Acun. *Sustainability of fiber-reinforced polymers (FRPs) as a construction material*, pages 521–538. Elsevier, 2016.

[21] Dan Rutherford. Size matters for aircraft fuel efficiency. just not in the way that you think.

[22] Hd Kim. Distributed propulsion vehicles. *27th International Congress of the Aeronautical Sciences*, pages 1–11, 2010.

[23] Kiruba Sivasubramaniam Haran and Kaushik Rajashekara. High specific power machines and drives for turbo-electric aircraft - ieee transportation electrification community.

[24] Devaiah Nalianda and Riti Singh. Turbo-electric distributed propulsion - opportunities, benefits and challenges. *Aircraft Engineering and Aerospace Technology*, 86:543–549, 9 2014.

Bibliography

[25] Hyun D. Kim, Aaron T. Perry, and Phillip J. Ansell. A review of distributed electric propulsion concepts for air vehicle technology. *2018 AIAA/IEEE Electric Aircraft Technologies Symposium, EATS 2018*, 11 2018.

[26] Chengyuan Liu. Turboelectric distributed propulsion system modelling. 2010.

[27] Michael Kerho and Brian Kramer. Turboelectric distributed propulsion test bed aircraft nasa aeronautics research mission directorate (armd) fy12 learn phase i technical seminar.

[28] Catherine Jones, Patrick Norman, Stuart Galloway, Michael Armstrong, and Andrew Bollman. Comparison of candidate architectures for future distributed propulsion aircraft. *IEEE Transactions on Applied Superconductivity*, 26, 2016.

[29] Michael J Armstrong, Mark Blackwelder, Rolls-Royce North, Andrew Bollman, Christine Ross, Catherine Jones, and Patrick Norman. Architecture, voltage, and components for a turboelectric distributed propulsion electric grid final report, 2015.

[30] Wikipedia Contributors. History of superconductivity - wikipedia.

[31] Editors of Britannica Encyclopedia. Superconductivity - magnetic and electromagnetic properties of superconductors — britannica.

[32] unicated F by A Lindemann. The electromagnetic equations of the supraconductor. *Proceedings of the Royal Society of London. Series A - Mathematical and Physical Sciences*, 149:71–88, 3 1935.

[33] CCAS Coalition for the Commercial Application of Superconductors. Properties, history, and challenges.

[34] M. Cyrot. Ginzburg-landau theory for superconductors. *Reports on Progress in Physics*, 36:103, 2 1973.

[35] J. Bardeen, L. N. Cooper, and J. R. Schrieffer. Theory of superconductivity. *Physical Review*, 108:1175–1204, 12 1957.

[36] Ziad Melhem. Materials uk preliminary review superconducting materials and applications a uk challenge and an opportunity, 2011.

[37] J Georg Bednorz and K Alex Müller. Perovskite-type oxides-the new approach to high-t c superconductivity, 1987.

[38] E. A. Early, C. L. Seaman, K. N. Yang, and M. B. Maple. Demonstrating superconductivity at liquid nitrogen temperatures. *American Journal of Physics*, 56:617, 6 1998.

[39] Pablo Cayado. Preparation of gdba2cu3o7 superconducting films by chemical solution deposition. 2012.

[40] A.A. Golubov. *Handbook of Applied Superconductivity*, volume 1. IOP Publishing, 1998.

[41] D. Dew-Hughes. The critical current of superconductors: an historical review. *Low Temperature Physics*, 27:713–722, 9 2001.

[42] LHC-Closer. Taking a closer look at lhc - superconductivity in short.

[43] Applied Superconductivity Centre. Critical current comparison charts — scaling spreadsheet — applied superconductivity center.

[44] Steven M. Blair. The analysis and application of resistive superconducting fault current limiters in present and future power systems. 2013.

[45] S. Eckroad. Survey of fault current limiter (fcl) technologies - update, 2008.

[46] Xiaoyuan Chen, Huayu Gou, Yu Chen, al, Chao Yang, Ying Xin, and Chao Li. Analysing faults and sfcl response in electric aircraft you may also like superconducting fault current limiter (sfcl) for a power electronic circuit: experiment and numerical modelling further study of a novel inductive sfcl for multiterminal hvdc systems.

[47] S. M. Blair, C. D. Booth, I. M. Elders, N. K. Singh, G. M. Burt, and J. McCarthy. Superconducting fault current limiter application in a power-dense marine electrical system. *IET Electrical Systems in Transportation*, 1:93–102, 9 2011.

[48] Mathias Noe and Michael Steurer. High-temperature superconductor fault current limiters: concepts, applications, and development status. *Superconductor Science and Technology*, 20:R15–R29, 2007.

[49] P. J. Masson, G. V. Brown, D. S. Soban, and C. A. Luongo. Hts machines as enabling technology for all-electric airborne vehicles. *Superconductor Science and Technology*, 20:748, 6 2007.

[50] Yutaka Terao, Weilu Kong, Hiroyuki Ohsaki, Hitoshi Oyori, and Noriko Morioka. Electromagnetic design of superconducting synchronous motors for electric aircraft propulsion. *IEEE Transactions on Applied Superconductivity*, 28:1–5, 6 2018.

[51] Fangjing Weng, Min Zhang, Tian Lan, Yawei Wang, and Weijia Yuan. Fully superconducting machine for electric aircraft propulsion: study of ac loss for hts stator. *Superconductor Science and Technology*, 33:104002, 8 2020.

[52] Yaohui Wang, Qiuliang Wang, Hui Wang, al, Boyang Shen, Jing Li, Jianzhao Geng, T Balachandran, D Lee, N Salk, and K S Haran. A fully superconducting air-core machine for aircraft propulsion investigation of ac losses in horizontally parallel hts tapes a fully superconducting air-core machine for aircraft propulsion.

[53] Ray Radebaugh. Cryocoolers for aircraft superconducting generators and motors hydrogen cooling options for-based superconducting systems aip conference cryocoolers for aircraft superconducting generators and motors *. 1434:838, 2012.

[54] Lillian Gipson. Hybrid wing body goes hybrid. 2015.

[55] Michael Kerho. Turboelectric distributed propulsion test bed aircraft, 2013.

[56] Jeffrey J Berton and William J Haller. A noise and emissions assessment of the n3-x transport.

[57] Timon Singh. E-thrust — inhabitat - green design, innovation, architecture, green building.

[58] Bright Appiah Adu-Gyamfi and Clara Good. Electric aviation: A review of concepts and enabling technologies. *Transportation Engineering*, 9:100134, 9 2022.

[59] Frederick Berg, Joseph Palmer, Paul Miller, Mark Husband, and Graham Dodds. Hts electrical system for a distributed propulsion aircraft. *IEEE Transactions on Applied Superconductivity*, 25, 2015.

[60] Hyun Dae Kim, Gerald V. Brown, and James L. Felder. Distributed turbo-electric propulsion for hybrid wing body aircraft. *2008 International Powered Lift Conference*, pages 1–11, 2008.

[61] Cesar A. Luongo, Philippe J. Masson, Taewoo Nam, Dimitri Mavris, Hyun D. Kim, Gerald V. Brown, Mark Waters, and David Hall. Next generation more-electric aircraft: a potential application for hts superconductors. *IEEE Transactions on Applied Superconductivity*, 19:1055–1068, 2009.

[62] Steven Fletcher. Protection of physically compact multiterminal dc power systems by. 2013.

[63] Gerald Brown. Weights and efficiencies of electric components of a turbo-electric aircraft propulsion system. American Institute of Aeronautics and Astronautics, 1 2011.

[64] Puran Rakhra. On the protection of compact dc power systems with high-power energy storage, 2017.

[65] Boeing. Aero - 787 no-bleed systems.

[66] Scholarly Community Encyclopedia. Paschen's law — encyclopedia mdpi.

[67] C E Bruzek. Introduction to superconducting power cable systems, 6 2016.

[68] Frederick Berg, Joseph Palmer, Paul Miller, and Graham Dodds. Hts system and component targets for a distributed aircraft propulsion system. *IEEE Transactions on Applied Superconductivity*, 27:1–7, 6 2017.

[69] Kiruba S Haran, Swarn Kalsi, Tabea Arndt, Haran Karmaker, Rod Badcock, Bob Buckley, Timothy Haugan, Mitsuru Izumi, David Loder, James W

Bray, Philippe Masson, and Ernst Wolfgang Stautner. High power density superconducting rotating machines—development status and technology roadmap. *Superconductor Science and Technology*, 30:123002, 12 2017.

[70] Michael Armstrong. Superconducting turboelectric distributed aircraft propulsion, 2015.

[71] Vinod Kumar Khanna. *Extreme-Temperature and Harsh-Environment Electronics*. IOP Publishing, 2017.

[72] Jian Rong, Xiongyi Huang, Yuntao Song, Haojun Yang, and Kun Lu. Ac losses calculation of bi-2212 cable-in-conduit conductor used in cfetr. *Fusion Engineering and Design*, 141:109–115, 4 2019.

[73] United States Department of Energy. Process innovations for hts wire manufacturing, 2017.

[74] V E Sytnikov, V S Vysotsky, I P Radchenko, and N V Polyakova. 1g versus 2g-comparison from the practical standpoint for hts power cables use. *Journal of Physics: Conference Series*, 97:012058, 2 2008.

[75] S. Donet, F. Weiss, P. Chaudouet, S. Beauquis, A. Abrutis, H.C. Freyhardt, A. Usokin, D. Selbmann, J. Eickemeyer, C. Jimenez, C.E. Bruzek, and J.M. Saugrain. Reel-to-reel mocvd for ybco coated conductor. *IEEE Transactions on Appiled Superconductivity*, 13:2524–2527, 6 2003.

[76] Yeekin Tsui, Elizabeth Surrey, and Damian Hampshire. Soldered joints—an essential component of demountable high temperature superconducting fusion magnets. *Superconductor Science and Technology*, 29:075005, 7 2016.

[77] Kai Wang, Hao Dong, Daxing Huang, Hongjing Shang, Bowei Xie, Qi Zou, Lin Zhang, Changping Feng, Hongwei Gu, and Fazhu Ding. Advances in second-generation high-temperature superconducting tapes and their applications in high-field magnets. *Soft Science*, 2:12, 2022.

[78] Geun-Joon Lee. *Superconductivity Application in Power System*. InTech, 6 2011.

Bibliography

[79] Shinichi Mukoyama. Development of ybco high-tc superconducting power cables. *Furukawa Review*, 35:18–22, 2009.

[80] Mathias Noe. Superconducting cables, 9 2017.

[81] Keyang Wang, Wurui Ta, and Yuanwen Gao. The winding mechanical behavior of conductor on round core cables. *Physica C: Superconductivity and its Applications*, 553:65–71, 10 2018.

[82] Jean-Maxime Saugrain, Frank Schmidt, and Pierre Mirebeau. Superconducting cables-status and applications. 2007.

[83] Zhixuan Wang, Jie Qiu, Shuhong Wang, Weizhi Gong, Hui Hong, and Bo Tian. Design of cold dielectric hts power cable. pages 64–67. IEEE, 9 2009.

[84] Svetlomir Stavrev. Modelling of high temperature supraconductors for ac power applications. 2579, 2002.

[85] Antonio Morandi. Hts dc transmission and distribution: concepts, applications and benefits. *Superconductor Science and Technology*, 28:123001, 12 2015.

[86] Mohammad Yazdani-Asrami, Seyyedmeysam Seyyedbarzegar, Alireza Sadeghi, Wescley T B de Sousa, and Dustin Kottonau. High temperature superconducting cables and their performance against short circuit faults: current development, challenges, solutions, and future trends. *Superconductor Science and Technology*, 35:083002, 8 2022.

[87] S. Nolan, C. E. Jones, P. J. Norman, and S. J. Galloway. Understanding the impact of failure modes of cables for the design of turbo-electric distributed propulsion electrical power systems. pages 1–6. IEEE, 11 2016.

[88] Sriharsha Venuturumilli, Frederick Berg, Lucien Prisse, Min Zhang, and Weijia Yuan. Dc line to line short-circuit fault management in a turbo-electric aircraft propulsion system using superconducting devices. *IEEE Transactions on Applied Superconductivity*, 29:1–6, 8 2019.

174

[89] Hiroki Kojima, Fumihiko Kato, Naoki Hayakawa, Masahiro Hanai, and Hitoshi Okubo. Superconducting fault current limiting cable (sfclc) with current limitation and recovery function. *Physics Procedia*, 36:1296–1300, 2012.

[90] J.E. Jensen, W.A. Tuttle, R.B. Stewart, and H.Brechna. *BROOKHAVEN NATIONAL LABORATORY SELECTED CRYOGENIC DATA NOTEBOOK*. United Stated Department of Energy,, 1980.

[91] Daniele Colangelo and Bertrand Dutoit. Impact of the normal zone propagation velocity of high-temperature superconducting coated conductors on resistive fault current limiters. *IEEE Transactions on Applied Superconductivity*, 25:1–8, 4 2015.

[92] S. Yazaki, A. Karasawa, T. Kotoyori, A. Ishiyama, and N. Miyahara. Critical current degradation in high-temperature superconducting tapes caused by temperature rise. *IEEE Transactions on Applied Superconductivity*, 23:4602304–4602304, 6 2013.

[93] D.T. Ryan, L. Li, X. Huang, J.W. Bray, E.T. Laskaris, K. Sivasubramaniam, A.D. Gadre, J.M. Fogarty, E.J. Harley, A. Otto, and A. DenOuden. Critical current degradation in hts wires due to cyclic mechanical strain. *IEEE Transactions on Appiled Superconductivity*, 15:3684–3687, 6 2005.

[94] Nexans. Nexans superconductors for electricity grids, 2022.

[95] Min Jae Kim, Min Cheol Ahn, Seong Eun Yang, Dong Keun Park, Young Jae Kim, Tae Kuk Ko, Chanjoo Lee, and Bok-Yeol Seok. Determination of maximum permissible temperature rise considering repetitive over-current characteristics of ybco coated conductors. *IEEE Transactions on Applied Superconductivity*, 18:660–663, 6 2008.

[96] S. Nolan, C.E. Jones, R. Munro, P. Norman, S. Galloway, S. Venturumilli, J. Sheng, and W. Yuan. Experimental investigation into the fault response of superconducting hybrid electric propulsion electrical power system to a dc rail to rail fault. page 012014, 12 2017.

[97] Rui He, Yunfei Tan, Ziyi Huang, Yiming Xie, Guangda Wang, Yifan Wang, Qiong Wu, and Junwen Wei. Bending and uniaxial tensile strain effects on the critical current of rebco coated conductor tapes. *Cryogenics*, 116:103285, 6 2021.

[98] Alexandre Zampa, Christian Lacroix, Arnaud Badel, Frédéric Sirois, and Pascal Tixador. Current redistribution during inhomogeneous quench of 2g hts tapes. *Superconductor Science and Technology*, 35:095003, 9 2022.

[99] Yinshun Wang, Shaotao Dai, Xiang Zhao, Liye Xiao, Liangzhen Lin, and Dong Hui. Effects of critical current inhomogeneity in long high-temperature superconducting tapes on the self-field loss, studied by means of numerical analysis. *Superconductor Science and Technology*, 19:1278–1281, 12 2006.

[100] Irvin Chew, Andrew Lapthorn, Pat Bodger, and Wade Enright. Superconducting transformer failure : Testing and investigation. pages 4–8.

[101] Reiner Denz, Ernesto de Matteis, Andrzej Siemko, and Jens Steckert. Next generation of quench detection systems for the high-luminosity upgrade of the lhc. *IEEE Transactions on Applied Superconductivity*, 27:1–4, 6 2017.

[102] Jae-Ho Kim, Chul Han Kim, V. Pothavajhala, and S. V. Pamidi. Current sharing and redistribution in superconducting dc cable. *IEEE Transactions on Applied Superconductivity*, 23:4801304–4801304, 6 2013.

[103] Sriharsha Venuturumilli, Frederick Berg, Zhenyu Zhang, Fei Liang, Jay Patel, Min Zhang, and Weijia Yuan. Forceful uniform current distribution among all the tapes of a coaxial cable to enhance the operational current. *IEEE Transactions on Applied Superconductivity*, pages 1–1, 2016.

[104] UPSAS. Low temperature properties of materials, 2010.

[105] L Bottura. Cable stability, 2014.

[106] Boeing. New etops regulations. *Boeing.*

[107] Mohan Muniappan. A comprehensive review of dc fault protection methods in hvdc transmission systems. *Protection and Control of Modern Power Systems*, 6:1, 12 2021.

[108] Mesut E. Baran and Nikhil R. Mahajan. Overcurrent protection on voltage-source-converter-based multiterminal dc distribution systems. *IEEE Transactions on Power Delivery*, 22:406–412, 1 2007.

[109] Z. Zhou, P. Igic, P.J. Unsworth, and P.M. Holland. Design and analysis of a feedforward control scheme for a three-phase voltage source pulse width modulation rectifier using sensorless load current signal. *IET Power Electronics*, 2:421–430, 7 2009.

[110] Jin Yang, John Edward Fletcher, and John O'Reilly. Multiterminal dc wind farm collection grid internal fault analysis and protection design. *IEEE Transactions on Power Delivery*, 25:2308–2318, 10 2010.

[111] Anant Agarwal and Jeffrey Lang. *Foundations of Analog and Digital Electronic Circuits*. Morgan Kaufmann, 2005.

[112] Ming Yu, Yi Wang, Lirong Zhang, and Ziguang Zhang. Dc short circuit fault analysis and protection of ring type dc microgrid. pages 1694–1700. IEEE, 5 2016.

[113] Hengxu Ha, S. Subramanian, A. Dysko, S. Ademi, D. Vozikis, and D. Tzelepis. Impact of vsc converter topology on fault characteristics in hvdc transmission systems. pages 6 .–6 . Institution of Engineering and Technology, 2016.

[114] E. Zeldov, N. M. Amer, G. Koren, A. Gupta, M. W. McElfresh, and R. J. Gambino. Flux creep characteristics in high-temperature superconductors. *Applied Physics Letters*, 56:680–682, 2 1990.

[115] David M J Taylor and Damian P Hampshire. Relationship between the ¡i¿n¡/i¿ -value and critical current in nb ¡sub¿3¡/sub¿ sn superconducting wires exhibiting intrinsic and extrinsic behaviour. *Superconductor Science and Technology*, 18:S297–S302, 12 2005.

[116] W. T. B. de Sousa, A. Polasek, F. A. Silva, R. Dias, A. R. Jurelo, and R. de Andrade. Simulations and tests of mcp-bscco-2212 superconduct-

ing fault current limiters. *IEEE Transactions on Applied Superconductivity*, 22:5600106–5600106, 4 2012.

[117] Wescley Tiago Batista de Sousa. Transient simulations of superconducting fault current limiters. *TRANSIENT SIMULATIONS OF SUPERCONDUCTING FAULT CURRENT LIMITERS*, 2015.

[118] Semikron. Semitrans m1 power mosfet modules skm111ar, 2015.

[119] MATLAB. Solve systems of linear equations ax = b for x - matlab mldivide - mathworks united kingdom, 2023.

[120] Daniele Colangelo and Bertrand Dutoit. Inhomogeneity effects in hts coated conductors used as resistive fcls in medium voltage grids. *Superconductor Science and Technology*, 25:095005, 9 2012.

[121] Daniele Colangelo and Bertrand Dutoit. Impact of the normal zone propagation velocity of high-temperature superconducting coated conductors on resistive fault current limiters. *IEEE Transactions on Applied Superconductivity*, 25:1–7, 2015.

[122] Herman Ten Kate. (multi) normal zone propagation velocity in high current density high field magnets, 2013.

[123] Steven Nolan, Catherine E. Jones, Rafael Pena-Alzola, Patrick J. Norman, Graeme Burt, Paul Miller, and Mark Husband. Voltage-based current-compensation converter control for power electronic interfaced distribution networks in future aircraft. *IEEE Transactions on Transportation Electrification*, 6:1819–1829, 12 2020.

[124] J. Kennedy and R. Eberhart. Particle swarm optimization. pages 1942–1948. IEEE, 1995.

[125] s vakali and m.s gadala. Effectiveness of particle swarm optimization technique in dealing with noisy data in inverse heat conduction analysis. pages 40–48, 2009.

Bibliography

[126] A. Rezaee Jordehi. A review on constraint handling strategies in particle swarm optimisation. *Neural Computing and Applications*, 26:1265–1275, 8 2015.

[127] Rolf Ottersten. On control of back-to-back converters and sensorless induction machine drives department of electric power engineering. *Phd Thesis*, 2003.

[128] MATLAB. Solve nonstiff differential equations — medium order method - matlab ode45 - mathworks united kingdom, 2023.

[129] Kitko Metals. Copper spot price.

[130] Jean Rivenc, Gilles Peres, Frederick Berg, Lucien Prisse, Peter Rostek, Dmitry Melyukov, Vadim Amelichev, and Sergey Samoilenkov. An evaluation of high temperature superconducting power cables for airborne application. pages 1–21. AIAA, 2018.

[131] Kiruba Sivasubramaniam, Tao Zhang, Antonio Caiafa, Xianrui Huang, Minfeng Xu, Liang Li, E. T. Laskaris, and J. W. Bray. Transient capability of superconducting devices on electric power systems. *IEEE Transactions on Applied Superconductivity*, 18:1692–1697, 2008.

[132] Michael James Armstrong, Mark J. Blackwelder, Andrew M. Bollman, Christine A. H. Ross, Angela Campbell, Catherine E. Jones, and Patrick J. Norman. *Architecture, Voltage, and Components for a Turboelectric Distributed Propulsion Electric Grid*. 2015.

[133] Steven Fletcher. Protection of physically compact multiterminal dc power systems. 2013.

[134] Mohammed Kh AL-Nussairi, Ramazan Bayindir, Sanjeevikumar Padmanaban, Lucian Mihet-Popa, and Pierluigi Siano. Constant power loads (cpl) with microgrids: Problem definition, stability analysis and compensation techniques. *Energies*, 10, 2017.

[135] Fei Gao, Serhiy Bozhko, Alessandro Costabeber, Greg Asher, and Pat Wheeler. Control design and voltage stability analysis of a droop-controlled

electrical power system for more electric aircraft. *IEEE Transactions on Industrial Electronics*, 64:9271–9281, 2017.

[136] Josep M. Guerrero, Mukul Chandorkar, Tzung Lin Lee, and Poh Chiang Loh. Advanced control architectures for intelligent microgridspart i: Decentralized and hierarchical control. *IEEE Transactions on Industrial Electronics*, 60:1254–1262, 2013.

[137] Fei Gao, Serhiy Bozhko, Seang Yeoh, Greg Asher, and Patrick Wheeler. Stability of multi-source droop-controlled electrical power system for more-electric aircraft. *2014 IEEE International Conference on Intelligent Energy and Power Systems, IEPS 2014 - Conference Proceedings*, pages 122–126, 2014.

[138] Xavier Giraud, Hubert Piquet, Marc Budinger, Xavier Roboam, Marc Sartor, and Sebastien Vial. Knowledge-based system for aircraft electrical power system reconfiguration. *Electrical Systems for Aircraft, Railway and Ship Propulsion, ESARS*, 2048:1–6, 2012.

[139] Daniel Schlabe and Jens Lienig. Energy management of aircraft electrical systems - state of the art and further directions. *Electrical Systems for Aircraft, Railway and Ship Propulsion, ESARS*, pages 1–6, 2012.

[140] O Meier, D Scholz, and Ing Dieter Scholz. A handbook method for the estimation of power requirements for electrical de-icing systems. 2010.

[141] S Wang, Juming Tang, and F Younce. Temperature measurement. pages 987–993. Marcel Dekker Inc., 2007.

[142] Rik De Donkcer, Duco Pulle, and André Veltman. *Advanced Electrical Drives Analysis, Modeling, Control*. Springer, Dordrecht, 2011.

[143] MATLAB. Implement abc to dq0 transform - simulink - mathworks united kingdom.

[144] V Blasko and V Kaura. A new mathematical model and control of a three-phase ac-dc voltage source converter. *Power Electronics, IEEE Transactions on*, 12:116–123, 1997.

Bibliography

[145] M. Milŏsević. Decoupling control of d and q current components in three-phase voltage source inverter. *Engineering*, 2003.

[146] Josep M. Guerrero, Juan C. Vasquez, José Matas, Luis García De Vicuña, and Miguel Castilla. Hierarchical control of droop-controlled ac and dc microgrids - a general approach toward standardization. *IEEE Transactions on Industrial Electronics*, 58:158–172, 2011.